Molecular Imaging of Abdominal Aortic Aneurysm with Sodium Fluoride

Michael Andrew Bell

Submitted in accordance with the requirements for the degree of Doctor of Philosophy

The University of Leeds
Faculty of Medicine and Health
Leeds Institute of Cardiovascular and Metabolic Medicine

November, 2022

The candidate confirms that the work submitted is his/her own and that appropriate credit has been given where reference has been made to the work of others.

Acknowledgements

Completing this PhD has been a brilliant, challenging and thought provoking experience, and I couldn't have accomplished this without my supervisory team. Marc, thank you for taking me on as your PhD student and taking me under your wing. You've instilled belief, resilience, calm and constantly encouraged me throughout this process. I enjoyed many of our chats over coffee and in surgery. Harry, thank you for joining my supervisory team during the pandemic and giving your PET/CT knowledge to this project. Thank you for your constant encouragement and direction both here in Leeds and abroad. Thank you also to Professor David Beech, Dr Richard Cubbon and Dr Karen Porter for giving me the opportunity to undertake research on the BHF programme in 2017 and keeping a key eye on my progress. Thank you also to Dr Jon De Siqueira for assessing my progress each year and encouraging my research. LICAMM has felt like a family and I will miss it greatly. Thank you also to the BHF for funding this project.

I wouldn't have been able to have completed this project without the friendship and support of the Bailey and Tsoumpas group members, the wider institute and to the many friends I've made here in Leeds. To Lucy, Karen, Kavi, Heba, Mohammed and Harry, thank you for your support and for the many scientific discussions. Thank you also to John and Joanna for their assistance in ePIC and to Mel for her help in CBS. To Leander, Marj, Fiona, Laeticia, Alex, Chris, Emma, Nikoletta, Greg, Gillian, Lauren, Ash, Jacob, Eva and everyone on the BHF programme (past and present), thank you for making the experience so enjoyable and hopefully my jokes weren't too annoying.

Thank you to the Bell clan, Margaret, Andrew, Sarah and the cats Sox and Sheba for your love and support throughout this process and listening to me talk on about aortas and images. My final thanks must go to Katie. I met you as a friend, and now you are my fiancée. You always know how to put a smile on my face, make me laugh constantly, helped me rationalise decisions and would always indulge in some great food. I can't put into words how grateful I am. "Few word do trick" Kevin Malone, The Office, S8 Ep2.

Abstract

Introduction

An abdominal aortic aneurysm (AAA) is a focal dilation of the aorta and AAA rupture (clinical endpoint) is associated with high mortality. Diagnosis and management of AAA has relied on ultrasound based screening programmes through the measurement of aortic diameter. Although these programmes have managed patients effectively, longitudinal analysis of aortic diameter data has shown a change in epidemiology and heterogeneity of AAA. The SoFIA trial showed that uptake of Sodium Fluoride (Na[^{18}F]F), a marker of microcalcification, could predict aneurysm growth and end clinical events (i.e. risk of rupture) independent of cardiovascular risk factors (e.g. smoking). However, how microcalcification develops and drive aneurysm progression is unknown and Na[^{18}F]F uptake was measured at a singular aortic diameter. This project investigated the relationship between Na[^{18}F]F uptake and aortic growth in a preclinical model and to determine the biological mechanism that promotes microcalcification development in AAA.

Methods

AAA were induced in C57Bl/6 and mice harbouring a conditional mTomato/m-Green fluorescent protein (mTmG) reporter gene using the porcine pancreatic elastase (PPE) model, with sham equivalents. Ultrasound scanning was used to confirm the induction of AAA. C57Bl/6 mice underwent 90 minute dynamic terminal Na[^{18}F]F PET/CT scan and aortas were harvested and placed into a gamma counter. Aortas were then sectioned and stained for the presence of microcalcifications using a von Kossa stain.

mTmG aortas were sectioned and stained for bone morphogenetic protein-2 (BMP2). Sections were imaged using a confocal microscope and z-stack images at 40 x magnification were taken. Nuclei expressing mGFP, BMP2 and other markers of interest were quantified and expressed as percentage of all cells counted.

Results

PET/CT quantification of sham vs PPE images for a range of metrics demonstrated no difference in Na[^{18}F]F uptake in the abdominal aorta. However,

quantifying %ID/g from *ex vivo* gamma counting revealed a significant difference in uptake between sham and PPE abdominal aorta day 14 post surgery (%ID/g = 0.00015 ± 0.015 vs 0.13 ± 0.0025. $P<0.05$). The appearance of microcalcification deposits was confirmed by von kossa stain. Upregulation of BMP2 was associated with nuclei expressing mGFP (lineage traced vascular smooth muscle cells) and was highest at day 7 post surgery when compared to sham sections (28.0 ± 3.6% vs 0% respectively. $P<0.05$). A high percentage of nuclei expressing mGFP AND BMP2, but not markers of vascular smooth muscle cells was highest at day 14 post surgery in PPE aortic sections, compared to day 7 (4.45 ± 1.5 vs 1.69 ± 0.73% respectively. $P<0.05$). This suggests vascular smooth muscle cell remodelling could be a driver of microcalcification formation in PPE model.

Conclusion

Although Na[^{18}F]F PET/CT experiments were inconclusive, *ex vivo* gamma counting demonstrates an increased uptake of Na[^{18}F]F in day 14 PPE AAA tissue. Expression of BMP2 was localised to lineage traced vascular smooth muscle cells and upregulated day 7 post surgery in PPE AAA tissue. This suggests a potential link between BMP2 expression and microcalcification development in AAA pathology. Further work includes the formulation of a therapeutic intervention to target vascular smooth muscle remodelling to prevent microcalcification development and slow down AAA progression.

Table of Contents

Table of Figures

Table of Tables

List of Abbreviations

[OH-]	Hydroxyl ion
2-[^{18}F]-FDG	2-[^{18}F]-Fluorodeoxyglucose
3-[^{18}F]-FLT	3-[^{18}F]-Flurothymidine
AA	Abdominal Aorta
AAA	Abdominal aortic aneurysm
ALP	Alkaline phosphatase
Ang-II	Angiotensin II
ApoE	Apolipoprotein E
α-SMA	α-smooth muscle actin
BHF	British Heart Foundation
BMP	Bone morphogenetic protein
$CaCl_2$	Calcium Chloride
CD105	Cluster of Differentiation 105
CT	Computed Tomography
CTA	Computed Tomography Angiography
DM	Diabetes mellitus
DMEM	Dulbecco's Modified Eagle Medium
DNA	Deoxynucleic acid
ECM	Extracellular Matrix
EDS	Ehlers-Danlos syndrome
EVAR	Endovascular repair
FBN-1	Fibrillin-1
GAPDH	Glyceraldehyde 3-phosphate dehydrogenase
GCA	Giant cell arteritis
GLUT4	Glucose transporter type 4
HKEM	Hybrid Kernelized Expectation Maximum
ID/g	Injected dose per gram
ILT	Intraluminal thrombus
ITI	Inner to inner
KEM	Kernelized Expectation Maximum
LDLR	low-density lipoproteins receptor

LDS	Loeys-Dietz syndrome
MASS	Multicentre aneurysm screening programme
mGFP	m-Green Fluorescent protein
MLEM	Maximum Likelihood Expectation-Maximization
MMP	Matrix metallopeptidase
MR	Magnetic Resonance
mTom	m-Tomato
Na[^{18}F]F	Sodium Fluoride
NAAASP	National health service abdominal aortic aneurysm screening programme
NICE	National institute of health and care excellence
OPG	Osteoprotegerin
OPN	Osteopontin
OSEM	ordered subset expectation maximization
OSR	Open surgical repair
OTO	Outer to outer
PAD	Peripheral Arterial Disease
PAH	Peripheral Arterial Hypertension
PBS	Phosphate buffer saline
PDGF	Platelet Derived Growth Factor
PET	Positron Emission Tomography
PET/CT	Positron Emission Tomography coupled Computed Tomography
PPARy	peroxisome proliferator-activated receptor – γ
PPE	Porcine pancreatic elastase
PPG	Pentagalloyl glucose
QALY	Quality adjusted life year
RNA	Ribonucleic acid

ROI	Region of Interest
RT-PCR	Real Time Polymerase Chain Reaction
Runx-2	Runt-related transcription factor 2
Smooth muscle myosin heavy chain	SMMHC
SUV	Standard Uptake Value
SVSMC	Saphenous vein smooth muscle cells
TAA	Thoracic aortic aneurysm
TBR	Tissue to background ratio
TGF-B	Transforming growth factor-B
TGFBR	Transforming growth factor B receptor
TGFB-S	Transforming growth factor B signalling
TRIAL	Tumour necrosis factor related apoptosis inducing ligand
UK	United Kingdom
UKSAT	UK Small aneurysm trial
USS	Ultrasound
VEGF	Vascular Endothelial growth factor
VSMC	Vascular Smooth Muscle Cells

Publications and Communications

Publications

First author:

Bell M, Gandhi R, Shawer H, Tsoumpas C, Bailey MA. Imaging Biological Pathways in Abdominal Aortic Aneurysms Using Positron Emission Tomography. Arterioscler Thromb Vasc Biol. 2021;41(5):1596–606.

Co-author:

Gandhi R, **Bell M**, Bailey M, Tsoumpas C. Prospect of positron emission tomography for abdominal aortic aneurysm risk stratification. J Nucl Cardiol [Internet]. 2021; Available from: https://doi.org/10.1007/s12350-021-02616-8

Communications

Oral:

Tracing microcalcification development in the porcine pancreatic elastase murine model of abdominal aortic aneurysm using Na[^{18}F]F. **Michael Bell**, Joanna Koch Paszkowski, John Wright, Lucy Craggs, Charalampos Tsoumpas, Marc A Bailey. The 7th International Meeting on Aortic Diseases, Liege (2022). Recipient of Evangelos Zlatoudis prize.

Functional imaging of the aortic wall. **Michael Bell**, Marc A Bailey. The 12th European Symposium on Vascular Biomaterials, Strasbourg (2021)

Poster presentation:

[^{18}F]NaF uptake in the porcine pancreatic elastase (PPE) model of abdominal aortic aneurysm. **Michael Bell**, Joanna Koch Paszkowski, John Wright, Harry Tunnicliffe, Lucy Craggs, Charalampos Tsoumpas, Marc A Bailey. 16th European Molecular Imaging Meeting, Gottingen (2021)

Chapter 1
Introduction

1.1 Cardiovascular disease

Cardiovascular disease is one of the leading causes of death in the United Kingdom (UK), with the British Heart Foundation (BHF) reporting 616,014 deaths in 2018 (1). In the same report, the number of deaths attributed to cancer was 170,992 and 62,131 to Alzheimer's Disease. The associated cost of treating and managing cardiovascular disease in the NHS is £9 billion annually. Cardiovascular disease encompasses the terms relating to disease of the heart and vasculature. Some examples include atherosclerosis, hypertension, myocardial infarction, hypertrophic cardiomyopathy, stroke and aneurysms. The main focus of this thesis will be abdominal aortic aneurysms or 'AAA' specifically.

1.2 Aneurysms

An aneurysm is defined as a focal dilation of a vessel (most commonly the aorta or intercranial artery). An aneurysm is defined diagnostically when the diameter of a vessel reaches 1.5 times greater than the adjacent normal artery. For example, the baseline diameter of the aorta is 1.5 to 2 cm and an AAA is diagnosed when the aortic diameter is measured as 3 cm. Aneurysms are an important vascular disorder as they are associated with potentially fatal complications such as occlusion or rupture. The prevalence of intracranial aneurysms is 3% (2) and 1.34% for AAA in the UK (3). Rupture of intracranial aneurysms can lead to subarachnoid haemorrhage accounting for 7% of all strokes.

1.3 Aortic Aneurysms

The aorta is the largest blood vessel in the body and originates from the heart, at the aortic valve. The aorta distributes blood under high pressure and velocity from the left ventricle throughout the body and faces a high haemodynamic burden (4). The aorta is comprised of the ascending aorta (i.e. the origin of the aorta starting in the heart), the aortic arch (as it turns 180 degrees at the top of the chest to give off the great vessels) the descending thoracic aorta through the chest and the abdominal aorta in the abdomen. The aorta then splits into the iliac arteries at the aortic bifurcation, around the level of the umbilicus to supply blood to the legs.

The aorta is comprised of three layers; (i) tunica intima, a thin layer of endothelial cells and elastic lamella, (ii) tunica media, vascular smooth muscle cells (VSMCs) densely packed into a multilayer and extracellular matrix (ECM), (iii) tunica adventitia, layer made of fibrous tissue, vaso vasorum (small vessels) and nerves.

Aneurysm formation within the aorta is mainly found within the thoracic (TAA) and abdominal regions. The structure and cellular composition of the thoracic and abdominal aorta differs slightly and could be a contributor to the differences in regional aneurysm pathophysiology. In the ascending aorta, the intima is thinner, the media is thicker and the content of elastin and collagen is higher (5). However TAA and AAA do share some similar histological features, such as VSMC loss and ECM degradation.

Dilation of the thoracic aorta is also linked to genetic disorders. Mutation of Fibrillin-1 (FBN-1) gene, which causes Marfan syndrome, destabilises the aortic wall through distribution of the elastin filament alignment and lamellar units (6). A study of 135 individuals with TAA with or without dissection demonstrated that 19% of the study population had a family history of TAA (7). These subjects had fast aneurysm growth and an autosomal dominant mode of inheritance. Mutations have been found to exist on 3p24.2-25, 5q13-14 and 11q23.2-q24 loci suggesting genetic heterogeneity (8). Finally, aortic dilation in the thoracic aorta, as well as the intercranial arteries, can be caused by the inflammatory disease Takayasu's arteritis (9). Those with familial inheritance of Ehlers-Danlos syndrome (EDS) can suffer from aneurysm formation and fragile vessels due to abnormal collagen synthesis (10). Although EDS is associated with a number of subtypes, it is believed that type I, III and IV are associated with vascular complications. Mutations of transforming growth factor β receptor (TGFβR) I and II, defined as Loeys-Dietz syndrome (LDS), suffer from altered transforming growth factor B signalling (TGFB-S), resulting in aortic dissection (11). Individuals with LDS are at a higher risk of early rupture at small aortic diameters due to rapid progressive nature of disease. Alterations in smooth muscle cell contractile proteins have also been shown to drive TAA progression. Mutations in α-smooth muscle actin (α-SMA (ACTA2)) in TAA subjects, detected by immunofluorescence, showed impaired interactions with actin filaments (12). Tissue analysis also demonstrated medial degeneration and smooth muscle

proliferation as well as medial smooth muscle hyperplasia. The study suggests the importance of smooth muscle contractile proteins in structural integrity of the aorta.

The defects caused in key signalling pathways and smooth muscle contractile proteins within the vessel wall could be the key reason that drives aortic dilation due to the extreme shear stress and mechanical strain placed on the vessel wall. However, a better understanding of these pathways in aneurysm development is required.

1.4 Abdominal Aortic Aneurysm (AAA)

As defined in Section 1.2, an AAA is a focal dilation of the abdominal aorta, associated with aortic wall damage, where AAA rupture is linked to high mortality (13,14). The diagnostic criteria for AAA is an abdominal aorta greater than 3cm. This is normally confirmed by a screening ultrasound scan of the abdominal aorta, however some AAA are diagnosed incidentally through other medical disease check-ups (15). As the aneurysm expands, the risk of rupture (considered the primary clinical endpoint) increases, accounting for 4000 deaths per annum in England and Wales (16). Analysis of Hospital Episode statistics data between 2005-2010 concluded that in-hospital mortality in the UK was 65.9% for ruptured AAA and post intervention mortality was 41.77% (17). This risk nominally occurs as the diameter exceeds the intervention threshold of 5.5 cm (13–15). However, some small aneurysms are prone to rupture (18). Clinically, the rupture risk of an aneurysm at 5.5 cm is quoted as 3% per year. By contrast, analysis of the National Health Service abdominal aortic aneurysm screening programme (NAAASP) suggests that the rupture risk is more likely to be 0.4% per year (3). To mitigate aneurysm rupture, AAA patients are sent for elective repair.

1.4.1 AAA epidemiology

The risk factors associated with AAA are related to aneurysm development (age, male sex, family history, smoking), expansion (smoking, hypertension) and rupture (smoking) (19–21). The prevalence of diagnosed AAA increases with age (22) with the mortality rate per 100 people is 1.02 for age group 60-65, 1.91 for age group 65-70 and 2.73 for age group 70-75 (3). Although the prevalence of AAA in males has been reported as 4.7% in the UK between 1997-1999 (23), the prevalence has dropped to 1.34% in the real-world observational screening data

(24). This is attributed to a change of epidemiology and environmental factors, particularly changing smoking habits. The risk of AAA rupture in men is much higher than that of women (22) however 31% of ruptured AAA recorded between 2001-2014 occurred in women (25). In addition, women with a history of smoking are 15 times more likely to develop an aneurysm than women who have never smoked. This contrasts with men, where the risk is 7 times more likely in those with a history of smoking versus those without (26). Despite this, inviting women to a similar screening programme to that already offered to men in the UK is not cost effective (27). Although there is no conclusive mechanistic causative link between smoking and AAA, smoking increases aneurysm expansion rate by 15-20% and doubles the risk of rupture (16,28,29).

Hypertension is also seen to increase the risk of AAA, with more than half of the cases in data analysed from large screening programmes having confirmed and treated hypertension (30,31). Interestingly, diabetes mellitus (DM) is shown to be protective against AAA formation and AAA growth (32,33) even though DM is a key risk factor for atherosclerotic cardiovascular disease (20). The protective nature of DM on aneurysm growth is thought to be a result of cross-linking glycation products on ECM remodelling and TGF-β signalling pathway contributing an anti-inflammatory effect (34). As a result, antidiabetic treatments, such as metformin, has been tested in a cohort of AAA subjects to study the link between aneurysm growth and treatment. Prescribed metformin showed a reduced likelihood of increased aneurysm growth (35). A phase 2 clinical trial for metformin treatment of AAA is currently in progress (Limiting AAA with Metformin trial (LIMIT) NCT04500756).

1.4.2 Screening

Historically, diagnosis of AAA occurred incidentally through unrelated medical check-ups or imaging studies (36,37). The implementation of dedicated ultrasound based screening programmes has facilitated more coherent diagnosis and monitoring. Such initiatives have been used in the UK (38), the United States of America (39) and Sweden (40) to date, with other countries such as Denmark, Australia and New Zealand implementing randomized trails (41). The initiation of ultrasound based screening programmes resulted from the Multicentre Aneurysm Screening Study (MASS) (23). This pivotal study showed that entering a screening programme could reduce the risk of rupture by 53%. As a result, the

UK NAAASP was implemented in 2013 and invites men aged 65 years old for a single abdominal ultrasound scan. To support the implementation and continuation of the programme, cost-effective analysis is used as an economic modelling tool to measure disease burden. The model takes into consideration not only aneurysm growth and rupture as well as invitation to screen, surveillance scan and repair costs. The analysis shows that the per quality-adjusted life-year (QALY) gained is £7,370 (42), well below the UK National Institute of Health and Care Excellence (NICE) cost-effectiveness threshold.

Definition of aortic diameter varies between countries. Figure 1 outlines the differing metrics used to define the anterior to posterior (AP) wall measurement (43). In the UK, the outer to outer (OTO) AP measurement is reported in aneurysm screening programs, as described in the UK small aneurysm trial (UKSAT) (44). However, a comparison between inner to inner wall (ITI) and OTO was conducted in the UK due to the discussion of ITI measurements underestimating the aortic diameter (45). The results of the trail showed on 60 imaging data sets, the difference in reported diameter was 0.27 cm with ITI measurements were more reproducible. As a result, ITI was then implemented in the NAAASAP. In Sweden, the leading edge to leading edge method is implemented (46).

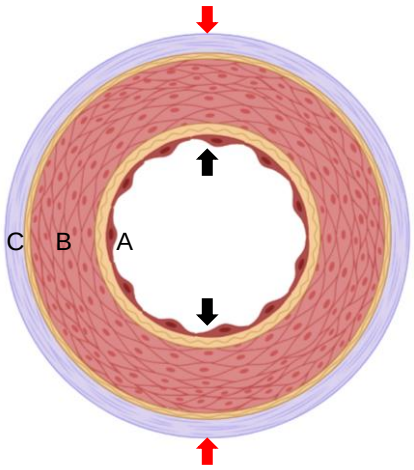

Figure 1: Cross section of the aorta representing a transverse image as taken in an Ultrasound scan. The three layers of the aorta, the tunica intima (A), tunica media (B) and tunica adventitia (C) are shown. The inner to inner (ITI) edge aortic diameter is measured by the two black arrows, the leading to leading edge diameter is measured by one black and red arrow of the same direction and the outer to outer (OTO) edge diameter is measured by the two red arrows. (Adapted from(47), image created in Biorender).

The criteria used in NAAASP for patient follow up and treatment is based on those employed in the MASS trial. After measurement of the anterior to posterior wall (AP) diameter, the results fall into the categories shown in Table 1 (23). The intervention threshold has been set from the results from the UKSAT, demonstrating there was no survival benefit in repairing small aneurysms versus large aneurysms (based on the MASS trial criteria) (44,48,49). However, the decision to set the intervention threshold at 5.5 cm in the UKSAT trial was informed by discussion, with no robust evidence demonstrating the true intervention size for AAA, although it is clear that aortic size correlates with rupture risk (50). With the access to large datasets and further analysis, it could be argued that the follow up criteria should be reviewed. A meta-analysis by the RESCAN collaborators assessed data collected from 18 centres across the UK and world (amassing to 15,742 patient data sets) studying the longitudinal growth of aortic diameter in AAA subjects (51). The study showed that for a small aneurysm to reach a clinically relevant diameter (i.e. ~5.5 cm) could take between 7-13 years. In addition, for a small aneurysm (3 cm in diameter) to have a 1.0% annual risk of rupture took between 4-10 years from the first scan. A comparison of four mathematical models used in the literature to examine aneurysm growth on a subset of patients demonstrated aneurysm growth is heterogeneous, but best modelled by non-linear methods (18). In addition, analysis of 18,652 data sets showed that the rupture risk for subjects (per annum) with a small aneurysm is 0.03%, 0.28% for medium aneurysms and 0.4% for large aneurysms (3). It should be noted that previously the rupture risk for large aneurysms that are untreated was quoted as 3.5% (52). In addition, with the COVID-19 pandemic (where AAA intervention was deferred until 7.0cm in the UK during the first wave) further data could now be explored.

Table 1: MASS criteria for detection and management of AAA based on USS (23)

Measurement	Follow up procedure
< 3 cm	No follow up
3 – 4.4 cm	Yearly follow up
4.5 cm – 5.4 cm	3 monthly follow up
> 5.5 cm	Refer to surgery

Investigation of whether rupture risk or aneurysm growth in individuals who have had their follow up ultrasound scans or “classical” intervention procedures postponed is consistent with existing data may indicate if refinement of the MASS criteria is needed (53,54). The data from the RESCAN and NAAASP meta-analysis suggest there is a large (clinically unnecessary) scan burden on the NHS and AAA patients.

Historically, aortic size and rupture risk have been correlated to guide patient management and intervention. Nominally the AAA rupture risk increases once passed the 5.5 cm threshold used for intervention. Rupture risk for aneurysms eligible for intervention has been reported to be between 25-40% compared to a rupture risk of 1-7% in aneurysms between 4.0 and 5.0 cm (55). Reports from UKSAT demonstrated that rupture risk of aneurysm between 4.0 cm and 5.5 cm was 1% (44). Access and analysis to the data collected from NAAASP has shown that contemporary rupture risk is much lower (3). For small AAA (3.0-4.4 cm) the rupture risk is reported at 0.03% per annum and for medium AAA (4.5-5.4 cm) the rupture risk is reported at 0.28%. Interestingly, for aneurysms above the threshold for intervention the rupture risk was 0.4%. The data from NAAASP suggests that using aortic size as a predictor of rupture may not be the best predictor of patient outcome. In addition, aortic size does not account for small aneurysm rupture.

Alternative biomarkers that have been investigated to predict aneurysm rupture include the application of Laplace law, depicting a linear relationship between diameter and wall stress, and finite element analysis which can evaluate stress on AAA walls (56). A combination of Computed Tomography (CT), 3D computer modelling, finite element analysis and blood pressure data showed initial peak wall stress was a more accurate predictor of subjects requiring intervention surgery compared to aortic diameter (57). An alternative computer model has been postulated that incorporates a range of AAA rupture severity parameters (58). Parameters incorporated within the model include stress ratio, asymmetry index and diameter ratio and are calculated from CT data. Although the model was only tested in three AAA patients, the calculated values agreed with the chosen clinical outcome for these individuals.

Most analysis methods fall short due to the regular predictive model used whereas AAA are heterogeneous, irregular structures. There is a clear need to

find an accurate predictor of aortic rupture in order to offer personalised medicine for better management of AAA subjects (such as personalised surveillance intervals and intervention thresholds). The data presented above suggest that aortic diameter may not be the most suitable metric to provide the best possible care to aneurysm subjects or provide personalised approaches. Investigating the use of other image derived biomarkers that have clinical utility has become an active area of research. Although 2D ultrasound measurements are under scrutiny, a preclinical study using the porcine pancreatic elastase (PPE) model of AAA showed that the growth of aneurysms modelled by 3D aortic volume measurements differed to the linear growth seen by measuring aortic diameter (59). Aortic volume peaked at day 10 post surgery, whereas aortic diameter peak day 14 post surgery. The preclinical investigation gives insight into the longitudinal growth of AAA in murine model that could reflect human AAA development.

1.4.3 Intervention

Once an AAA reaches an aortic diameter > 5.5 cm, patients are considered for elective surgery if they are medically fit enough and have sufficient predicted life expectancy to receive benefit. Elective surgery is more favourable than emergency repair of ruptured aneurysm, with the 30 day mortality risk rising from 2-3% (60) to 40-50% respectively (44,61). There are two clinically acceptable methods for elective repair of AAA; open surgical repair (OSR) or minimally invasive endovascular repair (EVAR) within the new NICE guidelines (62), which support the use of OSR (63–65). OSR uses a prosthetic graft to replace the diseased aneurysmal segment. The aorta is exposed through one of two approaches; the transperitoneal approach (laparotomy) or retroperitoneal approach (incision on the side of the subjects towards the rectus abdominis). The aneurysmal sac is opened to remove the thrombus before addition of a prosthetic graft. EVAR, on the other hand, introduces a bifurcated covered stent through the femoral artery to exclude blood flow from the aneurysm. Although EVAR is quicker compared to OSR and is associated with a reduced morbidity, reduced early mortality and length of hospital stay, EVAR suffers from a higher rate of re-intervention and surprisingly, increased late mortality. The EVAR 1 trial randomly assigned 1082 patients with AAA at the intervention threshold into two groups, those who would receive EVAR and those that would receive OSR. The

30 day mortality for group assigned to EVAR procedure was much lower than that in the OSR group (1.7% vs 4.7%), although secondary interventions was much higher in the EVAR group (66). The early suggestion that EVAR intervention was linked to reduced mortality and shorter intensive care unit stays when compared to OSR was echoed in the DREAM (67) and OVER (68) trails. However longer term follow up (10-12 years) of patients in EVAR 1 and DREAM trial demonstrated that subjects that underwent OSR had a better survival rate when compared to EVAR (69,70). The follow up to the original EVAR 1 trial, EVAR2, assigned subjects not eligible for OSR into EVAR intervention and no intervention and assessed the survival rates. Although the 30 day mortality of EVAR2 matched the initial results of EVAR 1 (EVAR intervention mortality 7.3% vs 12.4% in no intervention group), the rate of death from any cause was the same in the two groups (71). In addition, EVAR intervention subjects has higher rates of complications and reinterventions, suggesting that EVAR is associated with higher costs compared to OSR. Here in the UK EVAR is considered for randomised trials, elective aneurysm surgery and for cases of rupture (62).

1.5 AAA Murine Models

Preclinical *in vivo* models mimicking AAA pathophysiology have been invaluable in studying aetiological factors, potential therapeutic targets and evaluating novel radiotracer probes. The three established and reported models are the PPE, calcium chloride ($CaCl_2$) and Angiotensin-II (Ang-II) infusion model. All three models are established and used by our group in Leeds (72,73).

1.5.1 PPE AAA model

The earliest model of AAA pathophysiology was the PPE model, developed in 1963 to mimic elastin destruction in the aorta, as seen in humans (74). The first version of the model infused PPE into the aorta for 5 minutes (75,76). The infrarenal aorta is first identified and dissected. The aorta is clamped at the bifurcation of the vessel. A catheter is inserted into the aorta and PPE is infused. Blood flow is then restored to the aorta and the abdomen is closed. Typically aortic expansion is seen 14 days post-procedure. This procedure is both surgically and technically challenging as the aorta is isolated and the pressure of infused PPE determines the severity of induced aneurysm. As a result the simpler peri-adventitial PPE model was developed to mitigate the challenges in 2012

(77). Here, the infrarenal aorta is identified and dissected. PPE (10 µL) is then applied directly onto the exposed external surface of the aorta, followed by repeat washing of the aorta with PBS. Aortic expansion is usually seen 14 days post-surgery, although aortic volume reaches its peak at day 10 post-surgery (78). Peri-adventitial application of PPE allows aneurysm induction to occur on the infrarenal aorta mimicking human scenario.

The PPE model mirrors elements of human aneurysm pathophysiology including elastin breakdown and macrophage infiltration (79,80). The early stage of formation (from day 0 to day 7) is characterized by inflammation driven aortic dilation, whilst late-stage formation (day 7 to day 14) is characterized by elastin breakdown by T-cells and macrophages, resulting in full model induced aortic dilation. Post day 14, the aneurysm spontaneously regresses over time. Gender differences in aortic expansion have also been reported in rats using the perfused PPE model. Male rats had larger reported aneurysm (200% diameter increase) compared to female rats (69.4% diameter increase) and the histological presence of macrophages and matrix metalloproteinase (MMP)-9 in the media and adventitia was visible in males (81). In addition, aneurysm induction was achieved in 100% of males compared to only 29% of females. A major difference of this model compared to human pathology is aortic rupture is not observed. In addition, differences to classical AAA risk factors, such as smoking, are unknown. In our laboratory we have followed the PPE model out to 84 days and observe a slow recovery and repair of the aorta (although not complete normalisation) over time rather than ongoing expansion.

1.5.2 $CaCl_2$ model

The $CaCl_2$ model is an important model of AAA due to the presence of microcalcification on the aorta in small and late stage aneurysms (82,83). The initial model was developed in rabbits to explore calcification driven aneurysm formation on the carotid arteries due to the presentation of macrocalcification deposits visualised by CT (84,85). The approach has since been repurposed for murine models (86). The surgical procedures follows the same principle as the peri-adventitial PPE model, as described in section 1.5.1. The abdominal aorta is dissected before a soaked swab of $CaCl_2$ is applied to the aorta for 15 minutes. The aorta is then washed with repeat aliquots of PBS before the abdomen is closed. Aortic dilation is thought to occur through calcium deposits onto the

elastin structure, causing an inflammatory response and a breakdown of elastin matrix (79,86). The biological pathway is believed to be generation of calcium phosphate, through calcium ions transformed by VSMC alkaline phosphatase activity, which deposit on the elastin network. This leads to the production of hydroxyapatite crystals with the elastin network.

The reported concentration of $CaCl_2$ used and the time taken to induce aortic dilation varies. The first reported murine model used 0.5 M $CaCl_2$ and reported a 64% increase in aortic dilation (compared to baseline) two weeks post-surgery and a 110% increase in aortic dilation three weeks post-surgery (86). Alternatively, aortic dilations 7, 42 and 84 days post-surgery have also been reported (87–89). The marked histological features of this model include elastin destruction, macrophage infiltration, calcium deposits on the elastin layer and influx of MMPs (86,90,91). The $CaCl_2$ model has also been used to study therapeutic response. Periadventitial application of pentagalloyl glucose (PPG) at day 1 or day 28 post $CaCl_2$ application showed attenuation of aneurysm growth and dilation, as well as inhibition of elastin destruction (92). Histological analysis of the treatment tissue demonstrated no disruption in levels of MMPs or macrophages. Calcification deposits were also seen. Alternatively intraperitoneal injection of resveratrol showed preservation of the elastin matrix, as well as reduction in aortic dilation and number of inflammatory cells deposited on the aortic wall (93).

The $CaCl_2$ model is a useful model to study aneurysm pathology in the preclinical setting, however the model does not reflect some of the clinical features seen in human pathophysiology. The model does not show intraluminal thrombus, rupture or atherosclerosis (85). In addition the known clinical risk factors of AAA (e.g. age, smoking) are not seen in this model. Similar to the PPE model, it seems to regress over time rather than exhibiting ongoing growth and eventual rupture as seen in human patients.

1.5.3 Angiotensin-II (Ang-II) model

The final model of AAA that is used most frequently in preclinical exploration of aneurysm pathology is infusion of Ang-II. The Ang-II model is surgically less demanding than the aforementioned AAA models as the model requires implantation of pumps subcutaneously and no laparotomy is required. The model

itself was discovered incidentally with the main aim of the two studies looking at the effects of angiotensin in atherosclerosis on mice deficient in the low-density lipoprotein receptor (LDLR) (94) and apolipoprotein E (ApoE) (95). It was noted that in both of these hypercholesteraemic, atherosclerotic mice, spontaneous aortic dilation was apparent in the suprarenal abdominal aorta. Difference in gene expression between the suprarenal and infrarenal aortic sections may account for preference of the Ang-II model to form aneurysms in the suprarenal section (96). Formation of Ang-II induced aneurysm occurred through the development of intimal micro-tears resulting in the development of an intramural hematoma, wall remodelling and aortic dilation (97). Aneurysm formation is also accompanied by elastin network distribution, phagocyte and lymphocyte infiltration.

Ang-II infusion was assessed in wild type mice (C57Bl/6J), with AAA formation occurring in 39% of mice (98). The success rate was significantly lower than that reported in $ApoE^{-/-}$ and $LDLR^{-/-}$ mice (100% induction success). Aneurysm formation has been reported as early as 10 days post infusion and are characterized by large aortic expansion as a result of elastin degeneration (99). Histological analysis has shown a marked increase in macrophage infiltration as well as an increase adventitial tissue mass when compared to saline controls (90,95,100). In addition, microarray analysis also confirmed increase of inflammatory and extracellular modelling pathways, with markers of chemokines, MMPs and interleukin 6 upregulated (96). Mice infused for 28 days with Ang-II followed by a 56 day infusion of saline showed reduced death, as a result of aneurysm induction, and changes in aortic diameter (101). On the other hand, an 84 day Ang-II infusion has demonstrated higher incidences of ruptured deaths, aortic remodelling, tissue remodelling and macrophage infiltration. It appears that as long as Ang-II infusion is ongoing, aortic dilation continues.

Although the Ang-II model is technically simple and reflects human pathophysiology (including clinical end point i.e. aneurysm rupture), murine death is common due to aortic rupture. A meta-analysis demonstrated the mortality risk in using Ang-II model, with 20% of aneurysms rupturing during infusion (102). The risk of rupture can be attenuated by reducing the amount of Ang-II infused. It is noteworthy that the rupture observed in the model tends to be early in the aneurysm formation process relation to the microdissections that precipitate

aneurysm formation rather than large aneurysm formation and subsequent rupture as seen in human disease and therefore one must question its validity as a model of AAA rupture as opposed to aortic dissection related mortality.

1.6 AAA Pathophysiology

AAA formation is a complex process involving mass cellular remodelling, including VSMC, endothelial cells, macrophages and lymphocytes (103). The current understanding of AAA development was initially derived from study of tissue samples from subjects undergoing surgical repair. As a result, much of the analysis undertaken on these samples reflect end stage disease rather than what is occurring in the aortic wall during formation and early progression of the disease. However, the development of novel murine models (Section 1.5) has allowed some additional insights into early disease to be obtained.

Aneurysm development is characterised by four pathological observations; (i) ECM restructuring, (ii) VSMC loss, (iii) immune cell infiltration and (iv) increased oxidative stress (21). Microarray analysis of small (5-5.5 cm) and large (5.5-12 cm) aneurysm tissue showed upregulation of 840 and 1014 respectively differentially expressed genes (104). The most noticeable of genes upregulated included interleukin 6 and chemokine ligands. The analysis also showed upregulation of chemokine signalling, cancer and cytokine receptor pathways, with metabolic and VSMC contractile pathways downregulated. In addition to ECM breakdown, neovascularisation has been thought to contribute to aneurysm development. The formation of newly formed vessels in the media and adventitia has been shown to be a histological feature in AAA tissue (105,106). In addition, overexpression of key angiogenic markers such as VEGF and CD105 has also been shown (107,108).

Considerable research efforts has been focused on developing a therapeutic that could prevent continuous AAA dilation. Due to the histological finding of ECM breakdown in AAA patients, therapies targeting MMPs have been studied. The repurposing of doxycycline, an antibiotic, showed early success in reducing aneurysm growth in preclinical models of AAA (109,110). However, both the Pharmaceutical Aneurysm Stabilization Trial (PHAST) (111) and Non-Invasive Treatment of Abdominal Aortic Aneurysm Clinical Trial (N-TA^{3}CT) (112) failed to reproduce the success of preclinical trials, showing that aortic growth did not

reduce when compared to placebo control groups. An alternative focus on therapies targeting cytokines has also been assessed in preclinical models. Development of an inhibitor against interleukin-1β showed promise in limiting aortic growth (113). This in turn led to the attempt of repurposing canakinumab, a drug to treat arthritis. Similarly to PHAST and N-TA^{3}CT, the canakinumab trial was terminated as no difference was found in aortic growth between drug and placebo group (114).

Recent preclinical studies have shown targeting VSMC proliferation could provide a therapeutic intervention by repurposing tyrosine kinase inhibitors. Imatinib treatment in Ang-II and PPE murine AAA models both showed a reduction in aneurysm growth attributed to limited ECM breakdown and limited VSMC proliferation (115,116). In addition, Lenvatinib treatment in both Ang-II and PPE murine model has shown promise through reduced VSMC proliferation and maintaining VSMC structure (117). Therefore, it is important to understand the role VSMC play in aneurysm formation and progression.

In recent years, a new idea has developed that AAA formation might be driven by VSMC remodelling. VSMC are a key component of the vessel wall and maintain vascular tone through contraction and dilation. VSMCs are characterized by high plasticity, which allows phenotypic switching to occur. This describes the ability of the cells to switch from a mature contractile state to an immature, synthetic, proliferative and migratory state. Contractile VSMCs have a defined spindle like morphology and express high levels of α-smooth muscle actin (α-SMA), smooth muscle myosin heavy chain (SMMHC) and SM22-α, whereas synthetic VSMCs are rhomboidal in shape and express low levels of α-SMA and other contractile proteins. Phenotypic switching of VSMCs is prominent in vascular disorders, including AAA, and defects in smooth muscle protein genes can promote TAA (Section 1.3). Whole genome analysis of smooth muscle cells isolated from AAA showed an increase in elastolytic activity (118), whereas a meta-analysis of 6 genome wide association studies analysis studies further elucidated a number of smooth muscle pathways compromised by AAA progression (119). Further analysis showed a 2 fold increase in MMP2 RNA and a 7.3 fold increase in MMP9 RNA when compared to smooth muscle cells isolated from non-dilated abdominal aorta. VSMC phenotypic switching to express MMPs could be one of the main drivers of ECM breakdown commonly seen in AAA

subjects. In addition, the density of VSMC in AAA sections, compared to normal aortic sections, is reduced suggesting VSMC apoptosis could also be a contributor to aneurysm formation. It is important, however, to note that the contractile proteins are used as targets to stain for VSMC with antibodies, so it is possible that de-differentiated VSMC are present but not detectable with such staining. Histological analysis demonstrated that the density of VSMC in AAA tissue was 74% less than normal aortic tissue (120). Apoptotic nature of VSMC in AAA tissue was confirmed by DNA fragmentation and nuclear staining, demonstrating that VSMC loss was seen in the medial layer (121). Finally, altering of the local environment could drive VSMC to phenotypically switch. In chronic kidney disease subjects, urine in the blood is coupled with increase in oxidative stress, due to toxin release (122). This in turn induces a change in protein function and DNA, resulting in disrupting VSMC function and driving phenotypic switching. VSMC phenotypic switching in chronic kidney disease subjects can lead to expression of calcification markers. Aging of VSMC showed an increase in alkaline phosphatase (ALP), Runx-2 and collagen-1, with knockdown of all three markers deterred calcification of senescent VSMC (123).

One of the key challenges faced in detecting VSMC *in vivo* in pathological settings is the loss of expression of the key identification markers (for example α-SMA) in de-differentiated VSMC (124). Other cell types can also express smooth muscle contractile proteins such as fibroblast expression of α-SMA, leaving ambiguity in detecting de-differentiated VSMC *in vivo* (124,125). As a result, lineage tracing approaches have made use of Cre-LoxP technology to allow expression of an inducible immunofluorescent reporter gene in VSMC which persists irrespective of differentiation status (126).

1.6.1 Microcalcification

Along with the breakdown of elastin matrix and VSMC apoptosis, the presence of calcification on the arterial wall has been shown in AAA patients (83). Vascular calcification is defined as the deposition of calcium phosphate, in the form of hydroxyapatite on the vessel wall (127,128). Calcium phosphate aligns with the matrix in the form of $(Ca_8H_2(PO_4)_6).5H_2O$), which reorganizes to form calcium hydroxyapatite ($Ca_{10}(OH)_2(PO_4)_6$). This drives the formation of microcalcification deposits, which represents the unstable form of vascular calcification. However, microcalcifications can further progress to form macrocalcifications, which are the

stable form of calcification in the vessel wall, often referred as the porcelain vessel and visible on CT scans. The consensus on the properties that differentiate microcalcifications from macrocalcifications is still debated. The maximal size of microcalcifications has been reported to be 5 µm (129), 0.5-15 µm (130) and 50 um (131). Although detection of microcalcification using CT is not established, small spotty intensities have been reported in coronary artery disease (132). CT has been shown to identify macrocalcifications as small as 200 um.

Historically, calcification plaques can develop from childhood with severity increasing with age and are associated with traditional risk factors (133,134). Calcifications occur in both the medial and intimal layers of the aortic wall. Presence of calcification ultimately results in stiffening of the aorta and thus compromising function through degeneration of elastic properties (135,136). The clinical outcomes for subjects with calcified plaques in the aorta include high cardiovascular mortality, myocardial infarction and stroke. Treatment for calcified plaques include life style changes and statins.

Vascular calcification has been thought of as an end stage process in vascular disease, however the process is thought to be regulated by the presence of bone like proteins in the vessel wall (127,128). The process of calcium deposits forming on the vascular wall is thought to follow a similar process to that of bone mineralization. Mineralization begins with the invasion of osteoblasts into the extracellular matrix to facilitate the formation of the bone matrix. De-differentiated VSMCs are able to adopt an osteoblast like phenotype and express bone morphogenetic proteins (BMP) (137,138). BMP2 is a key regulator of bone mineralization. BMP2 activates upregulation of bone mineralization proteins through binding to BMP receptors and activating the Smad signaling pathway. This pathway promotes the expression of osteogenic transcription factors Runx2, Osterix and SOX9 that in turn regulate bone mineralization. Some of the key proteins regulated by transcription factors include alkaline phosphatase, osteopontin, osteoprotegerin, matrix GLA protein and SP7. Osteoblasts upregulating bone proteins promotes the deposits of calcium phosphate into the extracellular matrix and thus drives the formation of microcalcification plaques (135).

In aneurysm research, a CT study of 414 subjects demonstrated an inverse correlation between aortic diameter and extent of calcification as defined by the calcification index (139). In an individual predisposed to Marfan syndrome, microcalcification deposits were seen in the elastin layer (140). Finally, calcium deposits scored from CT data on aneurysms formed in both the abdominal and thoracic aorta were significantly associated to mortality and morbidity (141).

1.6.2 Bone proteins in AAA

1.6.2.1 Osteopontin (OPN)

OPN is a phosphorylated glycoprotein with roles associated with bone remodeling and vascular calcification (142). OPN is expressed in a variety of tissue and cell types, including cardiac tissue, bone, liver, osteocytes, VSMCs and endothelial cells (143). In atherosclerosis, OPN expression is produced as a cytokine in macrophages and T-cells, suggesting a role in modulating an inflammatory response in vascular calcification (142,143). In the process of vascular calcification, OPN loss precedes VSMC osteogenic differentiation, leading to increase in calcium deposits. OPN regulates calcium deposition through binding to $\alpha_v\beta_3$ integrins on osteoclasts, promoting cell adhesion and activation of macrophages, as well as binding to hydroxyapatite.

A potential protective role of OPN in vascular calcification has been demonstrated *in vitro* and *in vivo*. OPN added to VSMC (cultured in calcification media) inhibits calcium production (144). VSMC isolated from $OPN^{-/-}$ mice demonstrated the same phenotype as wild type VSMC, however when exposed to media containing elevated levels of phosphate, $OPN^{-/-}$ derived VSMC showed elevated levels of calcification compared to $OPN^{+/+}$ mice (145). Both studies demonstrate the protective role OPN plays in VSMC driven calcification.

OPN has been shown to potentiate Ang-II driven AAA formation. $OPN^{-/-}$ mice crossed onto a hypercholesterolaemic $ApoE^{-/-}$ background, only a single mouse (1/6) developed a AAA in response to Ang-II treatment compared to 8/9 $ApoE^{-/-}$ controls. Those that did develop AAA in the $OPN^{-/-}ApoE^{-/-}$ group demonstrated an 11% increase in aortic diameter when infused with Ang-II compared to 80% diameter in littermate controls (146). Western blot analysis on aortic tissue showed reduced expression of MMP-2 and MMP-9 in double knockout model, suggesting that the role of OPN in Ang-II model prevents aortic dilation and

reduces MMP activity. In humans, serum concentration of OPN correlated with aortic diameter and was a predictor of AAA growth post adjustment for other risk factors (142). Concentration of serum OPN from human AAA subjects was measured at 73.46 ± 43.60 ng/mL compared to 58.62 ± 43.83 ng/mL in controls. In addition, OPN serum concentration was highest in subjects with an aortic diameter between 30 - 50 mm. OPN upregulation was located in the media and adventitia of small aneurysms during histological examination.

1.6.2.2 Runx-2

Runt-related transcription factor 2 (Runx-2), also referred as Cbfa1, is a key transcription factor in regulating osteoblast and VSMC osteogenic differentiation (147,148). Deletion of Runx-2 in mice resulted in a lack of bone structure development during embryonic stages (149). Expression of Runx-2 has been shown in atherosclerotic plaques (148). In a comparison between non-calcified and calcified arteries, Runx-2, along with other markers of calcification discussed in this chapter (OPN, OPG, matrix Gla protein) were all upregulated in the presence of calcification (150). VSMC Runx-2 knockout mice attenuated the formation of calcified plaques in the vasculature in a high fat diet experiment, without loss of VSMC proteins (e.g. α-SMA) (148). Runx-2 deficiency inhibited macrophage infiltration and the formation of osteoclast cells.

In the context of AAA, $Runx2^{-/-}$ mice crossed with mice bearing an $ApoE^{-/-}$ background attenuated Ang-II induced AAA formation (151). Histological examination of the aortic tissue showed reduced elastin degradation and microcalcification formation compared to Ang-II induced AAA aortic tissue. The full role of Runx2 in AAA development, however, is still not fully understood

1.6.2.3 Bone Morphogenetic Protein 2

The Bone Morphogenetic Protein (BMP) family, including BMP2, BMP4 and BMP7, is a subfamily of the transforming growth factor-β (TGF- β) family (152,153). BMP induced osteogenic formation through binding to BMP receptors, which in turns phosphorylates and activates Smad pathway to maintain bones and tissue. Although the function of BMP2 has not been studied in AAA formation or growth, the role has been studied in atherosclerosis.

Expression of BMP2 has been found at the base of atherosclerotic plaques as well as calcification sites away from plaque formation (154). Cells cultured from

plaques demonstrated bone like nodules, confirmed by alizarin red and Von Kossa stain. Atherosclerotic plaque biopsies from abdominal aorta showed increased BMP2 expression in the adventitia but not in non-diseased area of the aorta (155). Addition of BMP2 enhances calcification of cultured human aortic smooth muscle cells, independent of phosphate concentration (156). BMP2 has also shown to inhibit VSMC proliferation (157) as well as promoting macrophage infiltration into atherosclerotic plaques (158,159).

1.6.2.4 Osteoprotegrin (OPG)

OPG is a member of the tumour necrosis factor receptor family and regulates bone formation, similar to OPN (160). OPG prevents osteoclast differentiation and activation through binding to RANKL (161). High concentration of OPG in serum has been shown to be a risk factor of cardiovascular events (for example coronary artery disease, myocardial infarction and carotid atherosclerosis), as well as a predictor of future cardiac events and mortality (160,162–165).

Western blot analysis of human AAA tissue (taken from surgical biopsy) demonstrated OPG concentration was 3 times greater than in atherosclerotic aorta tissue and 8 times greater than tissue from the no diseased segment of abdominal aorta (160). Cultured VSMC were driven to an aneurysmal phenotype through the addition of endogenous OPG. Reduced cell proliferation, increased MMP-9 and apoptosis characterized the change in VSMC phenotype. Serum OPG concentration has also shown to be correlated with an increase in aortic diameter (165).

$OPG^{-/-}ApoE^{-/-}$ mice infused with Ang-II showed reduced aortic dilation as well as a reduced risk of rupture (63% compared to 94% in $OPG^{+/+}ApoE^{-/-}$ littermates) (166). In the $OPG^{-/-}ApoE^{-/-}$ model abdominal aorta, levels of cathepsin S, MMP-2 and MMP-9 were reduced after 7 days of Ang-II infusion when compared to baseline measurements. The data suggested that OPG could be involved in an early inflammatory response to Ang-II infusion. In addition, $OPG^{-/-}$ mice undergoing $CaCl_2$ induced AAA showed an increase in aortic diameter, with elastin fibre destruction determined by histology examination (161). Aneurysm induction coincide with upregulation of tumour necrosis factor related apoptosis inducing ligand (TRIAL), which *in vitro* investigation demonstrated OPG inhibited TRIAL. Therefore, $CaCl_2$ induced aneurysms could be attenuated through OPG

inhibition of TRIAL. The contrast in aneurysm development between the two models has been suggested to be as a result of increased fibrotic remodelling in the Ang-II model preventing aortic dilation (167).

The role of OPG as a therapeutic has also been investigated in preclinical aneurysm models. OPG treatment of $CaCl_2$-driven AAA in C57Bl/6J mice appears to have no impact on aneurysm growth (168). However, it does correlate with an increased concentration in collagen in the aortic wall, as well as a marked wall thickness increase, as demonstrated through histology. This suggests that OPG could act to stabilise the vessel wall in AAA. Alternatively, activation of peroxisome proliferator-activated receptor – γ (PPARγ) through pioglitazone administration reduced OPG expression and Ang-II induced AAA formation in mice bearing an $ApoE^{-/-}$ background (169). Nominally in the Ang-II model, OPG is upregulated in response to aneurysm formation and confirmed in VSMC assay through endogenous addition of OPG and Ang-II. Targeting PPARγ could provide a therapeutic intervention.

1.7 Imaging Modalities

1.7.1 Ultrasound

Ultrasound (USS) is an important medical imaging modality that is used frequently in cardiovascular examination, especially in AAA diagnosis and screening. USS is cheap, non-ionising and can be easily transported to bedside although lacks depth of penetration and only supplies primary anatomical information (170,171). The ultrasound probe (also referred to as a transducer) generates the ultrasound wave through conversion of electrical signals. The ultrasound wave travels through the target. The ultrasound wave is then reflected back to the transducer by anatomical structures. Different tissue types, such as soft tissue, air, fluids and solid tissue, vary in density and therefore may reflect more or fewer sound waves compared to one another. For example, fluid is less dense than solid landmarks, and therefore reflect less sound waves than solid landmarks. The reflected ultrasound waves are detected by the transducer and converted back to an electrical signal. The electrical signal is processed into an image. Nominally, USS uses 2D b-mode (brightness mode) to image a slice in the target of choice.

1.7.2 Computed Tomography (CT)

CT is a 3D anatomical x-ray technique which separates different tissue through x-ray attenuation (170,172). The x-ray source and detector normally rotate around the target with the x-ray fanbeam spanning the target. Similar to ultrasound, density of tissue reflects the amount of x-rays absorbed. The amount of x-rays absorbed by a tissue is defined by Hounsfield units and reflects the difference between tissue density and composition. Dense tissue, such as bone, strongly absorbs x-rays so appears white in the reconstructed image, whereas air does not absorb x-rays and appears dark on the images. The vasculature, including the thoracic and abdominal aorta (173) can be enhanced using a contrast agent to detect abnormalities, including aneurysms (174). As mentioned in section 1.6.1, CT detection of calcification reflects macrocalcification not microcalcification deposits, these are bone-like and appear white.

1.7.3 Positron Emission Tomography

PET is an imaging technology that utilises a radioactive imaging probe to target and report an *in vivo* biological process at the molecular level in a specific anatomical location (170,175). PET can be used for detecting early stage and progression of disease as well as studying the effects of drugs. Clinically, PET has been successfully integrated clinically in the field of oncology, with some neurology and cardiac applications reported. PET imaging probes incorporate a positron emitting atom into a chemical compound, with each positron emitting atom differing in half-life and positron range. PET imaging probes are termed radiotracers (176). A known dose of radioactivity is injected intravenously into the patient and localises to regions where the biological process(es) reported by the radiotracer are happening. For example, 2-[^{18}F]-FDG, the most clinically relevant radiotracer, is a radiolabeled analogue of glucose and a marker of hypermetabolism. 2-[^{18}F]-FDG localizes to areas of hypermetabolism through GLUT4 transporters (177). However, unlike it's analogue glucose, 2-[^{18}F]-FDG remains trapped in cells after phosphorylation by hexokinase. The application of 2-[^{18}F]-FDG has had great success in oncology (178–180) and neurology (181) and is seen as the gold standard for detecting carcinomas. On the other hand, Na[^{18}F]F (the focus of this thesis) reflects tissue that contains calcium hydroxyapatite (calcification) and therefore accumulates in the bone and tissue with progressive microcalcification. The location of radiotracer accumulation is

detected through the generation of gamma rays as a result of positron decay. The positron emitting nuclei decays by emitting a positively charged particle (positron). The positron travels a short distance before it annihilates with an electron. The product of the annihilation are two acolinear 511 keV gamma rays, roughly 180° apart. The gamma rays are detected by a ring of detectors and a line of response is generated where the annihilation occurred. The electrical signals from the annihilation products that occur are stored into a sinogram, that once reconstructed provides an image. PET images are corrected for random, scatter and attenuation gamma ray events. PET scanners are nominally coupled with CT scanners (or more recently with MR scanners) to provide anatomical reference and attenuation correction in the image reconstruction step.

Radiotracers can be labelled with a number of different radioisotopes that differ in half-life, mode of decay and positron range. Longer lived radioisotopes, although currently not used in the clinic, allow for longitudinal tracking of the radiotracer. The most commonly used radioisotope is [^{18}F] due to its advantageous properties for example short half life and short positron range.

1.7.3.1 PET image analysis

Quantification of PET/CT images is important to identify localisation of radiotracer in diseased tissue to inform disease. Normally, visual inspection of PET/CT is used in the clinic to inform whether a disease is present or not (182). However, quantification maybe needed to inform, for example, response to treatment. Accurate quantification relies on correct delineation of the area of interest, with the defined region of interest (ROI) encompassing the full region without incorporating background radioactivity (183). This can be from local tissue structures that have high uptake of the radiotracer of interest or regions that have high background signal.

There are three main methods implemented in the quantification of radiotracer uptake in PET/CT images. Standardised uptake value (SUV) is the main value expressed in PET/CT studies and is described by Equation 1. Both SUV_{mean} and SUV_{max} are quoted in the literature. SUV_{mean} represents the mean SUV value across the defined ROI whereas SUV_{max} represents the maximal SUV value in the defined ROI. Although SUV is predominately used, there are many confounds in obtaining an accurate measurement (182,184,185). This can be split into two

categories, physiological and technical. Physiological confounds include patient weight, motion and metabolism. Technical limitations include radioactive calibration between PET scanner and dose calibrator, time of injection vs time of imaging study and the assumption of fast radiotracer clearance from the blood. In addition, factors such as the scan and reconstruction protocol can affect accurate SUV quantification. There is considerable effort to minimise the effects that can contaminate SUV quantification. For example, patients undergoing 2-[^{18}F]F-FDG scan are asked to fast 6 hours prior to their scan to minimise glucose levels.

A confound in measuring SUV in some studies, in particular in vascular applications, is SUV will also incorporate the measurement of background radiation, thus adding a source of contamination in the signal (183). As a result, tumour to background ratio (TBR), defined by Equation 2, takes into account the SUV measured in the blood pool. Although TBR theoretically offers removal of contaminant signal, there is the argument that further contaminants are incorporated in the measurement due to the aforementioned confounds of SUV.

The final measurement of radioactivity is percentage injected dose per gram (%ID/g) and is defined by Equation 3 (186). Image derived %ID/g is limited as definition of the weight of the defined ROI is unknown. However, %ID/g is useful in *ex vivo* gamma counting of tissue, as the weight of the tissue of interest is known.

Equation 1: Standard Uptake value (SUV)

$$\boldsymbol{SUV\ (g/mL) = \frac{Radioactivity\ in\ ROI\ (\frac{MBq}{mL})}{\frac{Injected\ radioactivty\ (MBq)}{Body\ mass\ (g)}}}$$

Equation 2: Tumour to background ratio (TBR)

$$\boldsymbol{TBR = \frac{SUV\ of\ tissue\ of\ interst}{SUV\ of\ blood\ pool}}$$

Equation 3: Percentage injected dose per gram (%ID/g)

$$\boldsymbol{\%\,ID/g\ (MBq/g) = \frac{Radioactivity\ (MBq)}{Weight\ of\ tissue\ (g)}}$$

1.8 PET Radiotracer applications in Vascular Disease

1.8.1 PET in cardiovascular disease

1.8.1.1 2-[^{18}F]-Fluorodeoxyglucose

As mentioned in section 1.7.3, 2-[^{18}F]-FDG is a radiolabeled analogue of glucose and a marker of hypermetabolism and locates in cells with hypermetabolic activity. The reported success of implementing 2-[^{18}F]-FDG in cardiac diagnosis has been varied. In a cohort of coronary stenosis subjects, 2-[^{18}F]-FDG uptake correlated with macrophage infiltration observed by histological staining (187). The result suggested a possible indication that 2-[^{18}F]-FDG could detect inflammatory remodeling in atherosclerotic plaques. In addition, in a large vessel vasculitis cohort, uptake of 2-[^{18}F]-FDG was 93% specific and 76% sensitive in correctly detecting large vessel vasculitis (188). However, there has been some confounding results, especially in atherosclerosis, questioning the role of 2-[^{18}F]-FDG as a marker of inflammation.

1.8.1.2 [^{18}F]-Sodium Fluoride

A key feature of vessel wall remodelling in response to injury is the deposits of microcalcification (as described in Section 1.5.1). Detection of microcalcification, described as calcium hydroxyapatite ($Ca_{10}(PO_4)_6OH_2$), using PET imaging is achieved through injection of [^{18}F]-Sodium Fluoride (Na[^{18}F]F). Na[^{18}F]F was developed primarily to detect bone metastasis and other bone diseases (e.g. osteomyelitis) (189,190), however there has been recent advancement in applying Na[^{18}F]F in cardiovascular disease in light of the realisation of the relevance of vascular calcification to disease prognosis.

Na[^{18}F]F is carried by the blood to the detection site. Here, Na[^{18}F]F can diffuse through the capillaries into the extracellular space occupied by the bone, or bone like structures, and binds to the surface. Na[^{18}F]F localises in regions of microcalcification through the exchange of [^{18}F]- ions with [OH]- ions in the calcium hydroxyapatite structure. This process can be explained through a classical 3 compartment model, where the rate constant k_3 describes ion exchange and accumulation of Na[^{18}F]F. Accumulation of Na[^{18}F]F in regions of microcalcification is seen 60 minutes post injection (191).

Validation of Na[^{18}F]F uptake in microcalcification has been extensively reported. 11 patients with carotid plaques elected for endarterectomy were imaged with Na[^{18}F]F and excised plaques were stained with Goldner's trichome, a marker of hydroxyapatite (192). Na[^{18}F]F uptake was greatest in the carotid plaques in subjects with recorded symptoms (e.g. stroke) compared to subjects with no symptoms. In addition, Na[^{18}F]F uptake correlated with Goldner's trichome staining ($r=0.45$, $p<0.001$). Confirmation of Na[^{18}F]F binding reflecting microcalcification as opposed to macrocalcification was shown using excised carotid plaques (193). PET/CT investigation showed Na[^{18}F]F exclusive binding to microcalcification was due to hydroxyapatite structure having a higher surface area when compared to macrocalcifications. In a study of 75 subjects, 12% of subjects demonstrated detectable calcified plaque by CT and Na[^{18}F]F uptake, whereas 75% of subjects showed Na[^{18}F]F uptake with no detectable plaques from CT (194). Therefore, Na[^{18}F]F uptake reflects the active remodelling, as presented by microcalcification, opposed to stable calcification deposits which are detected by CT.

Application of Na[^{18}F]F in vascular diseases has been well reported with studies in aortic stenosis, atherosclerosis and peripheral arterial disease (PAD) have shown promise. In a study of 121 subjects with differing stages of calcified aortic stenosis, Na[^{18}F]F uptake, when compared to 2-[^{18}F]-FDG uptake, increased with progression of disease (195). Na[^{18}F]F uptake was observed in regions away from calcium structures seen on CT, further suggesting Na[^{18}F]F detects active microcalcification remodelling. Na[^{18}F]F activity could also predict further calcification development in aortic stenosis subjects (196). This study indicates the role of Na[^{18}F]F could have in predicting future therapies for aortic stenosis subjects.

Evidence of Na[^{18}F]F in detecting atherosclerotic plaques has been reported. In a cohort of myocardial infarction subjects with carotid plaques (n=40), 93% of subjects showed marked Na[^{18}F]F uptake (197). Na[^{18}F]F was able to differentiate between culprit plaque (TBR = 1.66) and non-culprit plaque (TBR = 1.24). Uptake correlated with histological features of microcalcification, necrosis and macrophage infiltration. Na[^{18}F]F has shown the potential to predict subjects who are at risk of a coronary event (e.g. acute coronary syndrome) (198).

Finally, the prognostic value of Na[^{18}F]F PET imaging in vascular disease has been shown in subjects with PAH undergoing angioplasty procedure (199). Baseline Na[^{18}F]F uptake was highest in subjects who developed restenosis post angioplasty. This study demonstrated an early indication of the prognostic value of Na[^{18}F]F in detecting subjects who might be at risk post-surgery.

1.8.2 PET in AAA

1.8.2.1 2-[^{18}F]-Fluorodeoxyglucose

As discussed in Section 1.5, an early hypothesis derived from histological staining of end-stage AAA tissue showed an influx of macrophages, suggesting an immune driven response to wall remodeling. Initial reports studying the potential role of PET/CT imaging in AAA stratification used 2-[^{18}F]-FDG as a marker of macrophage infiltration. 2-[^{18}F]-FDG is a radiolabeled analogue of glucose and a marker of hypermetabolism. The role of 2-[^{18}F]-FDG, in particular in cardiac imaging, is confounded by both the presumed ability of 2-[^{18}F]-FDG to detect regions of inflammation and the non-specific uptake by other metabolic cells contributing to vessel wall remodeling, such as VSMC (200).

There has been much interest in using 2-[^{18}F]-FDG to detect macrophage infiltration in AAA subjects. However, the results are confusing and conflicting. This suggests that 2-[^{18}F]-FDG may not reflect solely macrophage infiltration and there could be another metabolic pathway contributing to the observed signal (201). A single PET study, using tissue samples from surgical intervention for histological analysis, showed that subjects with a PET positive scan (2-[^{18}F]-FDG uptake) had marked increase in macrophage infiltrates in the medial layer (202). The correlation however was only seen in 12% of participants and other upregulated markers of wall remodeling (VSMC death) could affect 2-[^{18}F]-FDG uptake. Although disease progression was observed, with an increase in lymphocyte and Ki-67 markers observed, the cohort of subjects observed were asymptomatic AAA; subjects presenting with no abdominal pain. However, two studies have reported that subjects presenting with none to low uptake of 2-[^{18}F]-FDG have large upregulation of macrophage markers defined by histology (203,204). From the reported evidence in the literature, the link between 2-[^{18}F]-FDG and macrophage infiltration could be non-specific or determined by other factors (200). These factors could include the contribution of other

metabolically active cells, such as VSMCs, endothelial cells and fibroblasts, contributing to wall remodeling at the time of PET/CT investigation and comparison between symptomatic and asymptomatic subjects.

In addition, the relationship between uptake of 2-[^{18}F]-FDG and AAA progression (aortic growth) and clinical presentation (symptomatic vs asymptomatic) has been studied to validate the role 2-[^{18}F]-FDG PET/CT could play in patient prognosis. The reported evidence on this relationship is, however, contradictory. In a cohort of both symptomatic and asymptomatic subjects (n=23), uptake of 2-[^{18}F]-FDG was able to discriminate between symptomatic and asymptomatic subjects (204). Measured values of both SUV_{max} and SUV_{mean} in symptomatic subjects were twice than that measured in asymptomatic subjects. In a follow up study, AAA subjects were invited to two PET/CT scans 9 months apart to study the relationship between aneurysm growth and baseline 2-[^{18}F]-FDG scans (205). Subjects with low baseline 2-[^{18}F]-FDG uptake, defined by SUV_{max}, had the largest increase in aortic diameter. Although this early study showed promise in the role 2-[^{18}F]-FDG could play in patient prognosis, both positive and negative correlation between PET quantification metrics and aortic growth have been reported (206–208).

Although the evidence for using 2-[^{18}F]-FDG as a tool for predicting aortic growth is not convincing, there has been some small pilot work in detecting complications after surgical procedures and correlations with other imaging modality metrics. In a follow up study of AAA subjects at the EVAR intervention threshold, subjects were split between pre-intervention and follow up imaging or just post-surgery imaging (209). 35% of subjects who underwent pre-intervention PET/CT scan had noticeable uptake in aneurysmal wall. Of this cohort, 83% of subjects developed type II endoleaks 1 year post EVAR, with 2 subjects reported with continued sac growth. In the post-surgery cohort, a correlation was found between sac growth, type II endoleaks and SUV. In a similar study, AAA subjects planned for EVAR were invited for pre-intervention 2-[^{18}F]-FDG scan and follow up at 1 month and 6 month post procedure (210). Subjects with a low 2-[^{18}F]-FDG uptake at baseline but high uptake at 6 months presented with poor sac shrinkage. Similar results have been shown in an aneurysm subjects with Marfan’s syndrome undergoing aortic arch graft repair (211). High uptake 2-[^{18}F]-FDG uptake further diagnosed the subject with arteritis (inflammation of

the arterial wall). Although further research is required to study the role of 2-[^{18}F]-FDG in detecting complications post intervention, the current literature shows possibility of this approach.

There are a few reported studies looking at the application of 2-[^{18}F]-FDG in TAA subjects. Subjects with diagnosed giant cell arteritis (GCA) had a significant uptake of 2-[^{18}F]-FDG and larger aortic diameters and volumes compared to GCA subjects without uptake (212). Acute aortic syndrome subjects with a PET positive 2-[^{18}F]-FDG signal at baseline showed increased disease progression or required intervention at follow up (213). Lack of PET research in TAA could be a result of lack of a specific marker for tailored patient therapy and limited clinical applicability.

1.8.2.2 [^{18}F]-Sodium Fluoride

An important development in AAA PET imaging was the results of the SoFIA^3 Trial (83). 72 AAA subjects and 20 controls were imaged with Na[^{18}F]F. Tumour to blood ratio (TBR) measurements could differentiate between AAA subjects and controls. However, the main finding was that Na[^{18}F]F could predict aneurysm growth and progression to a clinically relevant endpoint (e.g. repair or rupture) independent of classical AAA risk factors (e.g. age, aneurysm diameter and smoking). The SoFIA3 trial was the first to report a clinical application of a PET tracer as a potential stratification biomarker which could accurately predict growth and clinical endpoint. The trial also showed co-registration of Na[^{18}F]F uptake with von kossa *ex vivo* histology. Although there is promise shown from the SoFIA trial, the recruited AAA subjects represented late stage AAA (mean AAA diameter of 4.8 cm). Further investigation into the uptake of Na[^{18}F]F across the full AAA diameter range is needed to fully determine the diagnostic capability of Na[^{18}F]F. Although the evidence from the SoFIA3 trial suggests microcalcification as detected by Na[^{18}F]F PET/CT is relevant to AAA progression, the origin of bone deposits in the vascular wall is unclear. There are limited studies that have looked specifically at this link. A global Runx2 smooth muscle cell knockout murine line, back crossed with an ApoE$^{-/-}$ murine line, showed aneurysm attenuation and no presence of microcalcification using the Ang-II AAA model (151).

1.8.2.3 Markers of Angiogenesis

Although the bulk of PET/CT AAA research has focused on repurposing currently validated radiotracers that have had success in other disease areas, there has been some interest in looking at other markers of disease progression to evaluate their use in AAA prognosis and stratification. In particular, radiotracers that have been developed specifically to target angiogenesis in oncology have been investigated in preclinical and *ex vivo* AAA studies. Although the role of angiogenesis in AAA progression and development is not fully understood, there is evidence of the over expression of the integrin heterodimer $\alpha_v\beta_3$, VEGF, CD31 and CD105 through histological examination and mRNA analysis (105,106,108).

A single study reported the specificity on the angiogenic radiotracer [^{18}F]-Fluciclatide in *ex vivo* human AAA tissue samples (214). The specificity of [^{18}F]-Fluciclatide, a marker of $\alpha_v\beta_3$, was compared to other radiotracers, that were non-specific to other hallmarks of AAA progression, using autoradiography. [^{18}F]-Fluciclatide binds to $\alpha_v\beta_3$ by targeting the RGD (arginine-glycine-aspartate) domain expressed by integrin heterodimers. Results from the autoradiography study demonstrated only [^{18}F]-Fluciclatide showed specific uptake (88%). [^{18}F]-Fluciclatide could be an attractive tracer to study in clinical studies, with uptake in atherosclerotic plaques correlating with plaque volume and plaque wall thickness. In comparison, the RGD radiotracer [^{18}F]-FPPRGD2 showed specific uptake in the Ang-II murine AAA model when compared to shams (% ID/g 2.05 vs 0.63 respectively) (215). Uptake was confirmed with autoradiography and correlated with increased expression of CD31.

A single study also showed the repurposing of the CD105 Fab radiotracer, a detector of endoglin expression as a result of angiogenesis, in the $CaCl_2$ model in BALB/c mice (216). Maximal uptake was seen at day 7 post surgery when compared to baseline and day 20 post surgery (% ID/g baseline = 2.5 ± 0.1, day 7 = 11.1 ± 0.2, day 20= 4.5 ±0.5). Uptake was confirmed *ex vivo* gamma counting and autoradiography. Similar to studies with RGD tracers, early studies show the potential of angiogenic tracers in human studies. However, there's still a lack of understanding of the role angiogenesis plays in human AAA progression and the link with clinical end points. In addition, the use of Ang-II and $CaCl_2$ animal models do not fully reflect human pathology.

1.8.2.4 Proliferation

As described in Section 1.5, VSMC show remarkable plasticity in response to injury and can switch from a contractile state to a proliferative and synthetic state. Therefore, repurposing 3-[^{18}F]-Flurothymidine (3-[^{18}F]-FLT), a novel marker of proliferation used in oncology (217,218), in detecting possible AAA growth is sensible. Uptake of 3-[^{18}F]-FLT follows a similar 2 compartmental pathway as 2-[^{18}F]-FDG; 3-[^{18}F]-FLT is transported by pyrimidine salvage pathway and phosphorylated by thymidine kinase-1 (TK-1), thus trapping within the cell of interest (177). A single preclinical study, utilizing the Ang-II AAA model, demonstrated that uptake correlated with the active growth phase of aneurysm progression (73). SUV_{max} measurements peaked day 14 post Ang-II infusion and reducing at day 28. Biodistribution studies further demonstrated peak uptake in harvested abdominal aorta compared to sham models. Studies looking into cell specific uptake of 3-[^{18}F]-FLT are required to demonstrate VSMC specific remodeling and therapeutic response investigation, however, the early results warrant investigation in clinic (219).

1.9 Research hypotheses, aims and objectives

A substantial amount of the presented literature suggests that our understanding of the progression and treatment of AAA is based on historical trial data. Much of our knowledge has changed and there is need to provide both better tools for patient management, and personalised medicine.

It is clear that there is an association between aortic size and rupture risk, but current ultrasound methods do not provide a clear map for patient management. A complementary imaging strategy, that could accurately predict subjects at a greater risk of rupture or in need of specialised therapy, such as PET/CT, would be a potentially valuable tool in the clinical pathway. The hypothesis to be tested in this thesis is to complement the findings of the SoFIA trial (83) with a reverse translational study to determine if Na[^{18}F]F uptake is a suitable biomarker to detect aneurysm progression in a preclinical model and determine the cellular contribution to microcalcification development. The objectives are as follows:

i. Evaluate the use of Na[^{18}F]F as a detector of AAA and AAA progression in a preclinical model.
ii. Determine the key markers of calcification involved in AAA progression in the PPE model and the specific cell type expressing osteogenic proteins.
iii. Investigate the application of novel reconstruction methods and assess the effects of different region of interest (ROI) definitions.

Chapter 2

Methods

2.1 Reagents

Table 2: List of Chemicals

Name	Product Code	Supplier
Triton™ X-100	X100-1L	Sigma
Absolute Ethanol	BP2818-500	Fisher
Calcium Chloride Dihydrate	C5080-500G	Sigma
Disodium hydrogen phosphate	0585971	Fisher
Sodium dihydrogen phosphate	0938117	Fisher

Table 3: List of Antibodies

Antigen	Host Species	Clonality	Concentration	Supplier	Catalogue number
Bone morphogenetic protein – 2 (BMP2)	Rabbit	Monoclonal	1:100	Abcam	ab214821
Bone morphogenetic protein – 4 (BMP4)	Mouse	Monoclonal	1:100	Merck	MAB1049
Osteoprotegerin (OPG)	Mouse	Monoclonal	1:100	Novus	NBP2-76903
Runx2	Rabbit	Monoclonal	1:200	Abcam	ab192256
α-smooth muscle actin	Mouse	Monoclonal	1:200	Agilent Dako	M0851
Alexa Fluor 514	Goat	N/A	1:500	Invitrogen	A31558
Alexa Fluor 647	Chicken	N/A	1:500	Invitrogen	A21472
Prolong Gold Antifade Reagent with DAPI	N/A	N/A	N/A	Invitrogen	P36931

Table 4: CT Angiography contrast agent

Product name	Supplier	Product code
ExiTron nano 12000	Miltenyi Biotec	130-095-698

Table 5: Cell Culture Reagents

Product Name	Supplier	Product code	Supplementation
DMEM (1X) + GlutaMAX™	Gibco	31966-021	10% fetal bovine serum (FBS) 1% penicillin/streptomyosin
Dulbeco Phosphate Buffered Saline	Sigma	D8537-500ML	N/A
Recombinant Human PDGF-BB Lyophilized	Gibco	PHG0045	N/A

Table 6: Surgical chemicals

Product Name	Supplier	Product Code
Elastase from porcine pancreas	Sigma	E1250-50MG

Table 7: ELISA Kits

Antigen	Species	Supplier	Product Code
Osteoprotegerin	Human	R&D Systems	DY805
Osteopontin	Human	R&D Systems	DOST00
BMP-2	Human	R&D Systems	DBP200

Table 8: qPCR Primers

All primers are intron spanning unless stated otherwise.

Gene of interest	Protein	Clonality	Code
ACTA2	Alpha-smooth muscle actin	Human	qHsaCID0013300
BMP2	Bone morphogenetic protein 2	Human	qHsaCID0015400
BMP4	Bone morphogenetic protein 4	Human	qHsaCED0003208 Exonic
SPP1	Osteopontin	Human	qHsaCID0012060
TNFRSF11B	Osteoprotegerin	Human	qHsaCID0013204
Runx2	Runt-related	Human	qHsaCID0006726
GAPDH	Glyceraldehyde 3-phosphate dehydrogenase	Human	qHsaCED0038674 Exonic

2.2 Animal Husbandry

All work undertaken using animal models was conducted in alignment with the UK Home Office Animals Scientific Procedures Act 1986 and 3 R's principle under project license P606320FB (expiry date: 16th September 2021) and PP8169223 (expiry date: 4th August 2026), PIL license IDD2542A4.

2.2.1 C57Bl6/J

Male C57Bl6/J mice were purchased from Charles River (UK) or supplied by the in house breeding facility at the University of Leeds. Mice were housed in a conventional containment animal facility at the University of Leeds. A maximum of five mice per cage were kept in GM500 ventilated cages at 21 °C with a 12-hour light/dark cycle. The mice diet consisted of a RM1 chow pellet feed (special diet services) and triple-filtered water via Hydropac pouches *ad-librium*. Two chew sticks and a small plastic animal sheltered dome were supplied in each cage as environmental enrichment. Animals were identified using conventional ear notching. All mice were checked daily by a dedicated animal technician. The total number of C57Bl6/J mice used in this study is 30.

2.2.2 mTmG VSMC lineage tracing transgenic line

Mice harbouring a VSMC conditional mTmG fluorescent reporter were used for PPE induced AAA lineage tracing studies (220). mTmG mice were originally obtained from Jackson Laboratory (Jax strain: 007576). mTmG mice harbour a membrane targeted fluorescent Tomato probe (mTom) followed by a STOP codon, flanked by LoxP sites and downstream membrane bound green fluorescent protein (mGFP). These were crossed with SM-MHCCreERT2 (Jax strain: 019079) mice which express Cre in VSMC upon tamoxifen injection. Upon activation of Cre recombinase (by tamoxifen induction in these animals), the mTom is excised to reveal the downstream mGFP expression. Housing, diet and welfare as described in Section 2.2.1. These mice were generated separately for a BHF Project Grant.

2.2.3 Experimental interventions

All surgical AAA procedures were performed in a dedicated murine operating facility under sterile conditions under isoflurane anaesthesia by Dr Marc Bailey. Mice were anaesthetised with 5% isoflurane induction and weighed pre-

procedure. During the procedure mice were maintained at 37 °C and at 2% isoflurane in O_2 at a flow rate of 2 L/min on a heated down-draft operating table. Mice were injected intraperitoneally with 100 µL buprenorphine analgesia. Laparotomy of the abdomen and dissection of the infra-renal abdominal aorta were performed using an OPMI Pico operating microscope (Zeiss). The aorta was cleaned for peri-vascular fat and adventitia dissection. Post-procedure, abdominal wounds were closed using 6-0 Vicryl (Ethicon) sutures (peritoneum) and 4-0 Vicryl (Ethicon) sutures (skin) before full recovery at 37 °C on heated recovery platform. Once mice were fully recovered they were returned to their home cage.

Mice receiving PPE: 10-week-old male C57Bl6/J mice were laparotomised and pure PPE (10 µL, concentration = 0.5 - 15 mg protein/mL) was applied to the adventitia of the abdominal aorta for 5 minutes. The abdomen was washed three times with PBS before wound closing. This model applies to mice undergoing experiments described in Sections 2.3-2.5.

Mice receiving $CaCl_2$: 10-week-old male C57Bl6/J mice were laparotomised and a piece of cotton bud tip soaked in $CaCl_2$ (0.5 M) was applied to the adventitia of the abdominal aorta for 15 minutes. The abdomen was washed three times with PBS before wound closing. This model applies to mice undergoing experiments described in sections 2.3 and 2.4.

Sham receiving: 10-week-old C57Bl6/J mice were laparotomised and washed with PBS three times before wound closing. This model applies to mice undergoing experiments described in sections 2.3-2.5.

All mice underwent additional checks post-surgery and were fed a soaked diet for two days before returning to chow pellet feed described in section 2.1. Mice were weighed weekly following surgery. Any animals showing signs of distress or losing more than 15% of their starting weight were culled by a Sch1 method to prevent suffering.

2.3 *In vivo* imaging

Figure 2 outlines the *in vivo* imaging scheme for each dedicated study. Scheme 1 describes the workflow for ultrasound, PET/CT and biodistribution studies in day 14 PPE and $CaCl_2$ model. Scheme 2 describes the workflow for PET/CT and

CTA in longitudinal PET/CT study in the PPE model. Finally, scheme 3 describes the workflow for biodistribution study at day 7 in the PPE model.

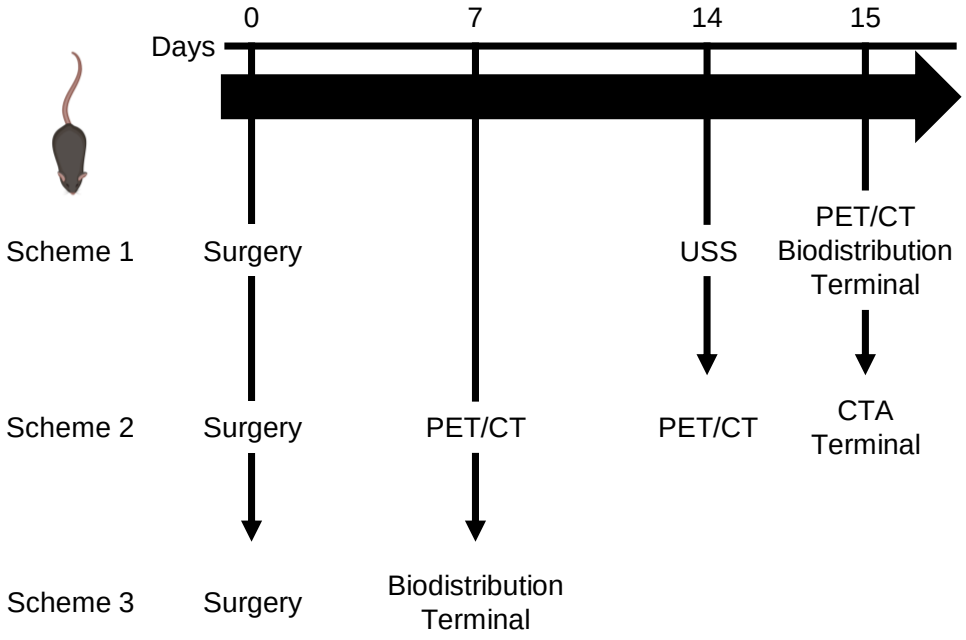

Figure 2: Experimental design for preclinical imaging investigation of Na[^{18}F]F uptake in sham vs PPE AAA model in 10-week-old C57Bl/6 mice. USS, ultrasound scan; PET/CT, positron emission tomography coupled computed tomography; CTA, computed tomography angiography.

2.3.1 Ultrasound

To confirm induction of AAA through detection and measurement of the aortic diameter and volume, B mode ultrasound imaging (Vevo 2100 imaging system) was performed 14 days post-surgery (78). Prior to imaging, the hair from the abdomen was removed by shaving and Veet^{TM} de-epilatory cream. Ultrasound imaging was performed using the MS-550D transducer at 40 MHz frequency. Mice were anaesthesed through 5% isoflurane induction and maintained at 2% isoflurane in O_2 at a flow rate of 2 L/min. Mice were placed supine on a heated table. Heart rate and respiration were monitored through electrodes on the heated table with conductive cream applied to each paw and temperature was monitored using a rectal probe. Aquasonic clear ultrasound transmission gel (Parker labs) was applied to the abdomen before lowering the transducer for imaging. A 2-D ECG-gated kilohertz visualisation (EKV) image was taken at the maximal aortic diameter. A 3-D transverse image was undertaken across a 12 mm region of interest, starting from the right renal artery in the inferior direction. 157 frames at

0.076-mm intervals gated for respiration with electrocardiographic triggering at 50 ms after the r-waves were acquired. Images were reconstructed and analysed for volumetric quantification using Vevo Lab v.1.7.0 as described in Waduud *et al* (78). Waduud *et al* measured the interobserver mean difference in aortic diameter calculation as -0.05 mm (Limits of agreement (LOA) 0.14 mm - 0.24 mm, p=0.1) and intraobserver mean difference as -0.03 mm (LOA 0.16 mm - -0.21 mm, p=0.36). The interobserver mean difference in aortic volume was measured as -1.38 mm^3 (LOA 1.58 mm^3 - -4.34 mm^3, p=0.008) and intraobserver mean difference in aortic volume was measured as -0.55 mm^3 (LOA 1.19 mm^3 - -2.28 mm^3, p=0.053).

2.3.2 micro-Computed tomography angiography (CTA)

To confirm induction of AAA through detection of the aorta and measurement of aortic volume, CTA was performed on the Bruker µCT SkyScan 1176 (Bruker, Belgium). Mice were anaesthesia through 5% isoflurane induction and maintained at 2% isoflurane in O_2 at a flow rate of 2 L/min. To visualise the vasculature, mice were injected through the lateral tail vein via a catheter with 100 µL ExiTron Nano 12000 (Miltenyi Biotec) at a flow rate of 100 µl/minute and flushed with saline. Mice were laid prone on the CT bed and respiration was monitored throughout the imaging experiment for animal welfare. Images were acquired with a 0.5mm aluminium filter (voltage 50 kV, current 476 uA), rotation step 0.7 ° and a spatial resolution of 35 µm. A scout scan was performed to check animal positioning and the scan region (skull to ankles, 4 fields of view) was defined.

CTA images were reconstructed in NRecon (version 1.7.5.9) using a Feldkamp reconstruction algorithm (smoothing = 4, ring artefact correction = 4, beam hardening correction = 40%). The abdominal aorta was segmented starting from the right renal artery in the inferior direction across a 12 mm region of interest, and analysed for volumetric quantification in CT Analyser (CTan) (version 1.18.1.0).

2.3.3 Micro Positron Emission Tomography and Computed Tomography

Na[^{18}F]F was prepared and supplied by the University of Manchester and University of Hull.

For initial model establishment studies (Figure 2; scheme 1), mice (at day 15 post AAA induction) were imaged on the Albira Si µPET/SPECT/CT scanner (Field of view = 40 mm, spatial resolution = 1.55 mm, sensitivity = 2%) (Bruker, Belgium). Mice were anaesthesed through 5% isoflurane induction and maintained at 2% isoflurane in O_2 at a flow rate of 2 L/min. Mice were injected with Na[^{18}F]F at a target dose of 10 MBq in 200 µL saline solution through the lateral tail vein via a catheter. The mice were placed prone on the bed and respiration and temperature was monitored throughout the imaging experiment for animal welfare. The mice were positioned in the scanner with the abdominal aorta placed in the centre of the scanner using a scout CT scan. A 90 minute whole body, single bed position dynamic scan were acquired initially to determine tracer kinetics and scan time. Following the PET scan, a two bed position CT scan was performed for anatomical localisation and attenuation correction. For the longitudinal studies, a 30 minute static PET acquisition after a 50 minute tracer uptake window followed by two bed position 20 minute CT scan was performed.

2.3.4 PET reconstruction

PET/CT images were reconstructed on both the Albira reconstruction module and using the STIR library. Two bed CT images were reconstructed using high resolution filtered back projection algorithm (image voxel size 0.25 x 0.25 x 0.25 mm). PET images were reconstructed using a 3D Maximum-Likelihood Expectation-Maximization (MLEM) algorithm with 20 iterations and corrected for attenuation, scatter, random and decay events on both Albira reconstruction module and STIR library (Standard university of Leeds protocol). Images were further processed using Kernalized Expectation Maximum (KEM) and Hybrid KEM (HKEM) algorithms as described previously (221,222). Images reconstructed at iteration 8 subiteration 16 were used for analysis as noise increases at this point.

Generation of SUVmean, SUVmax and TBRmax was achieved in AMIDE (version 1.0.4) using a fixed dimension elliptic cylinder region of interest (ROI) . The aortic ROI was constructed, using CT for anatomical location, between the kidneys and anterior to the anterior border of the vertebrae. ROIs were drawn on 60 minute timeframe. The size of the ROIs were based off the aortic size as determined from USS and CTA scans.

2.3.5 *Ex vivo* gamma counting

After the conclusion of PET/CT imaging experiment, uptake of Na[^{18}F]F in murine tissue was measured using the HIDEX automatic gamma counter. Mice were recovered post PET/CT imaging experiment and humanely culled by cervical dislocation under Schedule 1 of Home Office Animals Scientific Procedures Act 1986. The following samples were collected to measure the distribution of Na[^{18}F]F in the AAA models; abdominal aorta, thoracic aorta, heart, lung, spine, blood and plasma. The tissue was placed in pre-weighed vials and measured for radioactivity and sample weight in the HIDEX. The measured radioactivity, in counts per minute, was corrected for background and decay before converting into MBq through the acquisition of a standard curve (Figure 3). The counts and mass of each sample were used to then calculate the percentage injected dose per gram (% ID/g).

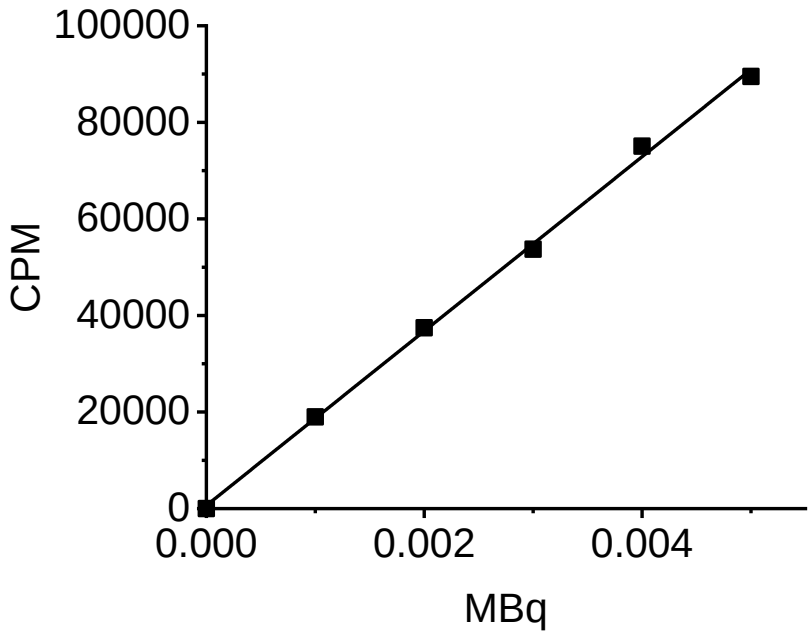

Figure 3: Standard curve used for converting gamma counting samples from CPM to MBq (r = 0.99, COD = 0.99).

2.4 Von Kossa histology

Microcalcification detection in paraffin embedded aortic samples using a Von Kossa stain kit (Abcam, ab150687) was performed at St James Hospital. In brief, paraffin sections were deparaffinised and then exposed in silver nitrate solution (5%) for 30 minutes under ultraviolet light. The sections were rinsed before

incubation in sodium thiosulfate solution (5%) for 2 minutes. The sections were further rinsed and then incubated in Nuclear Fast Red solution for 5 minutes. Images were collected using the AX10 bright field microscope (Zeiss). Images were taken at 20x and 40x magnification and analysed in ImageJ (version 2.3) to calculate the percentage area of Von Kossa positive staining.

2.5 Immunofluorescence histology

Upregulation or downregulation of calcification markers in the abdominal aorta was assessed using the mTmG lineage tracing murine line. Aortic tissue and sections were prepared by Dr Lucinda Craggs. After excision, the aorta was embedded in OCT through rapid freezing in an isopropanol and dry ice slurry. Once embedded, sections (10 µm thickness) of abdominal aorta were cut on a cryostat. Slides were removed from the -80 °C freezer and allowed to thaw to room temperature. Sections were washed with PBS to remove OCT residue, permeabilised for 30 minutes in PBS containing 0.3% Triton X-100, blocked for 1 hour in PBS containing 0.05% Triton X-100 and 10% novel horse serum. The slides were incubated for one hour at room temperature with antibodies specific for BMP-2 and OPG. Antibodies were validated in control tissue (bone marrow and smooth muscle cells) before staining on AAA sections (Figure 4). Sections were washed for 15 minutes using PBS containing 0.05% Triton X-100 before incubating with appropriate secondary antibodies for one hour. After the sections were washed for 15 minutes using PBS containing 0.05% Triton X-100, slides were mounted using Prolong Gold Antifade Reagent with DAPI . Sections were imaged on the LSM880 inverted confocal (Zeiss). Laser setting and channels were set using a no primary and no secondary antibody control and no primary control slide (Figure 4) to remove background signal. A tile scan at 20 x magnification and a z-stack covering 10 µM (10 slices at 1 µM thickness) ROI at 40 x magnification was taken for analysis. All analysis was completed in ImageJ (version 2.3). Each z-stack slice was counted for cells expressing DAPI, GFP, mTom, BMP2 and OPG. GFP expressing cells expressing BMP2 OR OPG were quantified and mTom expressing cells expressing BMP2 OR OPG.

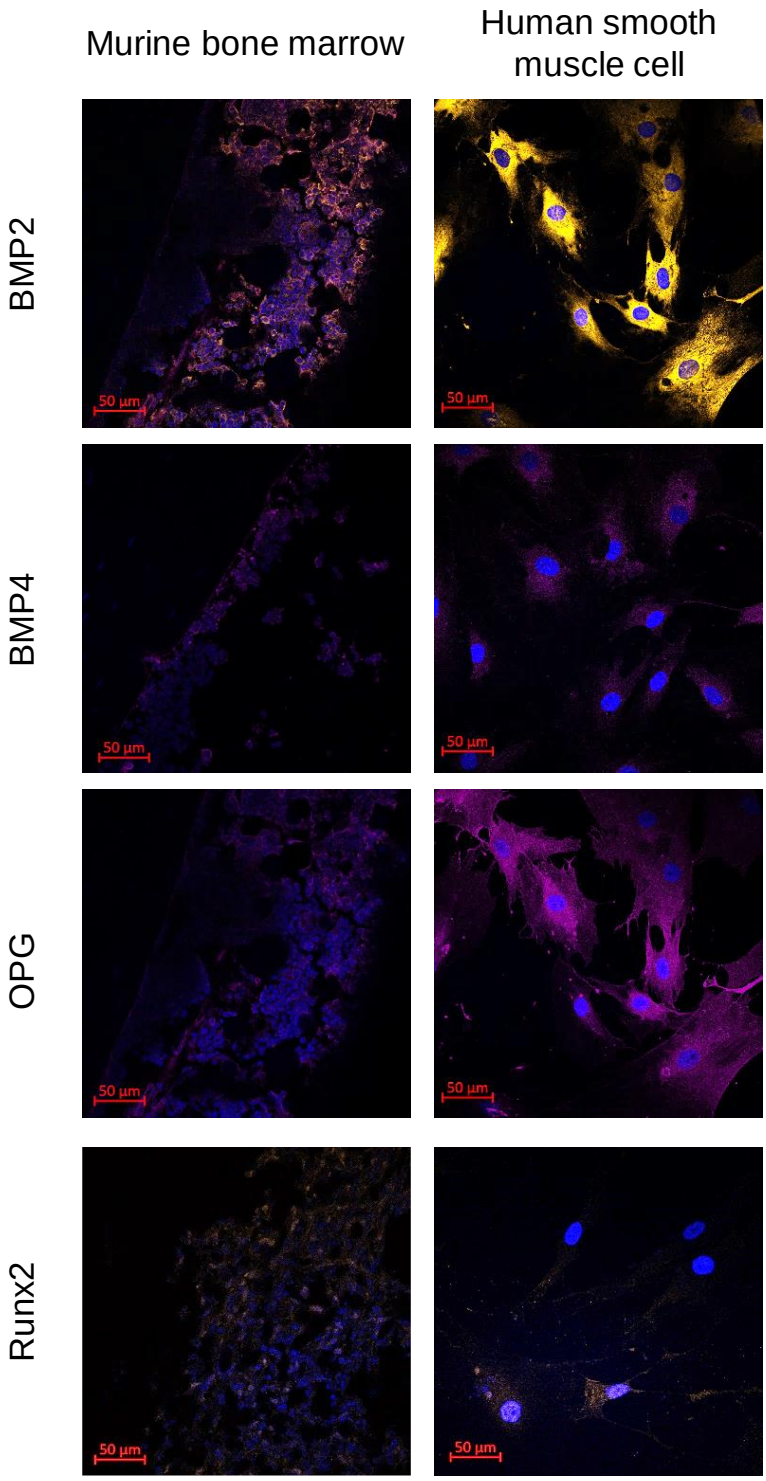

Figure 4: Validation of osteogenic calcification antibodies used in immunofluorescence confocal studies. BMP2 (1:100), BMP4 (1:100), OPG (1:100), Runx2 (1:200). Bone marrow samples kindly donated by Miss Lauren Eades.

2.6 Cell culture

All experiments in involving culturing of cells was performed in a Class II Biological Safety cabinet in a designated laboratory. Cells were cultured and maintained in a humidified incubator (5% CO_2, 37 °C). Fresh media was applied every two days and detached using Trypsin-EDTA. Cells were plated using Trypan blue stain and counted in duplicate using a haemocytometer.

2.6.1 Smooth muscle cell calcification

Saphenous vein smooth muscle cells (SVSMC) were plated in to 6 well plates at 1 x 10^4 cell/mL in DMEM GLUTAMAX + supplemented with 10% FBS and 1% penicillin/streptomycin and grown to confluency. The media was replaced with calcification media, prepared by adding 1 mmol/L $CaCl_2$, 2.14 mmol/L Na_2HPO_4 and 1.36 mmol/L NaH_2PO_4 into DMEM GLUTAMAX+ supplemented with 10% FBS and 1% penicillin/streptomycin and incubated for 7 days (223). After 24 and 72 hours the cells were harvested for RNA and media was collected for ELISA.

2.6.2 PDGF-BB assay

SVSMC were stimulated with PDGF-BB to study the role PDGF-BB plays in promoting VSMC calcification. SVSMC were plated in to 6 well plates at 1 x 10^4 cell/mL in DMEM GLUTAMAX+ supplemented with 10% FBS and 1% penicillin/streptomycin and grown to confluency. The media was replaced with serum free DMEM GLUTAMAX+ supplemented with 1% penicillin/streptomycin after washing the cells with PBS. After 3 days, cells were stimulated with either vehicle, 10 ng/mL PDGF-BB, 100 ng/mL or 10 ng/mL PDGF-BB and Calcification media as described in section 2.6.1. After 7 days, cells were harvested for RT-PCR and media was collected for ELISA to measure changes in calcification protein levels.

2.7 RNA isolation

RNA was isolated from confluent 6 well plates in a designated RNA preparation area using an RNA isolation kit (RNeasy mini kit Qiagen (74104)). The area and all consumables (pipettes, sterile filter tips) were first cleaned with 70% ethanol and followed by RNAase away surface decontaminant. Media was first removed and placed into 2 mL Eppendorf tubes. The wells were washed with sterile PBS before adding 350 µL Buffer RLT. The samples were vortex for a minute before

transferring to a gDNA eliminator column. The sample was centrifuged (30 s, 8000g). The column was discarded and 350 µL of 70% ethanol was added. The sample was mixed and placed into a RNeasy spin column. The sample was centrifuged (15 s, 8000 g) and the flow though was discarded. 700 µL Buffer RW1 was then added to the RNeasy spin column which was further centrifuged (15 s, 8000 g). The flow through was discarded and 500 µL of Buffer RPE was added to RNeasy column. The column was centrifuged (15 s, 8000g) and the flow through was discarded. A further 500 µL of Buffer RPE was added to RNeasy column and centrifuged (120 s, 8000 g). The column was then placed into a new collection tube and centrifuged at full speed (60 s). The RNA was eluted in 30 µL of RNAse-free water. RNA was quantified using the Nanodrop (ThermoScientific). RNA was stored at -80 °C until RT-PCR was carried out.

2.8 RT-PCR

All steps were performed by Dr Karen Hemmings.

2.8.1 Reverse transcription

Complementary DNA (cDNA) was produced using the High Capacity cDNA Reverse transcription kit (Thermofisher) by mixing RNA sample (10 µL), as prepared in Section 2.8, with a master mix including 10 X RT buffer (2 µL), 10 X Random Primers (2 µL), 25X dNTP Mix (0.8 µL), Multiscribe Reverse Transcriptase (1 µL) and Nuclease-free water (4 µL). The samples were centrifuged and placed on a thermal cycler using a four step heating protocol; (1) 25 for 10 minutes, (2) 37 for 120 minutes, (3) 85 for 5 minutes, (4) 4 until samples removed from thermal cycler. -RT samples were prepared by adding Nuclease free water (1 µL) instead of Multiscribe Reverse Transcriptase to check for contamination.

2.8.2 Quantitative reverse transcription polymerase chain reaction (qRT-PCR)

qRT-PCR was carried out on the Lightcycler 480 (Roche) using SYBR Green primers (Table 8) (Bio-Rad). Each well contained a mix of iTaq Mastermix (5 µL), nuclease free water (3.5 µL), primer of interest (0.5 µL) and cDNA (1 µL) generated in Section 2.9.1. The plate was spun briefly to ensure reagents are mixed and collected to the bottom of the well. qRT-PCR reactions were run using

the following protocol for 40 cycles: i) 95 C for 30secs ii) 60 C for 1 minute. Using the $2^{-\Delta CT}$, the abundance of target gene of interest relative to housekeeper (GAPDH) was calculated. Each experimental plate contained a control sample where Nuclease-Free water (1 µL) was added in place of cDNA. A melt curve at the end of the qRT-PCR reaction was conducted to check the melt profile of the primers used.

2.9 ELISA

ELISA was conducted to study changes in BMP2 and OPN expression in media from experiments described in Section 2.6. Media was collected from cell culture plates during RNA extraction. Media was placed into centrifuge tubes and centrifuged (10 minutes, 1500 RPM, 4°C). The supernatant was aliquoted and placed in a -80 °C freezer until use. Assay diluent (100 µL) was added into each well, along with either sample, standard or control (50 µL). The plate was sealed and placed on a horizontal orbital shaker (500 RPM) for 2 hours. The liquid was aspirated from each well before repeat washing of the plate. The conjugate of interest (BMP2 or OPN, 200 µL) was added to each well and plates were laid on a horizontal orbital shaker (500 RPM) for 2 hours. The liquid was aspirated from each well before repeat washing of the plate. After the final wash, substrate solution (200 µL) was added to each well. Plates were then covered and incubated at room temperature for 30 minutes. Before imaging on an optical reader, stop solution (50 µL) was added to each well. Readings were taken at 450 and 550 nm.

2.10 Statistics

All statistical analysis was conducted using OriginPro (2020). Unless stated otherwise, graphs presented in this thesis will display the mean and standard error. All data sets were tested for normal distribution. For the data that is normally distributed, comparison between two sets of data was analysed using a student t-test. Data that failed normal distribution analysis were analysed using a Wilcoxon rank sum test. Statistical significance was assumed with a $P<0.05$ with a $P>0.05$ denoted no statistical significance (indicated by NS on graphs). OriginPro (2020) was used for generation of all graphs presented in this thesis.

Chapter 3
Results

3.1 Baseline Na[^{18}F]F scans

PET/CT scans in wild type mice were conducted to study the pharmacokinetics of Na[^{18}F]F without the presence of discrete vascular pathology. This experiment was conducted to show competency in performing Na[^{18}F]F PET/CT, in addition to demonstrating Na[18F]F uptake on the Albira Si µPET/SPECT/CT and in novel AAA murine models, ahead of future experiments.

Figure 5 demonstrates the uptake of Na[^{18}F]F one hour post injection, with uptake seen predominantly in bone and bladder. Figure 6 details the time course of Na[^{18}F]F distribution. Early time frames (6 secs) demonstrate successful injection of Na[^{18}F]F through the vena cava and into the heart (14 secs). Na[^{18}F]F is then distributed through the body via the kidneys (60-300 secs) before accumulating in the bone (3600-5400 secs).

To understand the pharmacokinetics of Na[^{18}F]F uptake in calcified regions (i.e. vertebrae) and in the aorta, the accumulation of Na[^{18}F]F was traced over the imaging time course to generate time activity curves (Figure 7). Rapid accumulation of Na[^{18}F]F is seen in the vertebrae. The high peak seen in the early time frames in the abdominal aorta (AA) region demonstrates the first pass of Na[^{18}F]F before accumulation in regions of microcalcification (Figure 7). Figure 7 also demonstrates the potential challenge of quantifying Na[^{18}F]F uptake in the preclinical AAA models due to residual Na[^{18}F]F activity in the blood pool of healthy aorta.

Figure 8 shows the quantification of SUV_{mean} (Figure 8a), SUV_{max} (Figure 8b) and TBR_{max} (Figure 8c) for vertebrae and abdominal aorta (AA) regions using ROIs drawn as described in Section 2.3.4 at 3600 secs, with the mean and SE tabulated in Table 9. Finally biodistribution analysis confirmed greatest uptake of Na[^{18}F]F in Spine (%ID/g = 7.1 ± 1.3) and the baseline %ID/g in the abdominal aorta was 0.27 ± 0.11 (Figure 8d). Low %ID/g in control tissue (heart, lung, liver), along with data shown in Figure 8a, b and c, demonstrate the specificity of Na[^{18}F]F in binding to regions containing microcalcification. In addition, low% ID/g in plasma (0.31 ± 0.14) suggests clearance of radiotracer from the blood for accurate interpretation of Na[^{18}F]F accumulation. Sections of AA were cut and

stained using Von Kossa kit to demonstrate the lack of microcalcification in the aortic wall (Figure 9).

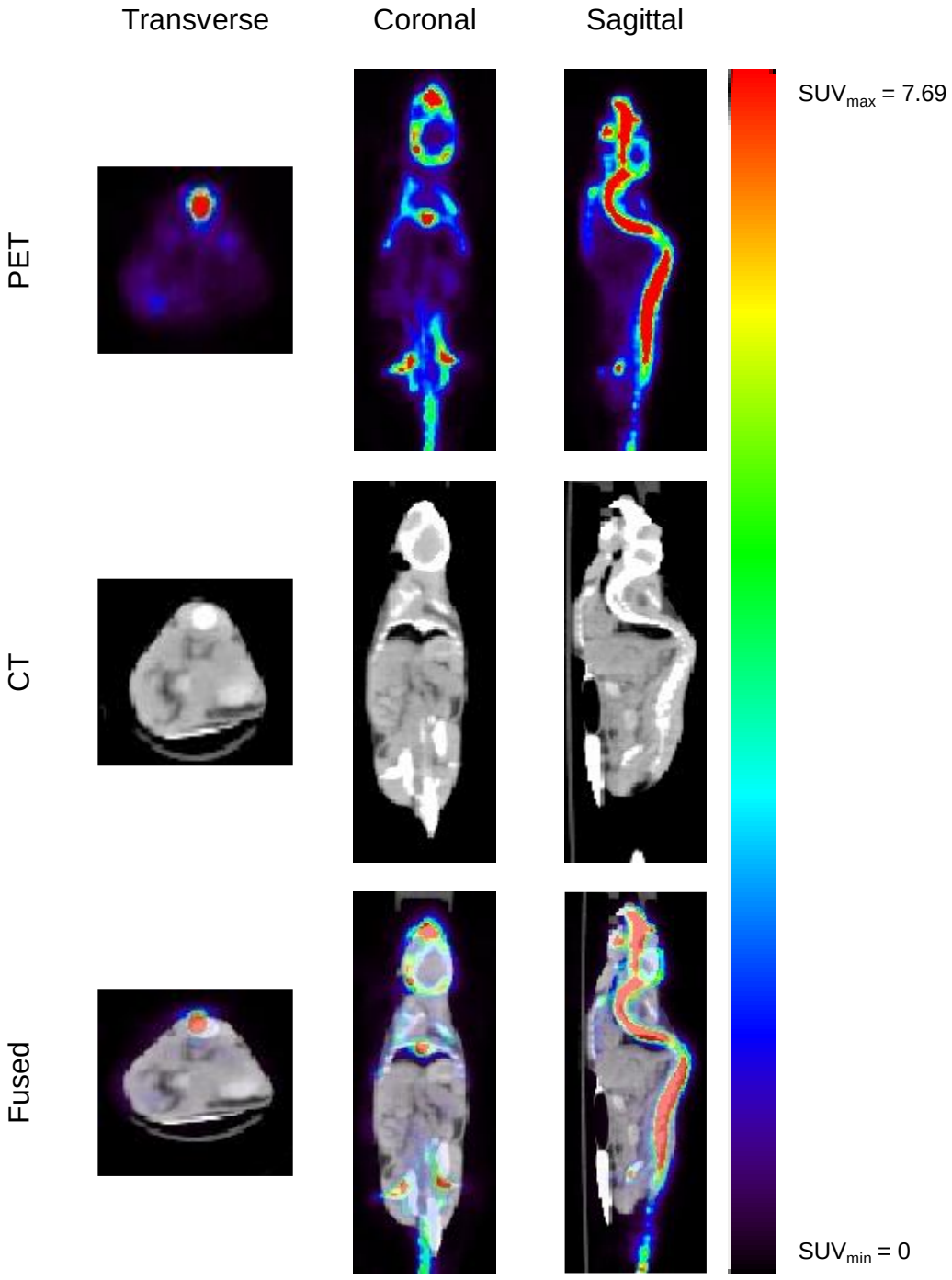

Figure 5: Representative PET/CT image of baseline model injected with Na[^{18}F]F IV. Images shown 1 hour post injection with Na[^{18}F]F localising in the skull, vertebrae, rib cage and bladder. n=4.

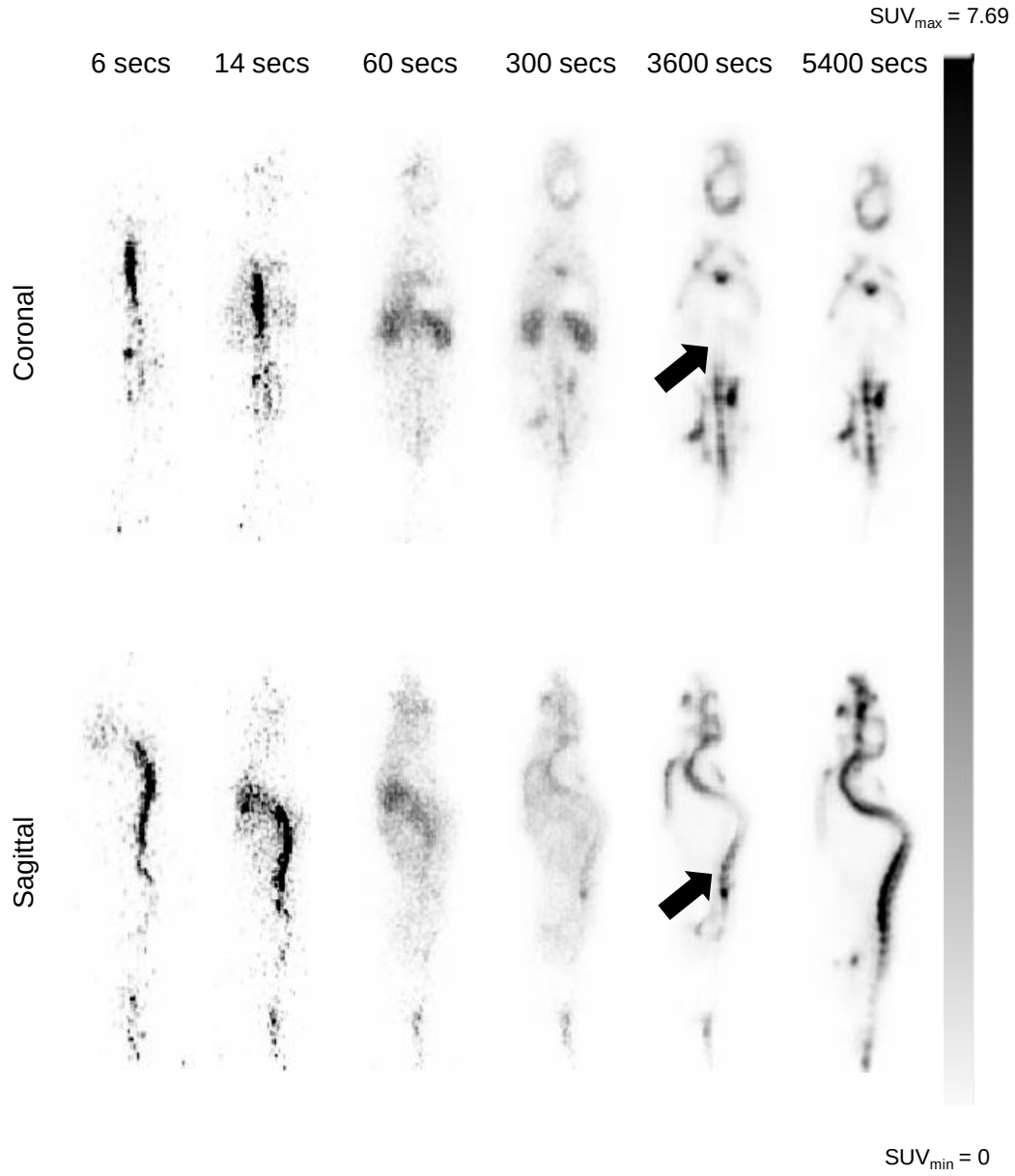

Figure 6: Na[^{18}F]F biodistribution in baseline model through time course of a PET scan. Uptake at 6 secs shows Na[^{18}F]F uptake through the vena cava traveling to the heart (12 secs). Na[^{18}F]F is distributed through the body travelling through the kidneys (300 secs) and accumulating in bone regions (3600-5400 secs). Arrow indicates uptake in abdominal aorta with partial volume effects from the bone. Image reconstructed using Bruker module at 0.5 mm voxel size, 20 iterations. n=4.

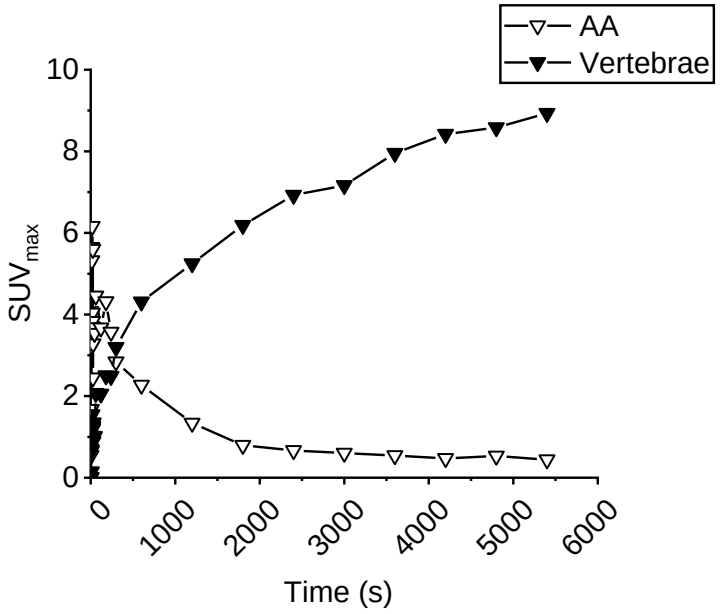

Figure 7: Dynamic distribution of Na[^{18}F]F in baseline models. Accumulation of Na[^{18}F]F is seen in the bone with an increase in scan time. In the early time frames of the scan (6-14 secs), the first pass of Na[^{18}F]F in the abdominal aorta (AA) is seen before wash out and accumulation.

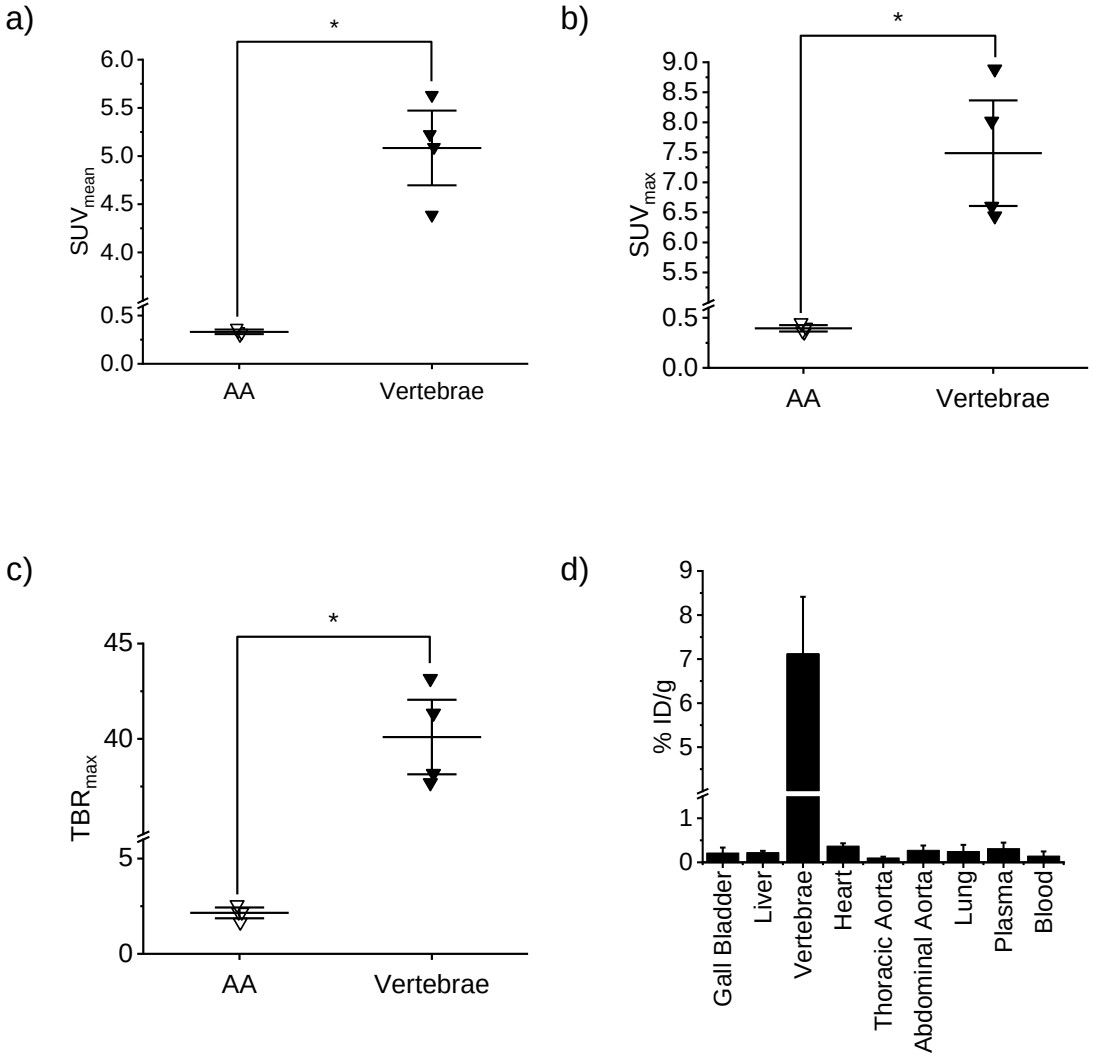

Figure 8: Baseline quantification of PET/CT images for (a) SUV_{mean}, (b) SUV_{max} and (c) TBR_{max} and (d) biodistribution in murine tissue including the abdominal aorta and bone. n=4, mean and standard error shown.

Table 9: Quantification of vertebrae and AA in baseline model.

Metric	Vertebrae	AA	P value
SUV_{mean}	5.1 ± 0.26	0.33 ± 0.016	0.00039
SUV_{max}	7.5 ± 0.59	0.40 ± 0.021	0.0013
TBR_{max}	40 ± 1.3	2.1 ± 0.19	0.00011

Magnification Baseline AA

40 x

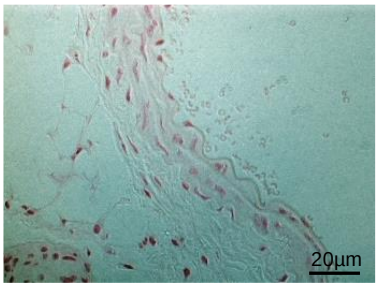

Figure 9: Representative slice from Von kossa stain of baseline aortic tissue.

The results from baseline scans confirmed the expected pharmacokinetics of Na[^{18}F]F in wild type mice and indicated that uptake of Na[^{18}F]F in bone containing regions occurs 1 hour post injection. In addition, baseline quantification using image derived metrics (e.g. TBRmax) and% ID/g from biodistribution give an indication of abdominal aortic uptake without surgical or therapeutic intervention.

3.2 Na[^{18}F]F uptake in $CaCl_2$ murine model

To determine if detection of microcalcification using Na[^{18}F]F is plausible in a preclinical model and system, the $CaCl_2$ murine model was used as a positive control. As stated in section 1.5.2, the $CaCl_2$ model was developed due to the appearance of calcified lesions on the aortic wall in AAA subjects.

Ultrasound analysis did not show a statistical difference between aortic diameter in sham and $CaCl_2$ group (0.32 mm ± 0.033 vs 0.40 mm ± 0.021 respectively, p=0.08), although the trend towards a larger aortic size was seen in $CaCl_2$ group (Figure 10). 3D volumetric analysis was not completed due to the peri-vascular inflammation caused by the $CaCl_2$ cast an acoustic shadow which obscured portions of the aorta.

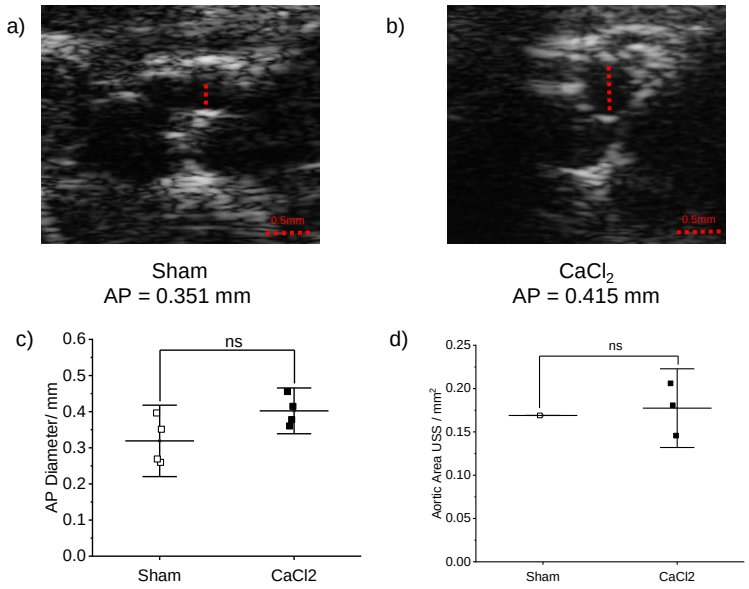

Figure 10: USS analysis of $CaCl_2$ AAA murine model. Representative EKV slice images showing little dilation of the aorta (a,b). Red dotted lines indicate AP diameter of sham and $CaCl_2$ aorta. No statistical difference was found between sham and $CaCl_2$ AAA model for either AP diameter (c) or aortic area (d). ns; not significant. n=4 sham, n=4 $CaCl_2$, mean and standard error shown.

Figures 11 and 12 respectively show representative PET/CT image slices of sham and $CaCl_2$ models from the study cohort. PET image data in Figure 13 indicate that Na[^{18}F]F followed the same pharmacokinetic profile in the $CaCl_2$ and sham models, similar to as described in section 3.1. However, there is Na[^{18}F]F accumulation in the AA, denoted by the black arrow. Figures 14 and 15 demonstrate a direct comparison representative PET/CT slices of sham and $CaCl_2$ models. Uptake in the abdominal aorta is seen in 2/3 of the models with peri-adventitial application of $CaCl_2$ on the aorta that is visually distinguishable from sham equivalent models at 3600 seconds post injection, demonstrating some variability in this study cohort.

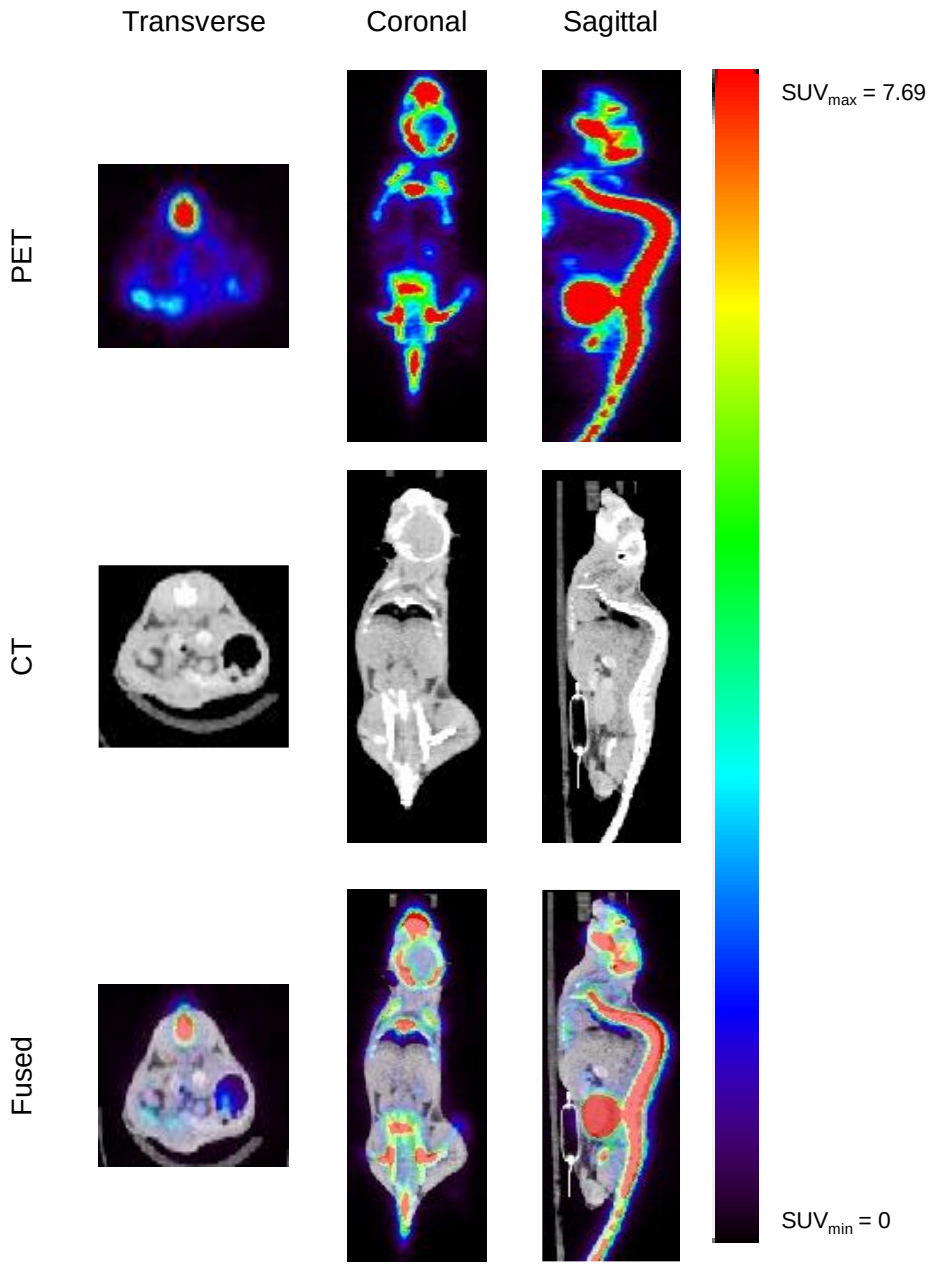

Figure 11: Representative PET/CT slices from sham model from $CaCl_2$ cohort. Slices shown 1 hour post Na[^{18}F]F injection. n=4.

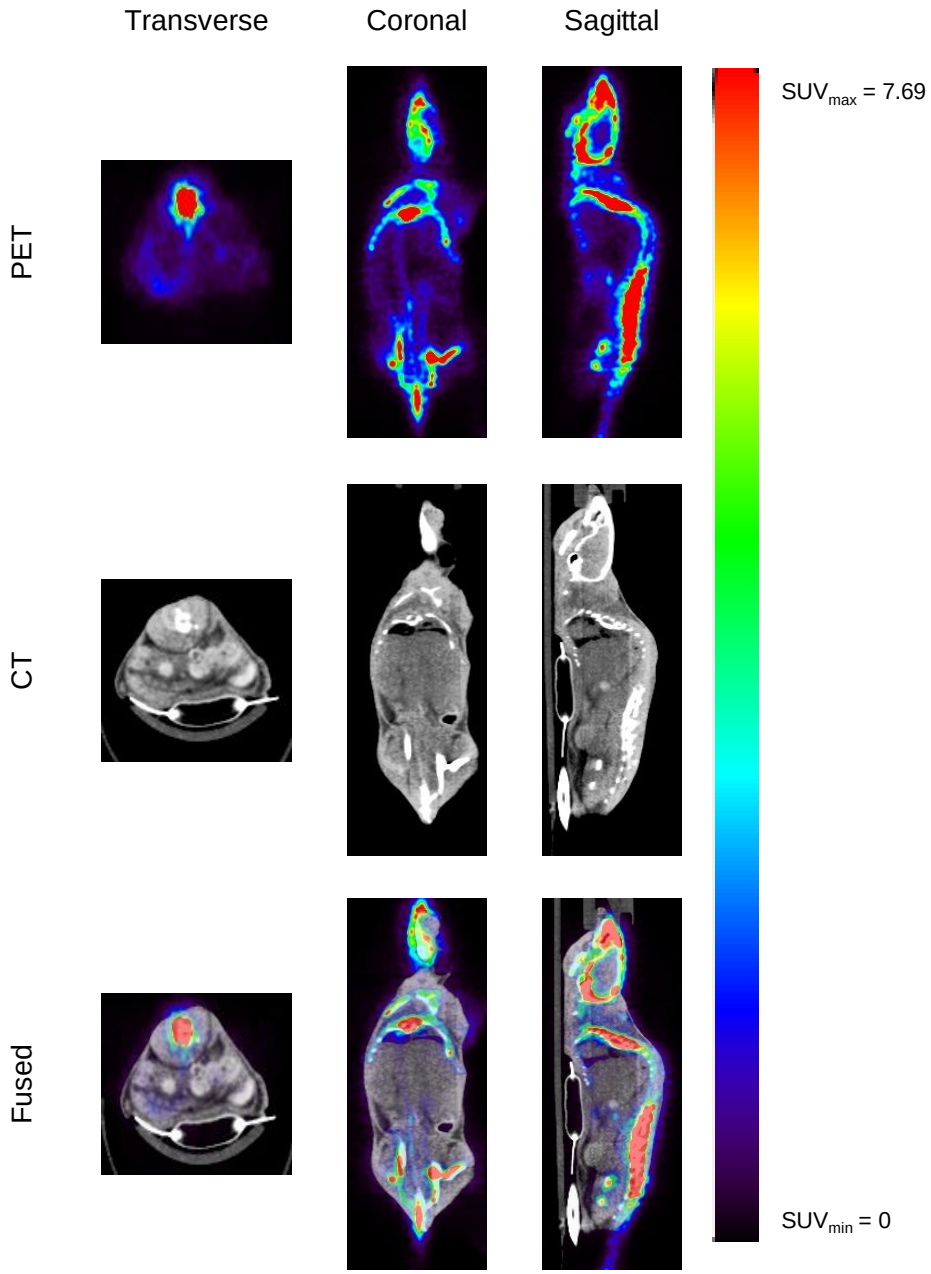

Figure 12: Representative PET/CT slices from $CaCl_2$ model from $CaCl_2$ cohort. Slices shown 1 hour post Na[^{18}F]F injection. n=3.

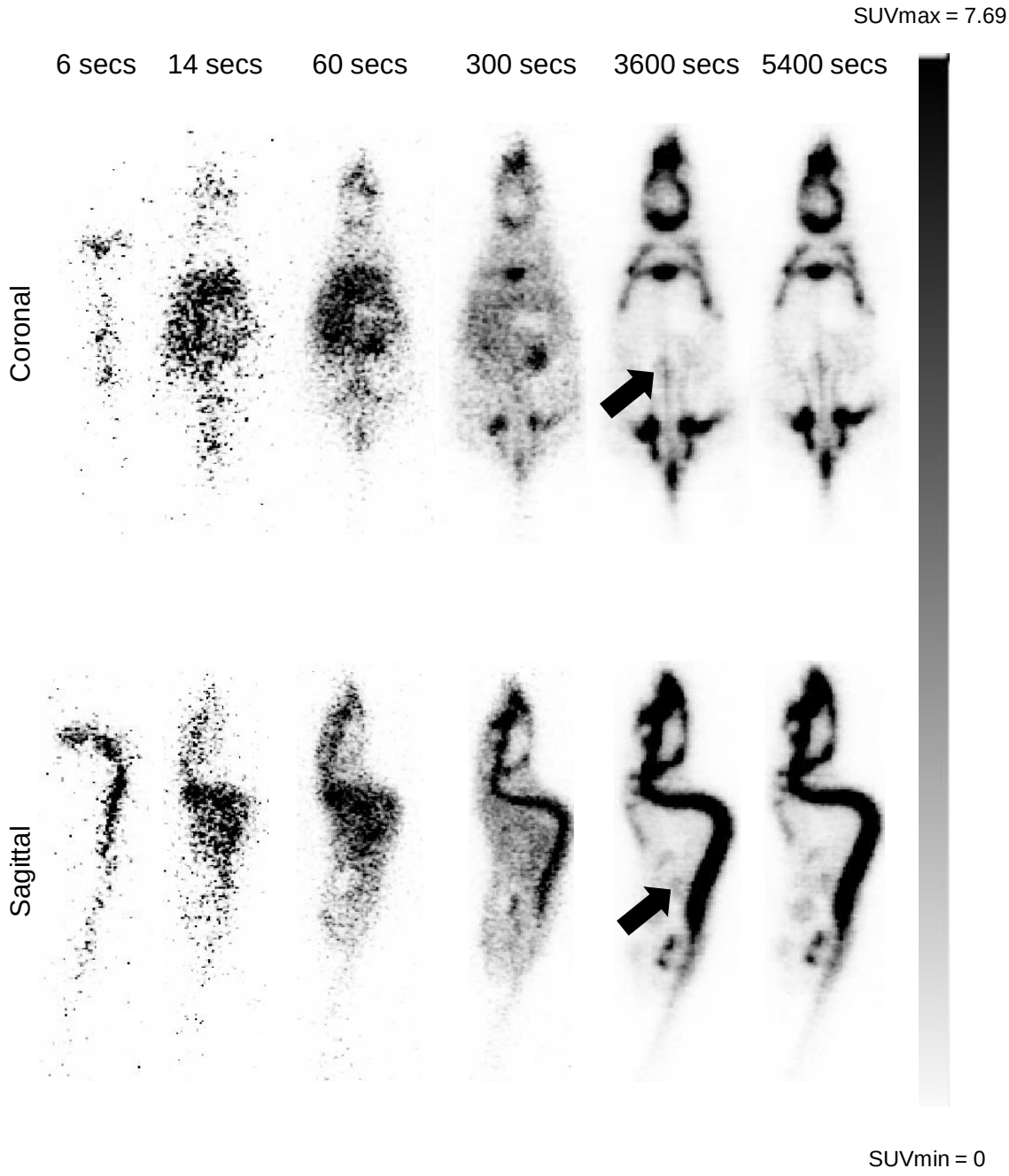

Figure 13: Coronal and sagittal representative PET images demonstrating pharmacokinetics of Na[^{18}F]F uptake in $CaCl_2$ model. Model shown is a peri-adventitial $CaCl_2$ treated model. Uptake at 6 secs shows Na[^{18}F]F uptake through the vena cava travelling to the heart (12 secs). Na[^{18}F]F is distributed through the body travelling through the kidneys (180 secs) and accumulating in bone regions (1200 and 3600 secs). Black arrow indicates uptake in AA with partial volume effects from the bone. Image reconstructed using Bruker module at 0.5 mm voxel size, 20 iterations. n=3

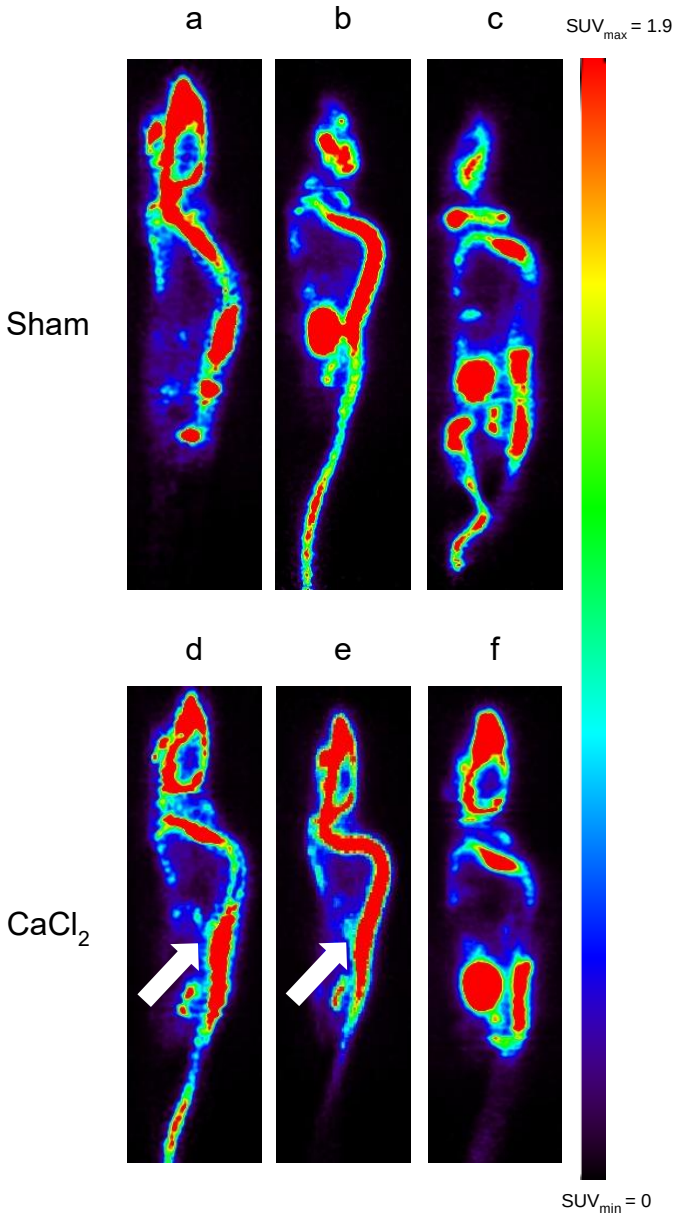

Figure 14: Uptake of Na[^{18}F]F in sham vs $CaCl_2$ model (sagittal plane shown). Uptake seen in the skeleton and on the abdominal aorta in the infrarenal region (indicated by white arrows). Each image label depicts an individual mouse.

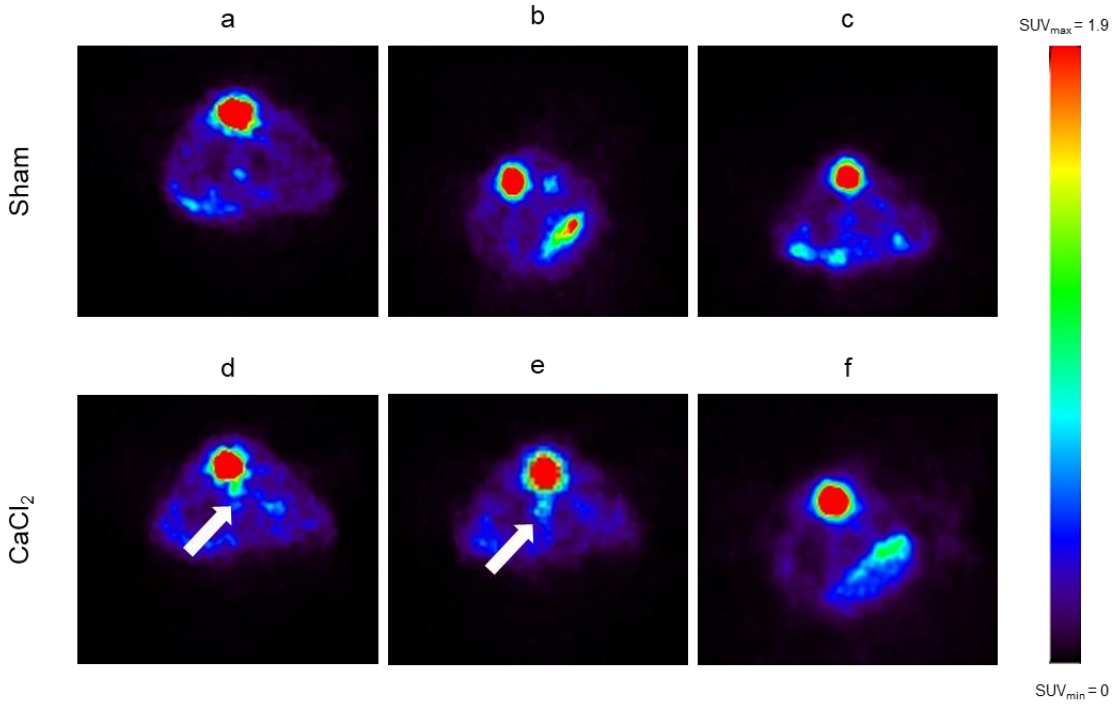

Figure 15: Uptake of Na[^{18}F]F in sham vs $CaCl_2$ model (transverse plane shown). Uptake seen in the skeleton and on the AA in the infrarenal region (indicated by white arrows). Each image label depicts an individual mouse.

Time activity curves for Na[^{18}F]F uptake in bone and AA in sham and $CaCl_2$ cohort (Figure 16) follow a similar trajectory as baseline models (Figure 7). Large accumulation is seen in the bone as time increases. A difference in intensity between sham and $CaCl_2$ for uptake in bone is due to injection quality (Figure 16a). In the AA, there is a higher uptake, and thus retention, of Na[^{18}F]F in $CaCl_2$ model, which could indicate the presence of microcalcifications.

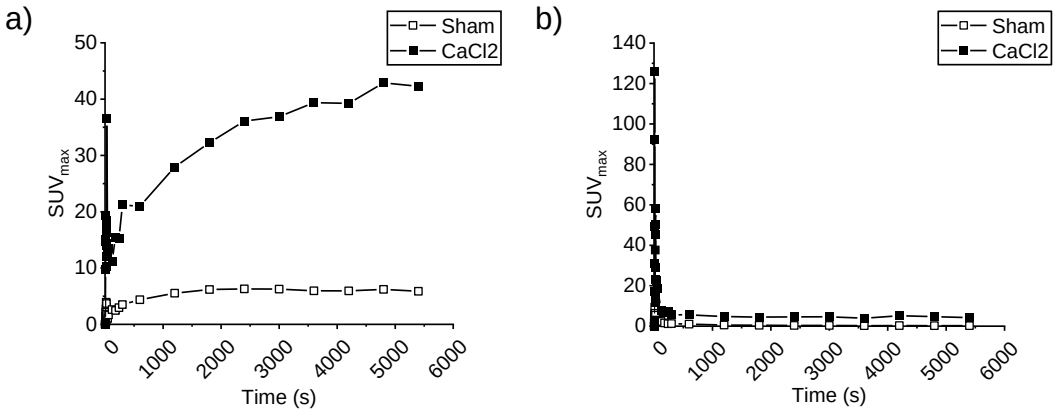

Figure 16: Time activity curves for [^{18}F]-NaF uptake in sham and $CaCl_2$ induced aneurysmal aortas demonstrating heterogeneity of AAA formation. (a) = Na[^{18}F]F uptake in the vertebrae. Accumulation of Na[^{18}F]F is seen in the vertebrae with an increase in scan time. (b) = Na[^{18}F]F uptake in the abdominal aorta. In the early time frames of the scan (6-14 secs), the first pass of Na[^{18}F]F in the abdominal aorta (AA) in both sham and $CaCl_2$ models. However, as scan time progresses retention of Na[^{18}F]F is seen in the $CaCl_2$ model compared to the sham model, indicating detection of microcalcification deposits.

Quantification of Na[^{18}F]F uptake from PET/CT images at 1 hour is shown in Table 10 and Figure 17. All metrics demonstrate a difference between sham and $CaCl_2$ models, with the greatest difference seen in quantifying using TBR_{max}, however Figure 17 demonstrates the large variability in SUV_{mean} and SUV_{max}. The difference between TBR_{max} and SUV_{max} measurements could be due to TBR_{max} incorporating SUV_{max} measured in the background and thus removing signal contamination that is seen in the other metrics. Large variability in SUV_{max} and SUV_{mean} could be a result of partial volume effects from the bone. This can be demonstrated in the line profiles of baseline, sham and $CaCl_2$ models (Figure 18).

Figure 18a shows representative PET/CT images and the position of the line profiles from which SUV_{max} values were recorded. The line profiles cross the bone of the spine and the adjacent AA. Figure 19 shows the zoomed in line profile around the bone and abdominal aorta. Both baseline (Figure 19a) and sham (Figure 19b) line profiles show a clear profile representing the bone, however in the $CaCl_2$ line profile (Figure 19c), a profile representing the abdominal aorta is masked by the profile from the bone. This signal masking is further highlighted in Figure 19 and is one of the challenges of preclinical AAA imaging. The close

anatomical location of AA and bone and the large Na[^{18}F]F signal from the bone prevent the regions from being clearly distinguished. Statistical significance was not found in any of the measured metrics, owing to small sample size (n=3).

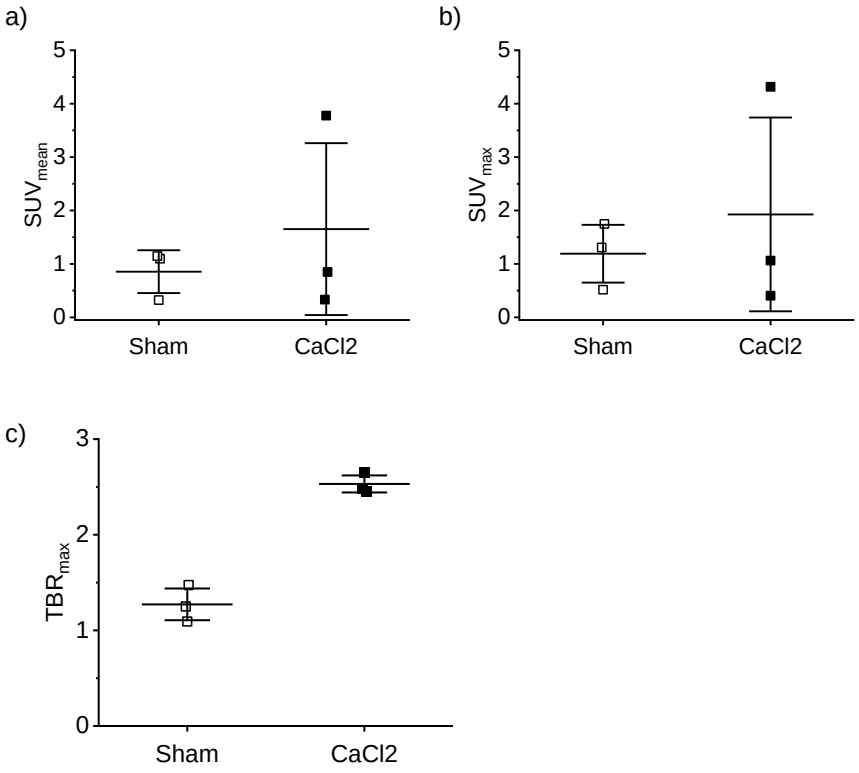

Figure 17: PET/CT image derived quantification of Na[^{18}F]F in the AA region of sham vs $CaCl_2$-treated mice. Data presented as (a) SUV_{mean} (b) SUV_{max} and (c) TBR_{max} from images at 1 hour post injection. n=4 sham, n=3 $CaCl_2$, mean and standard error shown.

Table 10: **PET/CT image derived quantification of Na[^{18}F]F in the AA region of sham vs $CaCl_2$ AAA models.**

Metric	Sham	$CaCl_2$
SUV_{mean}	0.86 ± 0.27	1.7 ± 1.1
SUV_{max}	1.2 ± 0.36	1.9 ± 1.2
TBR_{max}	1.3 ± 0.11	2.5 ± 0.059

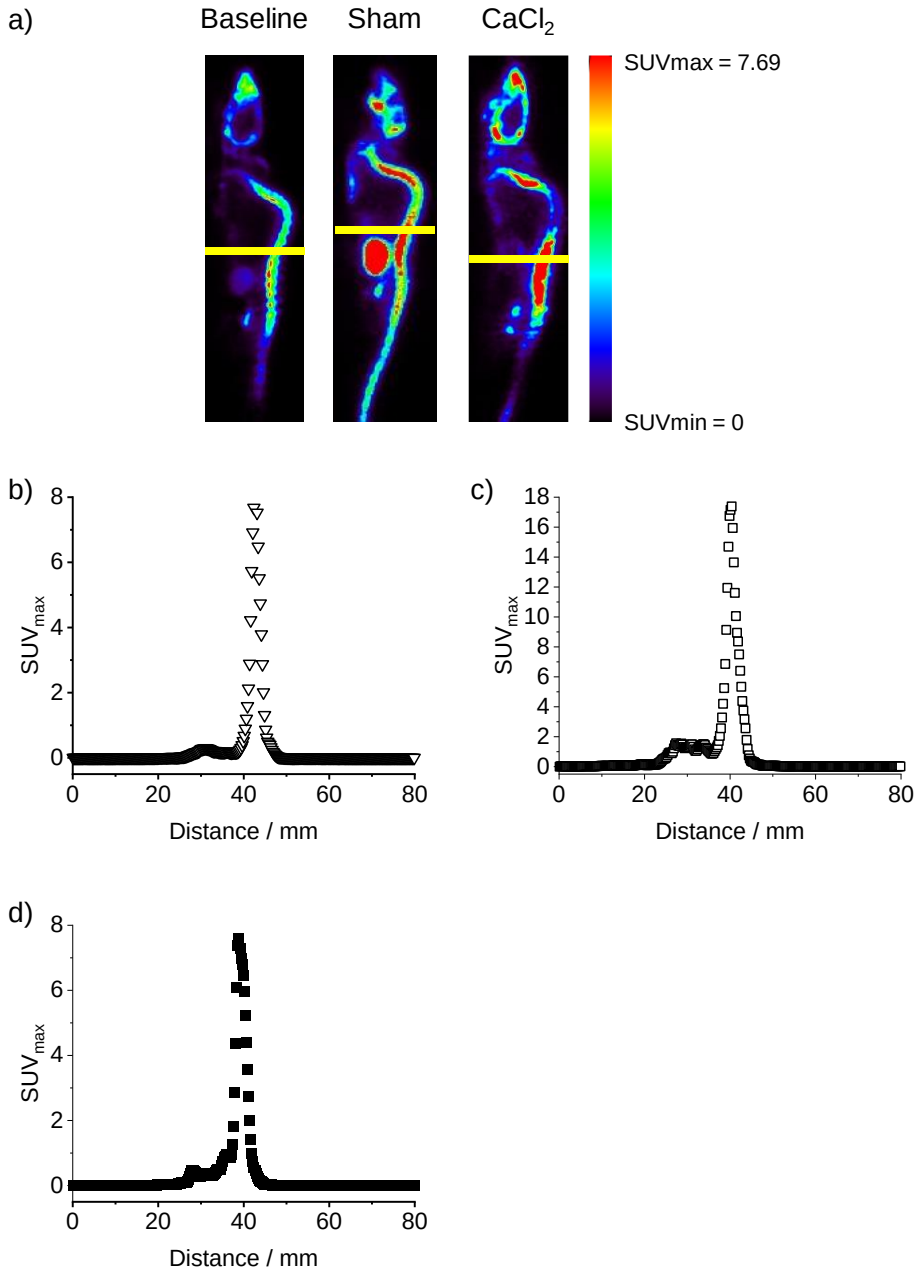

Figure 18: Sagittal PET/CT image slices and respective SUV_{max} line profiles. (a) representative sagittal slices from baseline, sham in $CaCl_2$ group and $CaCl_2$ models. A line profile taken through the AA and plotted for (b) baseline, (c) sham and (d) $CaCl_2$. Images at 1 hour post injection.

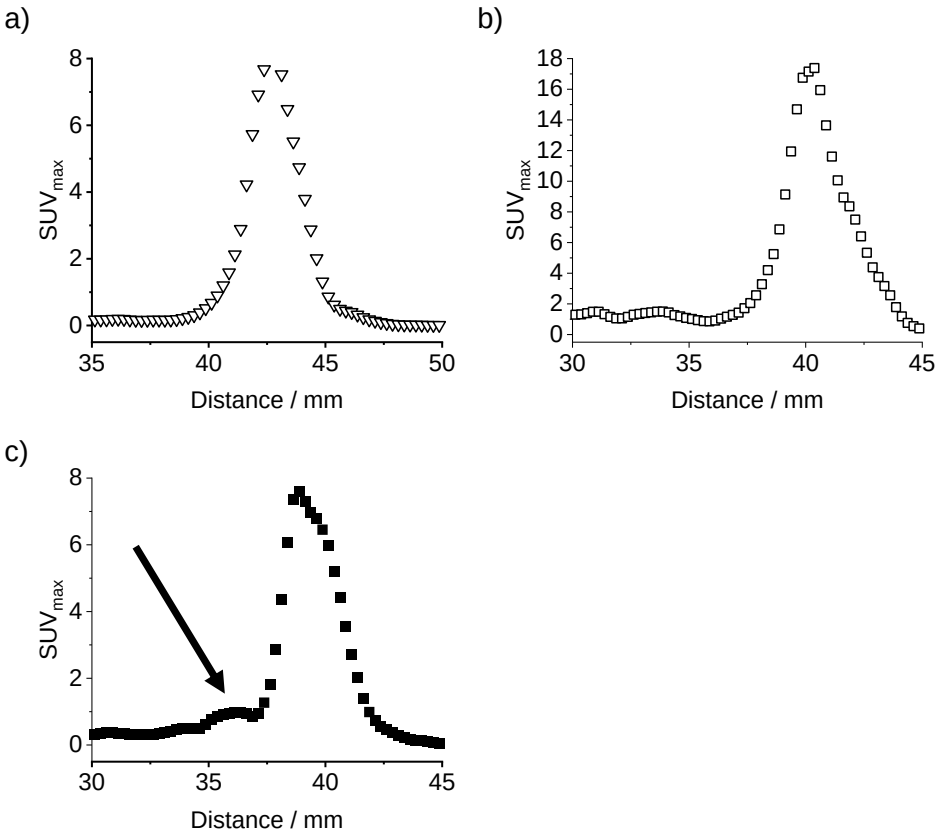

Figure 19: Line profiles show signal masking of AA by adjacent bone. (a) Baseline line profile follow a similar trajectory to (b) sham. Black arrow on (c) CaC_{l2} shows signal potentially masked by bone in AA region.

Gamma counts from harvested AA tissue (post PET/CT imaging) demonstrated an increased uptake of Na[^{18}F]F in $CaCl_2$ models compared to sham model (Sham% ID/g = 0.045 ± 0.082, $CaCl_2$% ID/g = 0.5 ± 0.29, $p < 0.05$) (Figure 20). Similar to results in section 1, Na[^{18}F]F accumulated in the bone (Sham% ID/g = 5.0 ± 1.1, $CaCl_2$% ID/g = 7.9± 1.9) and clearance from the plasma is also noted (Sham% ID/g = 0.26 ± 0.10, $CaCl_2$% ID/g = 0.055 ± 0.055). Finally, Von Kossa stain revealed the presence of microcalcifications in the aortic wall and on the surface of the aorta in $CaCl_2$ operated models (Figure 21).

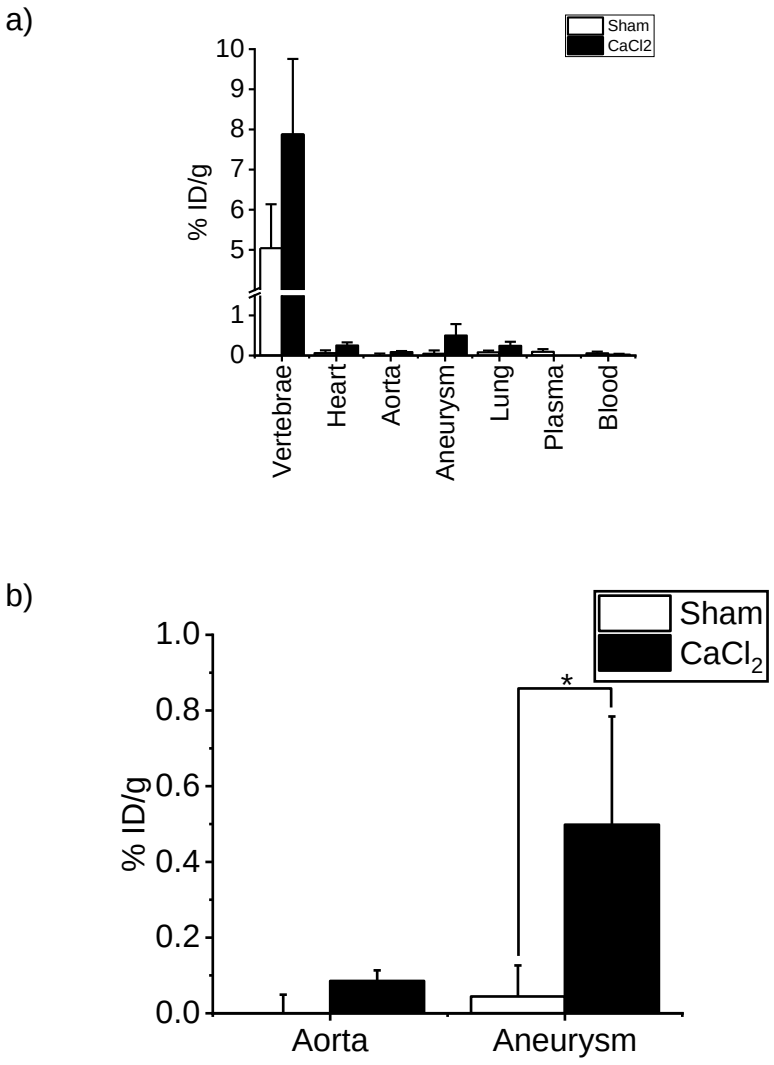

Figure 20: Gamma counting of harvested tissue from sham and $CaCl_2$-treated mice following PET/CT studies. (a) displays gamma counts from various tissues and fluids. (b) shows gamma counting of aorta and abdominal aneurysm tissue from sham and $CaCl_2$ model, with data demonstrating a significant increase in Na[^{18}F]F uptake in $CaCl_2$ mice ($p=0.05$). Data presented as mean and SEM (n=4 sham, n=3 $CaCl_2$). Mean and standard error shown.

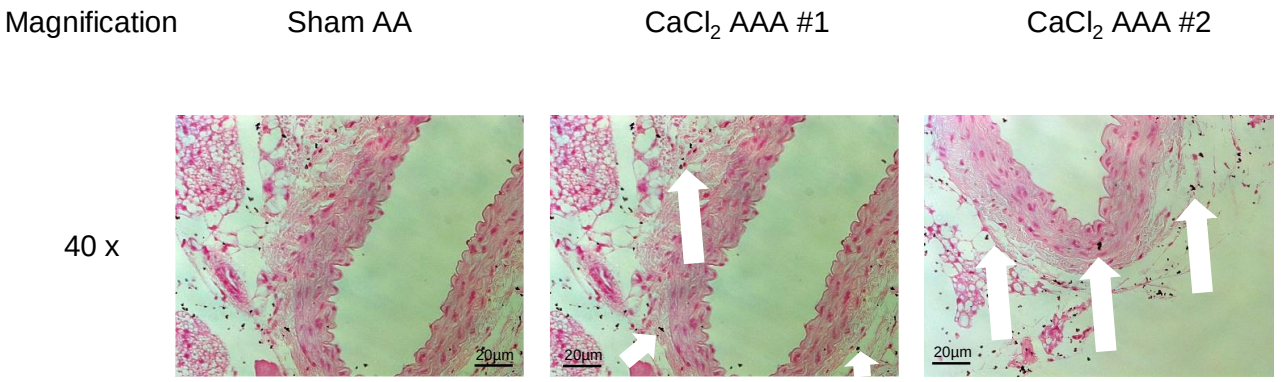

Figure 21: Sham and $CaCl_2$ AA sections stained with Von Kossa. White arrows indicate the presence of Von Kossa positive microcalcifications in the aortic wall.

The $CaCl_2$ model demonstrated that Na[^{18}F]F detection of microcalcifications in preclinical imaging is challenging. This is down to the anatomical location of bone in relation to the AA and Na[^{18}F]F uptake in the bone masks the AA. However, quantifying PET/CT images using TBR_{max} does suggest the removal of background signal could provide an accurate quantification of Na[^{18}F]F exhibiting microcalcification development. In addition, gamma counting of untreated aorta and AA tissue showed a significant difference in Na[^{18}F]F uptake between these tissues in $CaCl_2$-treated mice, but not in the sham group. As the $CaCl_2$ model of AAA produces variable results, with poor aneurysm generation in this study, an alternative model of AAA was investigated.

The PPE model was chosen as it represents the clinical scenario more accurately than the Ang-II model, which represents aortic dissection. As stated in Section 1.5.1, the PPE model generates infrarenal aneurysm induction, as seen in the clinical presentation of AAA, compared to suprarenal aneurysm induction as seen in Ang-II model.

3.3 Na[^{18}F]F uptake in PPE model of AAA

Due to the large variability in aneurysm induction using peri-adventitial $CaCl_2$, the PPE model was used. Our group has reported the PPE model and shown competence in consistent aneurysm induction (59).

Histological sections of AA taken from sham and PPE models (day 14 post intervention) stained with von Kossa demonstrated the appearance of microcalcifications in the aortic wall in PPE mice. No microcalcifications were detected in the sham controls. This was verified by quantification of the percentage area of von Kossa stain in the aortic wall, which demonstrated a significantly higher percentage area of PPE samples were positive for von Kossa (0.90±0.28%) compared to sham (0.039±0.033%).

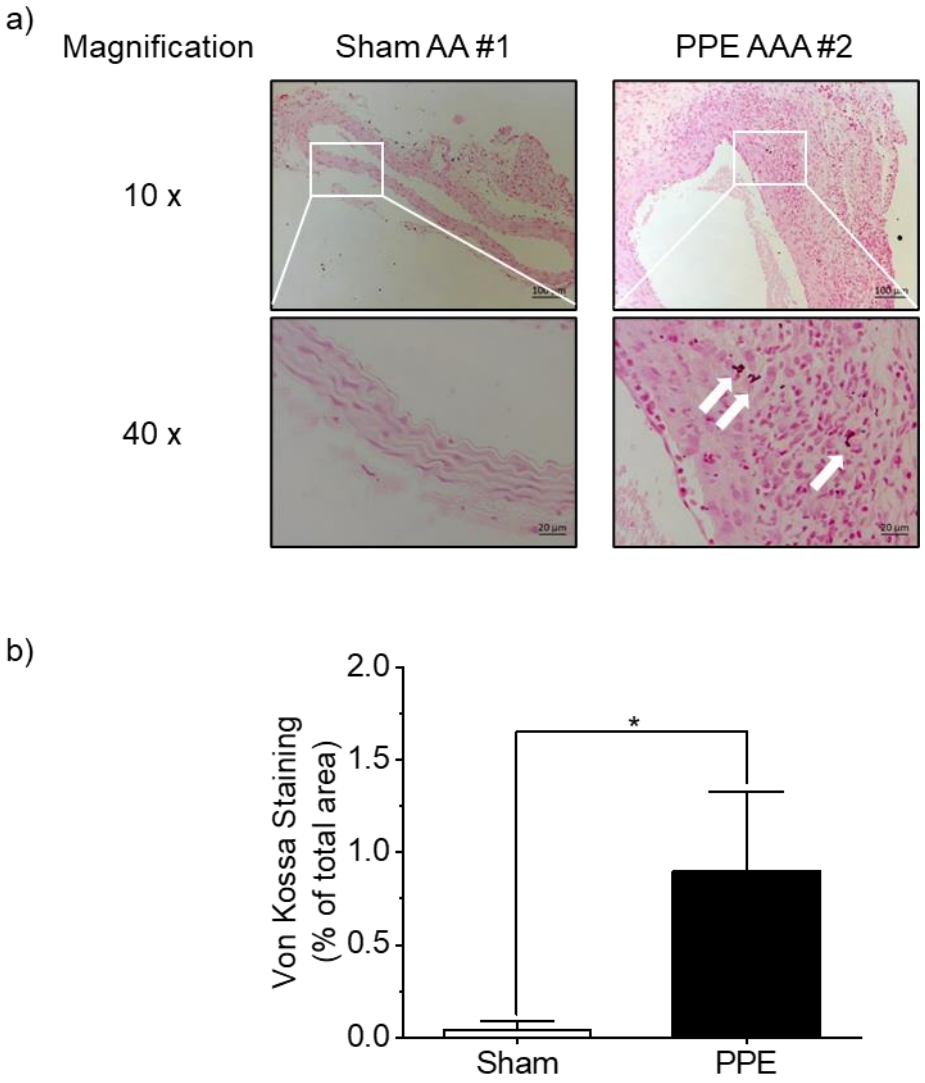

Figure 22: Von Kossa staining and staining quantification of AA tissue from sham and PPE-treated mice at day 14 post procedure. Staining is shown as 10x and 40x magnification (a). Von Kossa stain present in PPE AAA tissue sections, as highlighted by the white arrows. Quantification of microcalcification deposits demonstrate higher presence in PPE model compared to sham ($P<0.05$, n=5 sham, n=5 PPE). Mean and standard error shown.

USS analysis of sham and PPE induced models (day 14 post intervention) showed positive aneurysm induction in the PPE model (Figure 23). 3D volumetric analysis of the aorta further confirmed aneurysm induction through an increase in aortic volume. Quantification of aortic diameter and aortic volume demonstrated a significant difference between sham and PPE models, with both measures markedly increased in PPE mice (Figure 23 and Table 11).

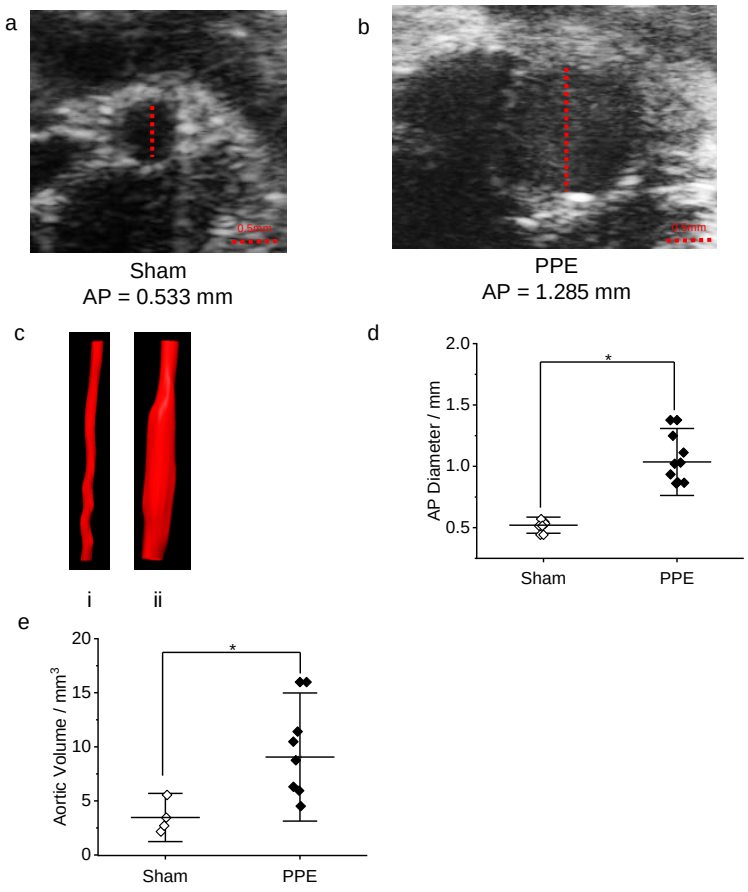

Figure 23: USS analysis confirms dilation of aorta in PPE aneurysm model. (a,b) representative EKV slice images showing increase in anterior-posterior (AP) diameter in PPE compared to sham. (c) 3D reconstructed aortic volume in sham (i) and PPE (ii) models. Statistical analysis of infra renal aorta shows significant increase in AP diameter and aortic volume (d, e) (<0.05). Mean and standard error shown.

Table 11: Quantification of aortic diameter and aortic volume in day 14 sham and PPE using USS

Metric	Sham	PPE	P value
Aortic Diameter / mm	0.52 ± 0.018	1.0 ± 0.061	0.000014
Aortic volume / mm^3	3.5 ± 0.74	9.1 ± 1.5	0.025

Ex vivo gamma counting of tissue from sham and PPE mice (day 14 post intervention) followed a similar pattern as described in $CaCl_2$ and baseline models. High Na[^{18}F]F uptake was seen in the bone of both sham and PPE models (%ID/g 6.0±4.0 vs 17.0±3.0, respectively). Low Na[^{18}F]F uptake was seen

in tissue that does not typically show calcification (lung and heart), as well as low Na[^{18}F]F in plasma (~0.35% of total injected radioactivity), showing Na[^{18}F]F clearance from the blood, which demonstrates specificity of Na[^{18}F]F for calcified areas (Figure 24a). A significant difference between Na[^{18}F]F uptake in AA tissue was seen in PPE model (ID/g 0.13±0.015) compared to sham (ID/g 0.00015±0.015) (Figure 24b). This is in line with the appearance of microcalcification deposits detected in the von Kossa staining of PPE tissue presented in Figure 22. %ID/g in AA tissue positively correlated with both aortic diameter (r = 0.80; COD 0.65) and aortic volume (r=0.59, COD = 0.35) (Figure 25) suggesting high Na[^{18}F]F uptake could be an indicator of aortic expansion.

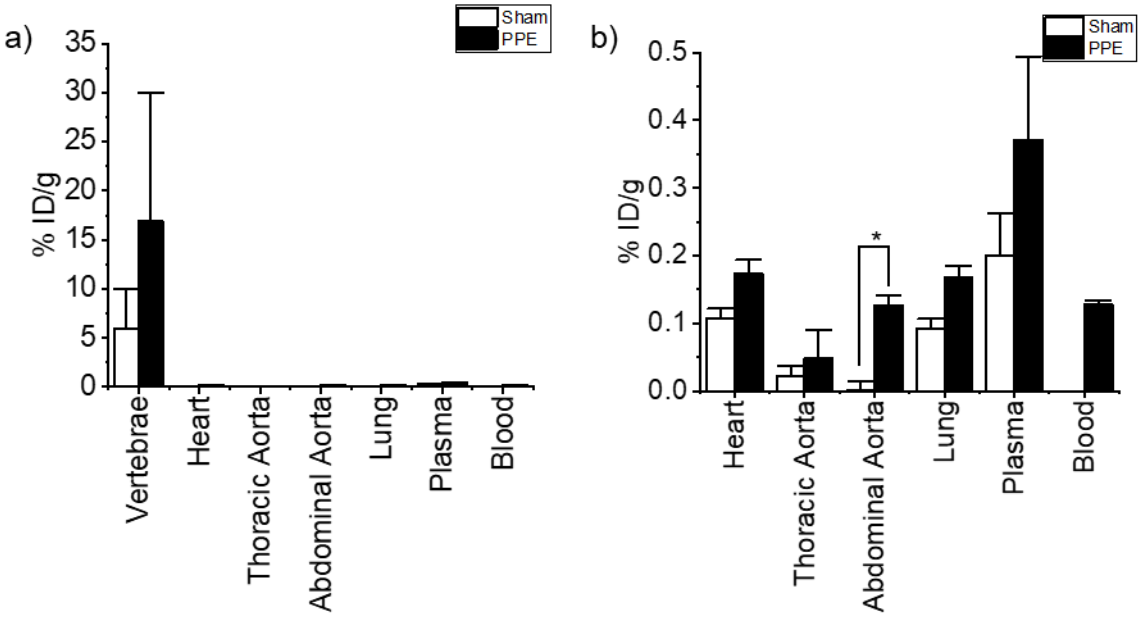

Figure 24: Harvesting of tissue from sham and PPE groups post PET/CT scan demonstrates biodistribution of Na[^{18}F]F. (a) Highest Na[^{18}F]F uptake seen in vertebrae. (b) Uptake in the abdominal aorta of PPE model showed a significantly greater uptake compared to sham equivalent ($p<0.05$). Mean and standard error shown.

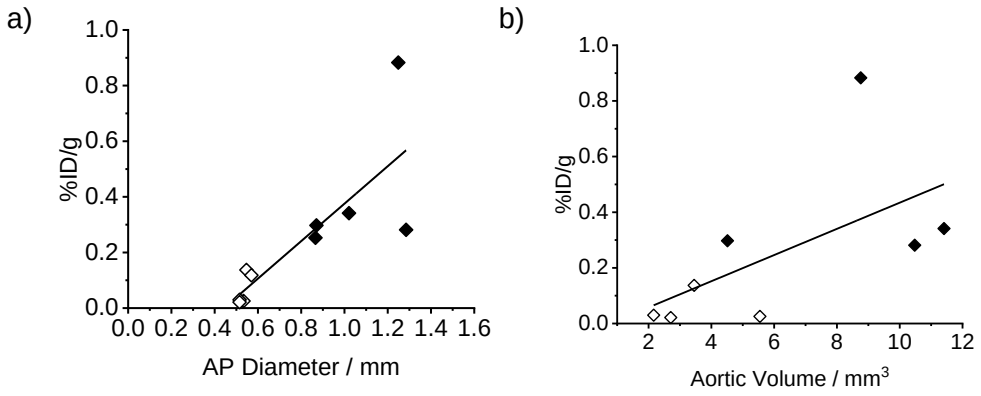

Figure 25: Correlation of *ex vivo* gamma counting derived %ID/g with AAA ultrasound measurements collected from sham and PPE-treated mice. (a) displays AP diameter and (b) shows aortic volume.

PET/CT imaging of sham and PPE models (day 14 post intervention), however, did not show any difference in uptake in the AA (Figure 26). Quantifying for SUV_{mean}, SUV_{max} and TBR_{max} showed high variability in both sham and PPE models, as well as no significant difference between groups (Figure 27 and Table 12) .

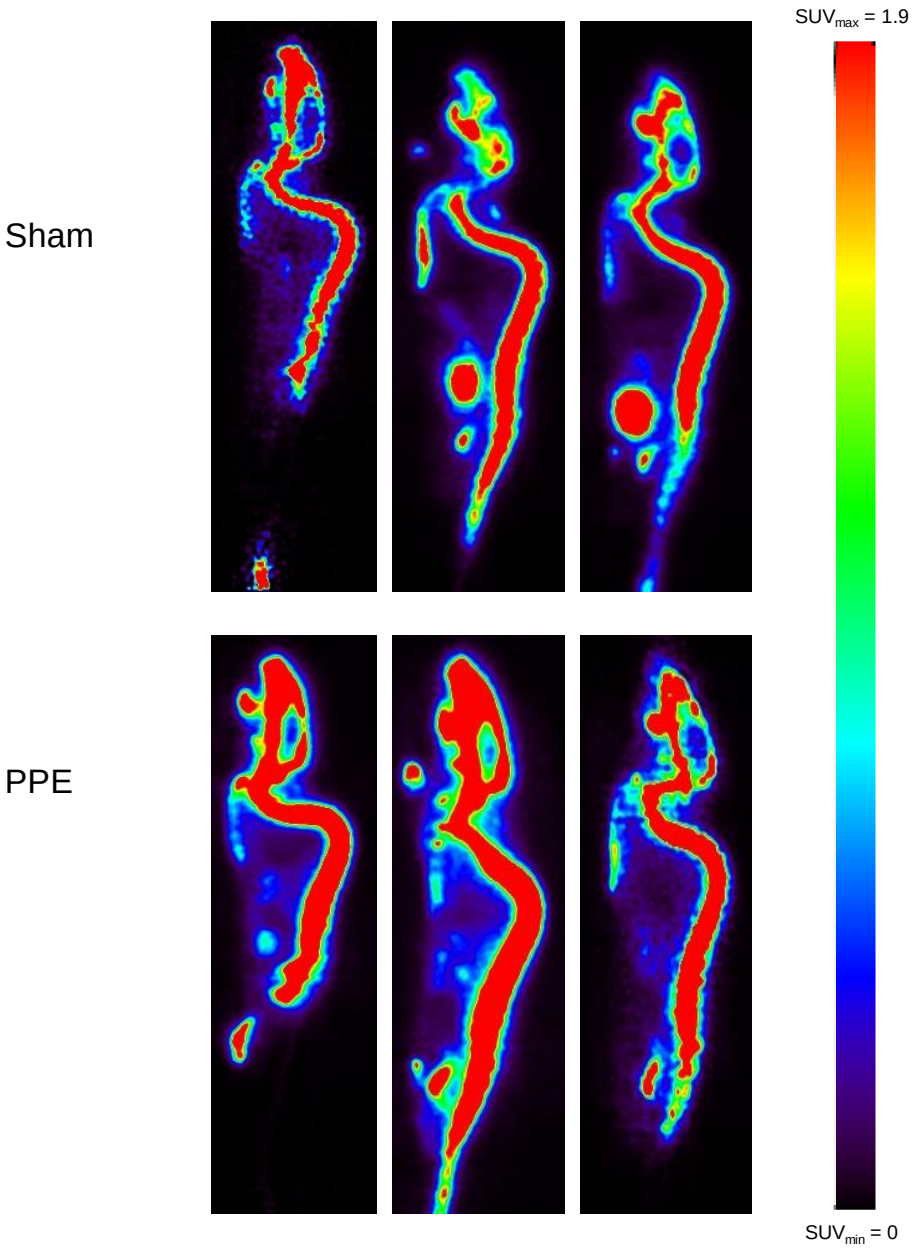

Figure 26: Sagittal PET/CT image slices of Na[^{18}F]F uptake in sham vs PPE mice. Na[^{18}F]F uptake was seen in the skeleton. No uptake was recorded in the AA of the PPE group

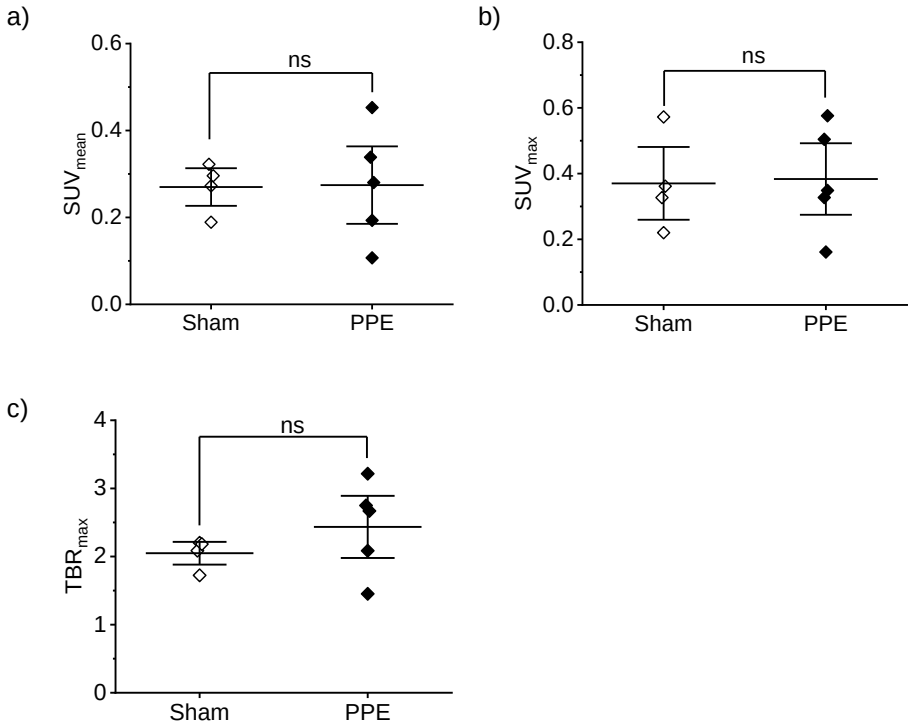

Figure 27: Distribution of PET/CT-derived metrics in sham and PPE mice. No difference was observed between groups when (a) SUV_{mean}, (b) SUV_{max} and TBR_{max} (c) were quantified. ns, not significant. Mean and standard error shown.

Table 12: Quantification of Na[^{18}F]F uptake in AAA in sham vs PPE AAA models.

Metric	Sham	PPE	P value
SUV_{mean}	0.27 ± 0.029	0.27 ± 0.059	0.95
SUV_{max}	0.37 ± 0.074	0.38 ± 10.0	0.90
TBR_{max}	2.0 ± 0.11	2.4 ± 0.30	0.31

Although *ex vivo* gamma counting detected a difference in accumulation of Na[^{18}F]F and thus suggesting increased microcalcifications in PPE AAA tissue as seen in histological data (Figure 22), PET/CT imaging at day 14 demonstrated no signal uptake in the AA. This could be due to the poor sensitivity of the Albira scanner or detection of microcalcification growth at day 14 is not the most suitable time point for this model. As shown previously by our group, aneurysm induction using peri-adventitial PPE was detectable at day 3 post surgery when measuring for aortic volume, and day 7 post surgery when measuring for aortic diameter

(59). As aortic diameter is normally used in the clinic to stratify patients for treatment and management over time, a longitudinal PET/CT experiment was designed to see if Na[^{18}F]F detection of microcalcification development in PPE model occurs at an earlier time-point, and verify a time-point at which Na[^{18}F]F could reliably detect AAA.

Longitudinal tracing of Na[^{18}F]F uptake in the AA demonstrated no significant difference between sham and PPE models at day 7 and day 14. Figure 28-31 demonstrates example images at day 7 and day 14 for both sham and PPE models. Strong Na[^{18}F]F uptake is seen in the bone, as previously reported, however there is an absence of detectable signal in the AA in both models. Quantifying for both SUV_{max} and TBR_{max} in the AA shows no difference in metric at the two time points and between models (Figure 32 and Table 13). CT angiography (CTA) was used as quality assurance for aneurysm induction at Day 15 post intervention (Figure 33). Similar to the results seen in Figure 23, aneurysm induction was seen in the PPE model for this cohort. A significant difference between aortic diameter and aortic volume was seen between sham and PPE groups (Table 14).

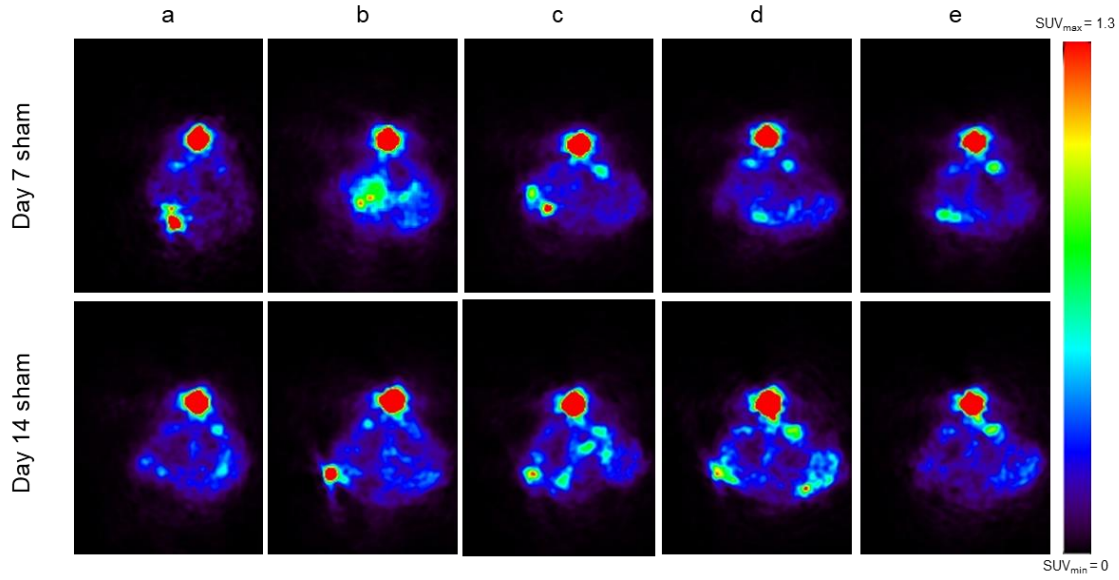

Figure 28: Raw PET/CT transverse image sections of the abdomen of sham control mice at day 7 and day 14 post surgery. This longitudinal tracing demonstrated no uptake of Na[^{18}F]F in the AA at either time-point for any mouse. Each image column (a-e) depicts slices from individual mouse.

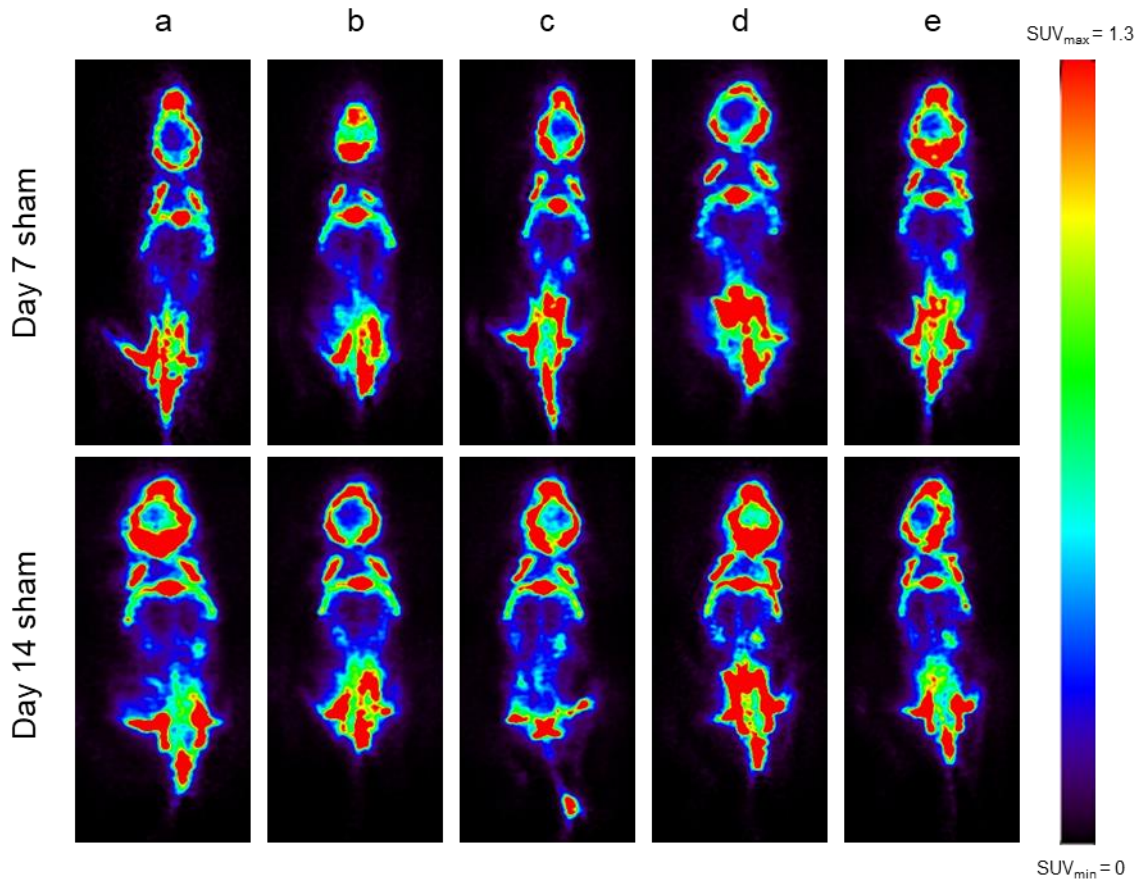

Figure 29: Raw PET/CT coronal image sections of the abdomen of sham control mice at day 7 and day 14 post surgery. This longitudinal tracing demonstrated no uptake of Na[^{18}F]F in the AA at either time-point for any mouse. Each image column (a-e) depicts slices from individual mouse.

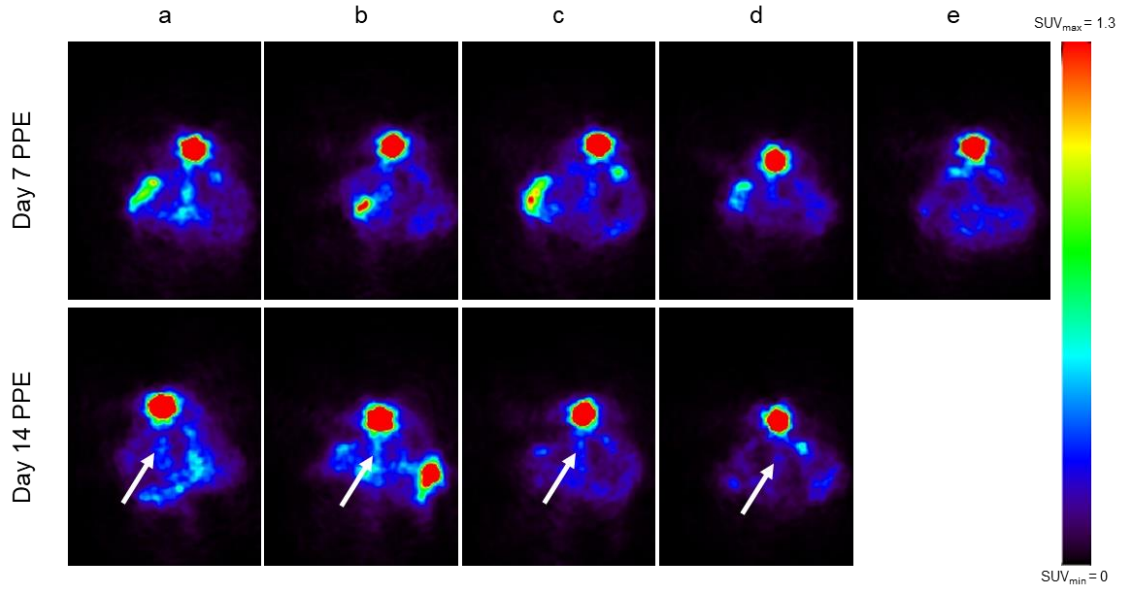

Figure 30: Raw PET/CT transverse image sections of the abdomen of PPE-treated mice at day 7 and day 14 post surgery. Heterogeneous Na[^{18}F]F uptake is perceived in AAA at day 14 (white arrow), with no signal seen at day 7. The day 14 scan for e failed and is therefore not represented. No uptake in the AA is seen in these mice. Each image column (a-e) depicts slices from individual mouse.

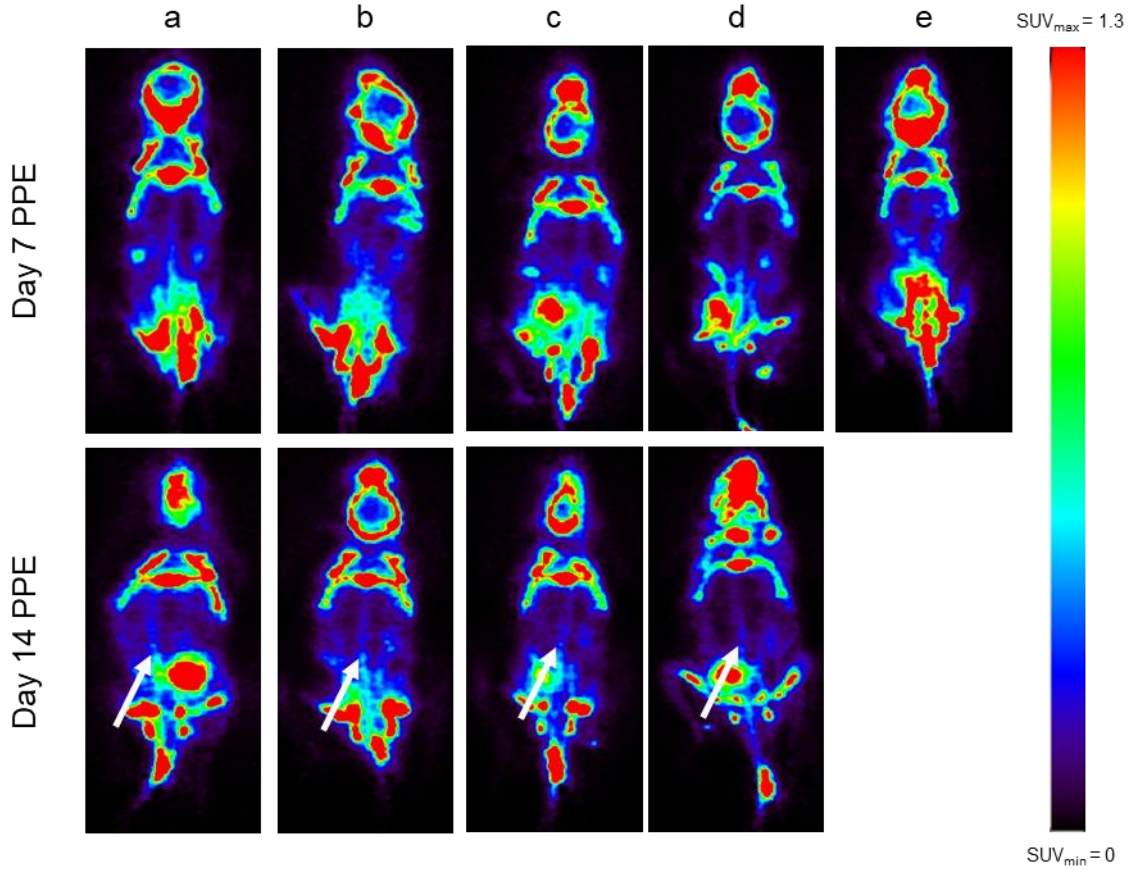

Figure 31: Raw PET/CT coronal image sections of the abdomen of PPE-treated mice at day 7 and day 14 post surgery. Heterogeneous Na[^{18}F]F uptake is perceived in AAA at day 14 (white arrow), with no signal seen at day 7. The day 14 scan for e failed and is therefore not represented. No uptake in the AA is seen in these mice. Each image column (a-e) depicts slices from individual mouse.

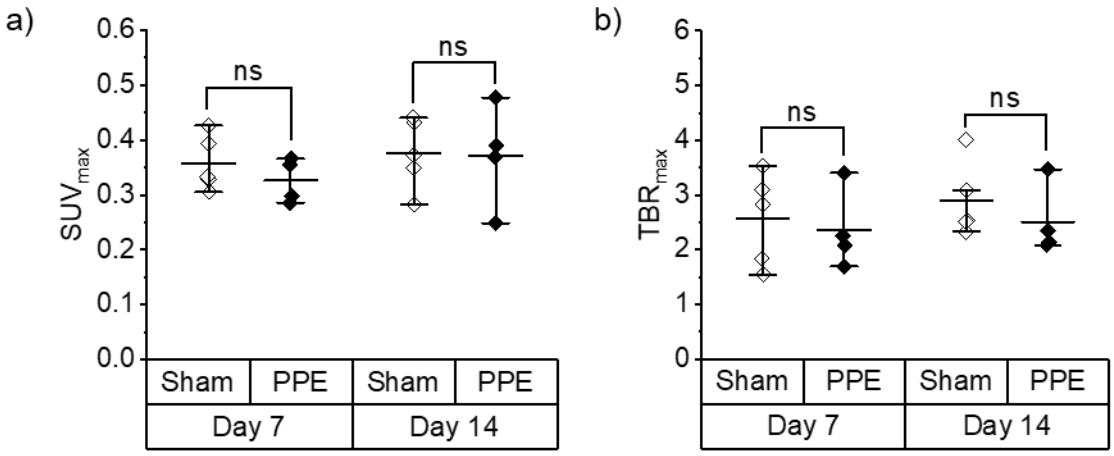

Figure 32: Quantification of aortic Na[^{18}F]F uptake in sham and PPE groups at day 7 and day 14 post surgery. (a) displays SUV_{max} and (b) shows TBR_{max} No significant difference was recorded between groups sham for either metric at any time-point. n=5 sham, n=4 PPE. Mean and standard error shown.

Table 13: PET/CT metrics of AA Na[^{18}F]F uptake in Day 7 and Day 14 sham vs PPE models

	SUV_{max}			TBR_{max}		
Time / day	Sham	PPE	P value	Sham	PPE	P value
7	0.36 ± 0.022	0.33 ± 0.020	0.35	2.6 ± 0.38	2.4 ± 0.37	0.70
14	0.38 ± 0.029	0.37 ± 0.047	0.93	2.9 ± 0.31	2.5 ± 0.32	0.42

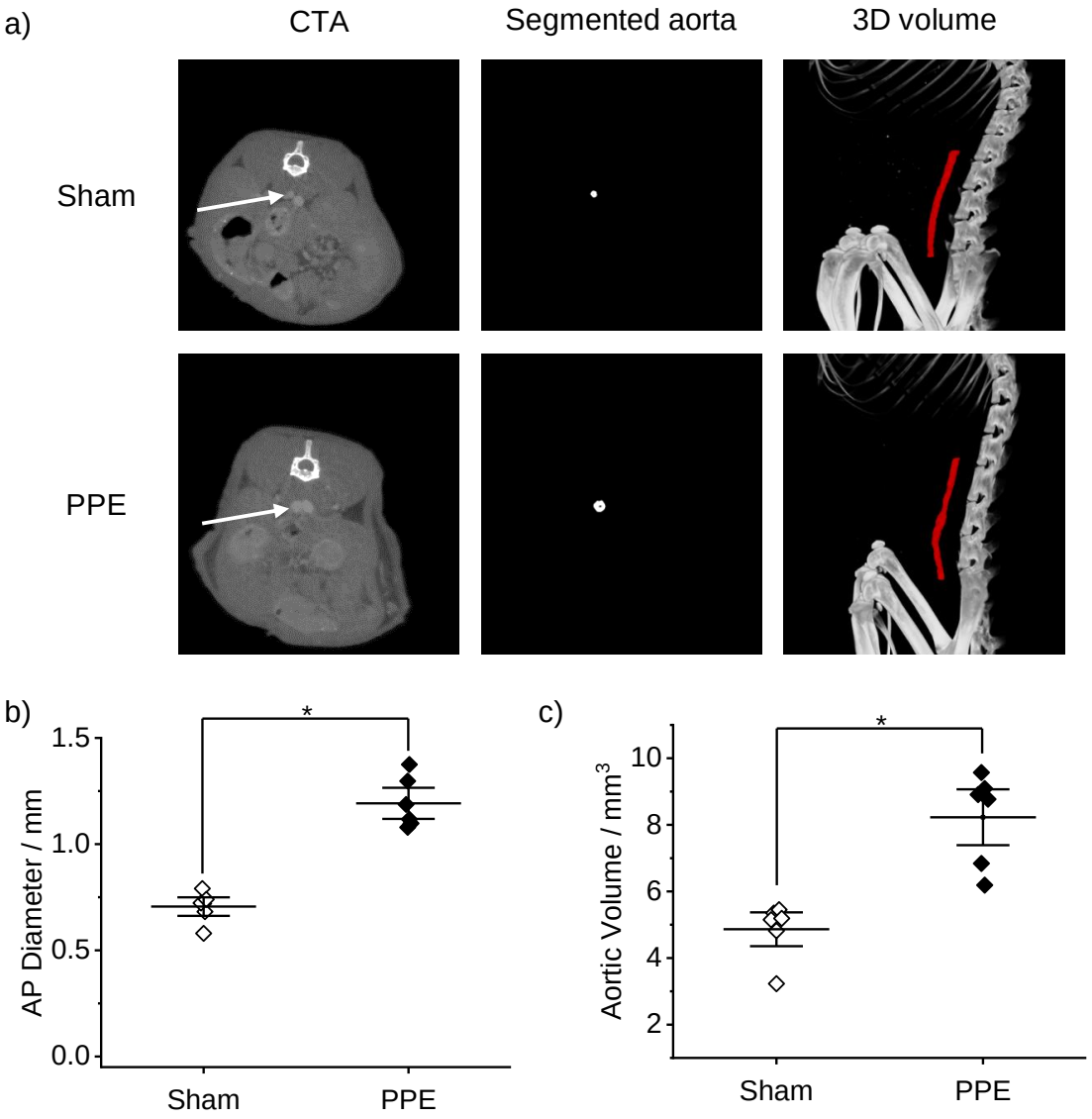

Figure 33: Aortic measurements as determined by CTA. (a) shows example slices generated using CTA and segmentation of the AA in sham and PPE-treated mice. Quantification of (b) AP diameter and (c) aortic volume were significantly increased in the PPE group vs sham ($p<0.05$). (n=6 sham, n=6 PPE). Mean and standard error shown.

Table 14: Aortic diameter and Aortic volume measurements from CTA

Metric	Sham	PPE	P value
Aortic Diameter / mm	0.71 ± 0.029	1.2 ± 0.049	0.0000066
Aortic volume / mm^3	4.9 ± 0.34	8.2 ± 0.56	0.00043

To confirm the presence or absence of microcalcifications at day 7 in PPE model, a dedicated day 7 biodistribution experiment was conducted in a small cohort. Analysis of uptake in AA showed no difference in uptake between sham and PPE model (ID/g 0.05 ± 0.05 vs 0.01221 ± 0.00912 respectively), suggesting the absence of Na[^{18}F]F uptake and a lack of microcalcification development at day 7 in the PPE model (Figure 34a). Histological analysis of aortic sections revealed no presence of microcalcifications in day 7 sham and PPE AA tissue (Figure 34b).

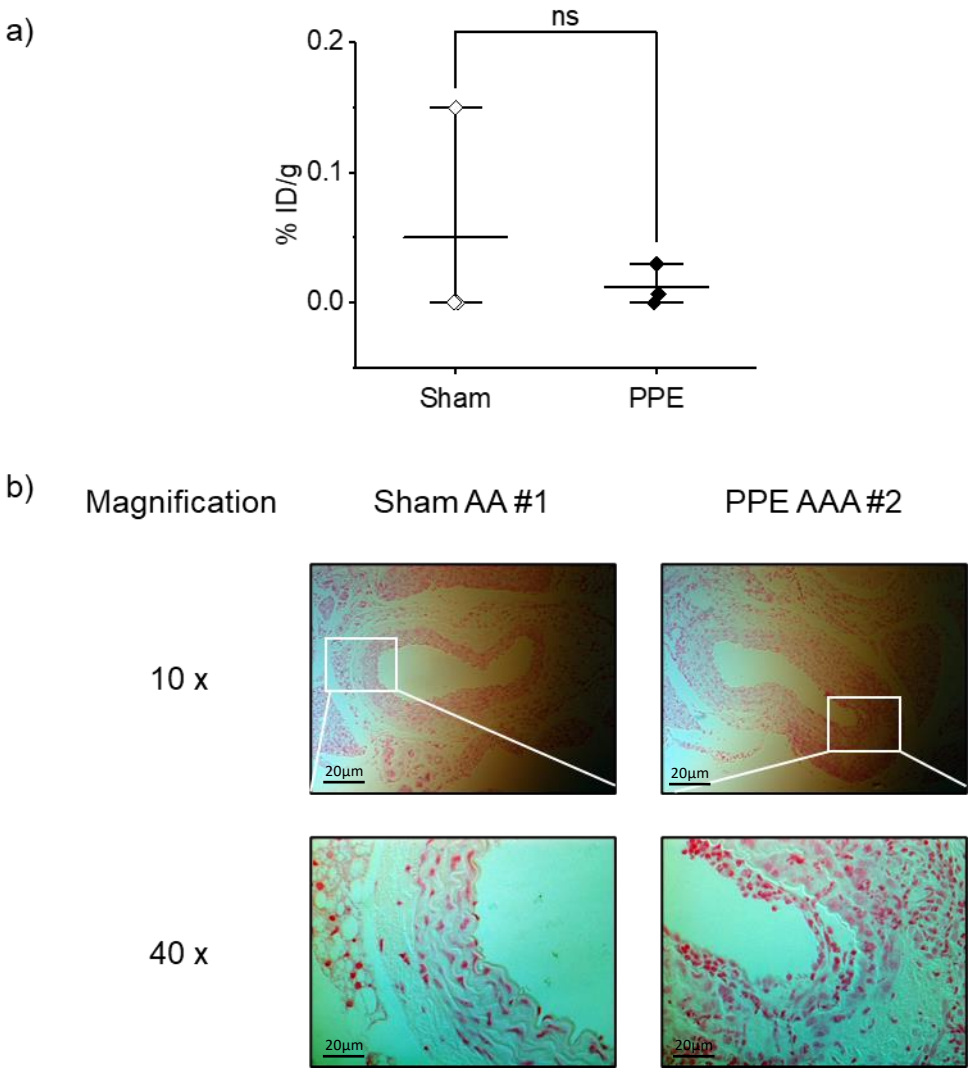

Figure 34: Day 7 investigation of the presence of microcalcification deposits. a) *Ex vivo* gamma counting demonstrated no significant difference between sham and PPE AA tissue (p=ns). Mean and standard error shown. b) Von Kossa staining of AA tissue from sham and PPE mice at the day 7 time-point. Images are shown at 10x and 40x magnification. Von Kossa stain present in PPE AA tissue sections. (n=3 sham, n=3 PPE)

Although PET/CT imaging did not show Na[^{18}F]F uptake in the AA at either time-point for the PPE-treated group, biodistribution analysis (Figure 24) and von Kossa staining (Figure 22) suggests Na[^{18}F]F uptake was greatest in the PPE model day 14 post surgery.

3.4 Kernel reconstruction algorithms on preclinical AAA model data

As demonstrated in both $CaCl_2$ and PPE AAA PET/CT investigation, image analysis demonstrated there was no difference in quantification between sham and the surgical models. However, biodistribution demonstrated increased Na[^{18}F]F uptake in both the $CaCl_2$ model, and in the PPE model at day 14, compared to their respective sham controls. In addition, von Kossa staining confirmed the presence of microcalcifications in both models. The absence of Na[^{18}F]F signal could be due to the poor sensitivity of the scanner and the anatomical location of the spine in relation to the AA, with the large signal from the spine masking that from the AA. In an attempt to improve the quantification of AA in Na[^{18}F]F AAA clinical scans, our group have recently reported the application of two novel PET reconstruction methods (221,224).

Using the STIR framework and the model of the Albira scanner (developed by Mr Harry Tunnicliffe, still in development), the PET/CT data acquired from this study were reconstructed using both KEM and HKEM methodologies to determine if an underlying AA signal can be detected in the preclinical models, and further inform whether the PPE model would be useful for study of microcalcification development. Only line profile data is reported due to the developmental stage of the model. In addition, a normalisation profile was not completed at this stage of development and could also augment the displayed line profiles.

3.4.1 Optimisation of reconstruction algorithms

To understand how the reconstruction algorithm affects image quality in terms of noise, the baseline models were reconstructed over a range of iterations to determine which image should be used for analysis. Figure 35 shows the plot of intensity against iteration for each reconstruction algorithm tested. The measured intensity reflects a line profile drawn through the vertebrae in the sagittal plane. Here the advanced reconstruction algorithms (KOSEM and HKOSEM) are compared against algorithms used in the clinic. The graph demonstrates for

OSEM as iteration increases, the measured intensity in the bone increases. This suggests that with a higher iteration, more noise is incorporated into the image. For both advanced reconstruction algorithms, as iteration increases the intensity remains stable, suggesting no additional noise is incorporated into the image sets. From the graph, MLEM, KOSEM and HKOSEM images after 8 iterations were used for analysis.

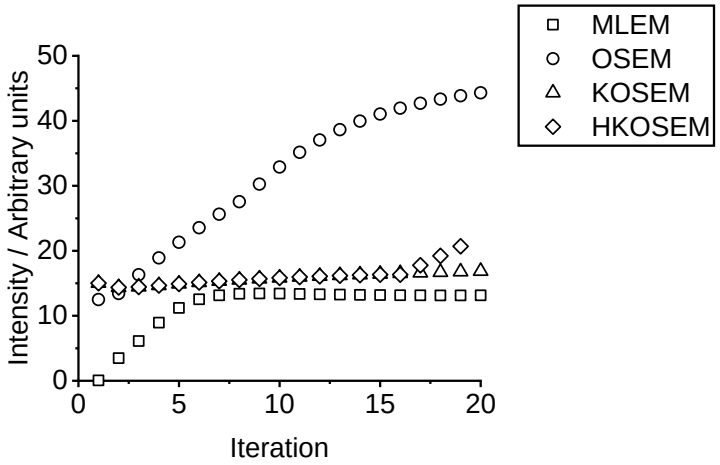

Figure 35: Optimization of PET/CT reconstruction methods on baseline model. For both standard reconstructions (i.e. MLEM and OSEM), as the number of iterations increase, intensity increases due to noise. Both advanced reconstruction methods (KOSEM and HKOSEM) suppress noise as iteration increase.

Figure 36 shows representative slices from reconstructed baseline models using MLEM, KOSEM and HKOSEM. Plotting a line profile through the AA and spine shows the intensity profile from each reconstruction follows a similar pattern. However, looking at the distance around the AA and bone more closely shows some peaks revealed by KOSEM and HKOSEM reconstructions. This suggests that additional information from KOSEM and HKOSEM algorithms have detected Na[^{18}F]F signal uptake missed by MLEM reconstruction.

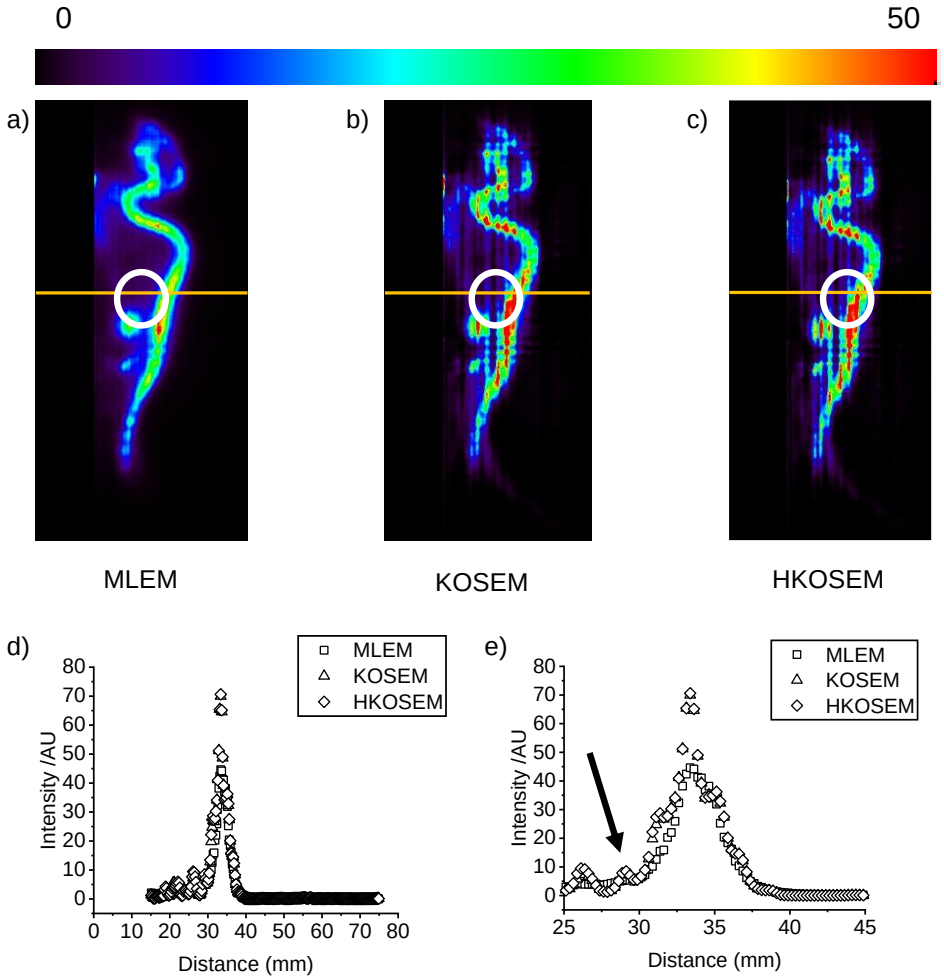

Figure 36: STIR reconstruction of baseline model. Representative images of MLEM (a), KOSEM (b) and HKOSEM (c) raw PET/CT data with area highlighted for AA region (circle) with line profiles. Line profile graphs show that KOSEM and HKOSEM reconstructions reveal additional features (black arrow) from PET reconstruction which are not present in the standard MLEM reconstruction (d,e).

MLEM, KOSEM and HKOSEM reconstructions were conducted on a sham model from the $CaCl_2$ cohort study, with representative images presented in Figure 37 and 38 respectively. A line profile through the AA revealed a similar intensity profile across each of the algorithms. On closer inspection, no additional information is revealed around the AA, suggesting the signal from the bone is not masking any signal from the AA. On the other hand, images reconstructed on a peri-adventitial $CaCl_2$ model shows additional features present in the advanced reconstruction algorithms that are masked from the bone in MLEM reconstruction (Figure 38). This suggests that the application of additional imaging data maybe required for quantification of Na[^{18}F]F uptake in the AA.

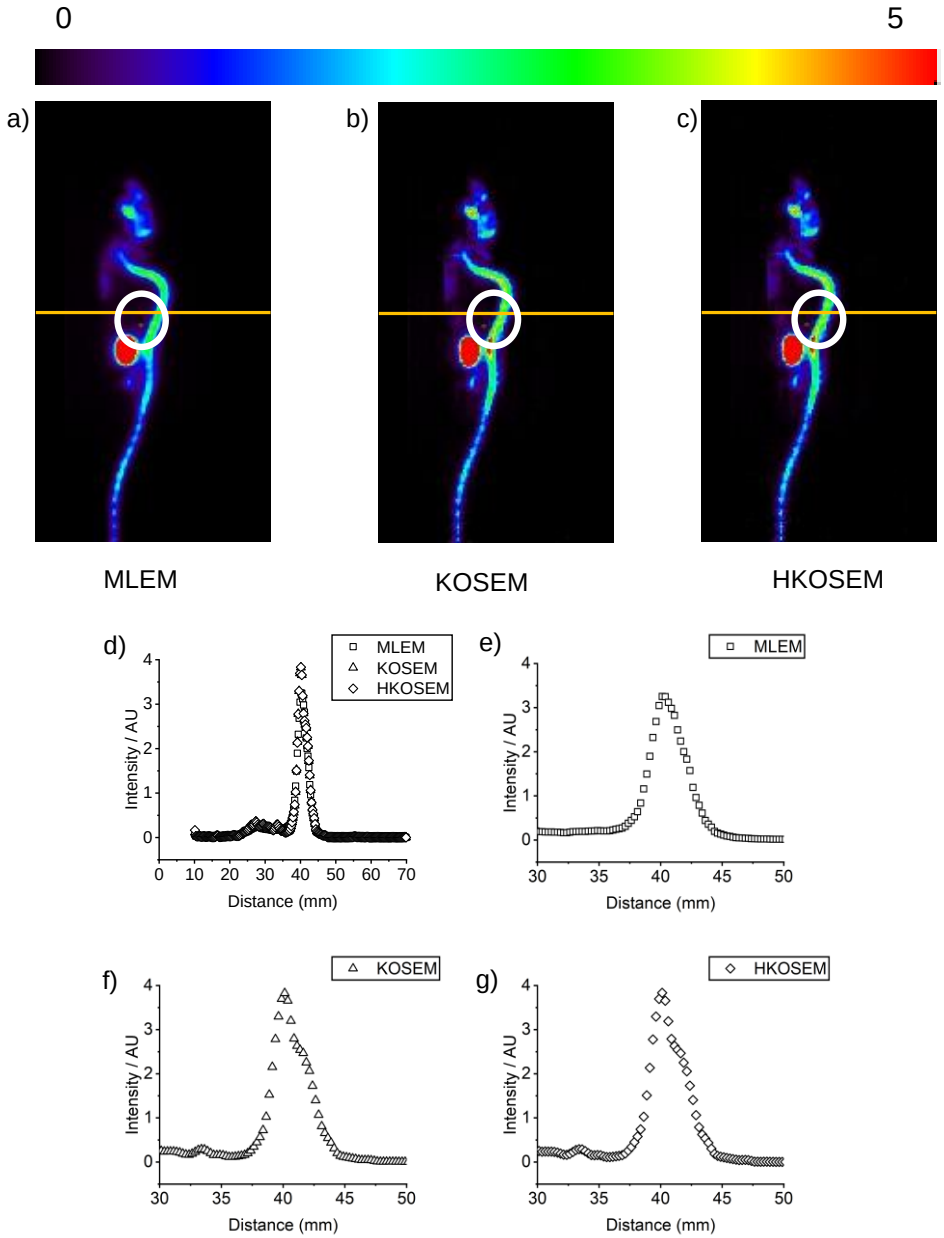

Figure 37: STIR reconstruction of sham model from $CaCl_2$ cohort. Representative images of MLEM (a), KOSEM (b) and HKOSEM (c) raw PET images with area highlighted for AA region (circle) with line profile drawn. Composite line profile graphs for each reconstruction algorithm (d). No difference in line profile was shown between MLEM (e), KOSEM (f) and HKOSEM (g) reconstruction algorithms.

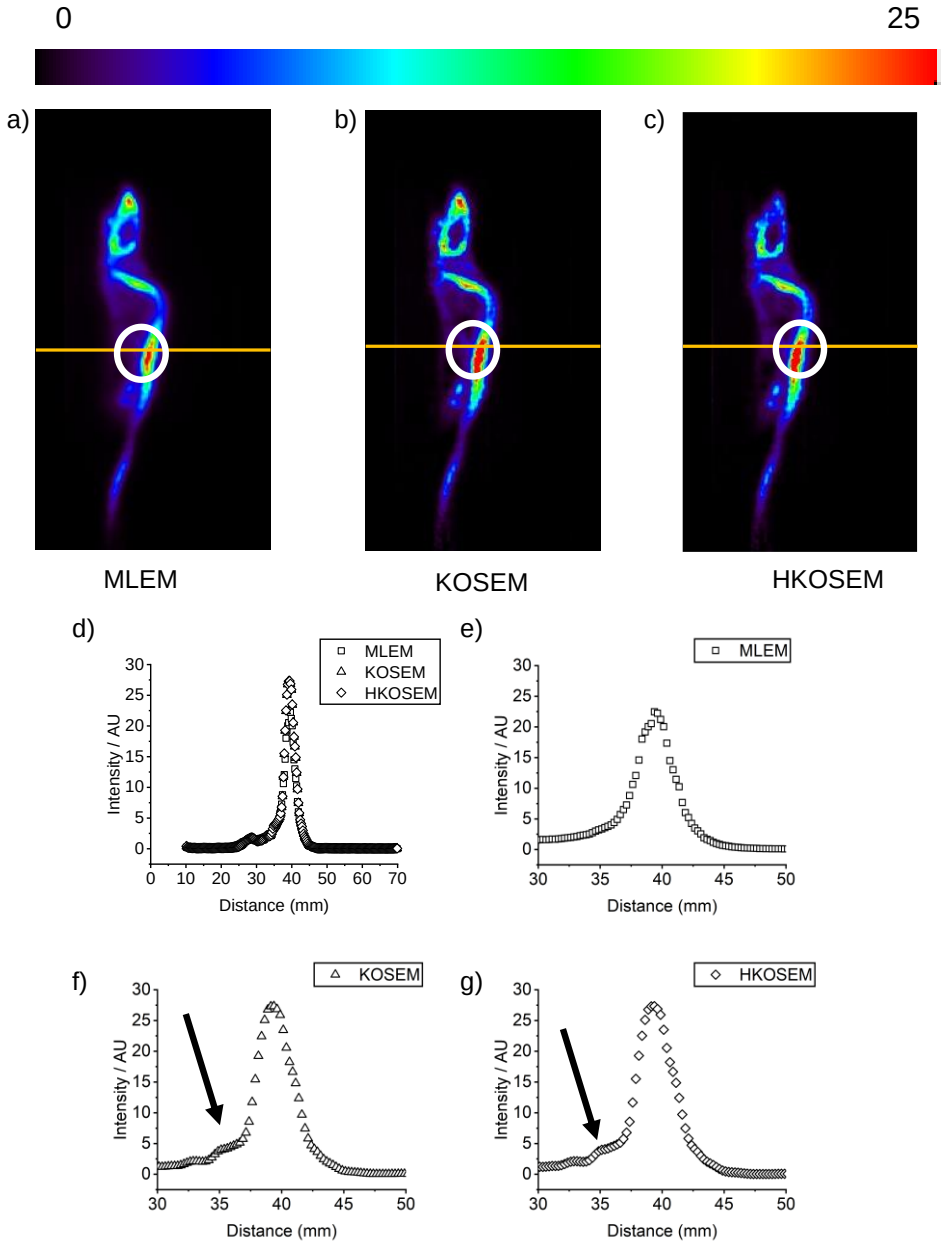

Figure 38: STIR reconstruction of $CaCl_2$-treated mice. Representative images of MLEM (a), KOSEM (b) and HKOSEM (c) raw PET/CT data with area highlighted for AA region (circle) with line profiles. (d) Composite line profile drawing of three reconstruction algorithms. Line profile graph of MLEM reconstruction showed no AA peak (e). Line profile graphs show peak revealed by KOSEM (f) and HKOSEM (g) reconstructions, however the peak is still masked by the large peak from the vertebrae (black arrow).

MLEM, KOSEM and HKOSEM reconstruction algorithms were performed on sham and PPE models to determine if signal from the AAA is masked by the spine. Reconstructions on sham model (Figure 39) from the PPE cohort (Figure 40) reveals a similar result as to that reported in baseline and sham model, where no additional Na[^{18}F]F signal is masked by the spine. Advanced

reconstruction on a peri-adventitial PPE model however demonstrates no additional signal is revealed by the advanced reconstruction algorithms.

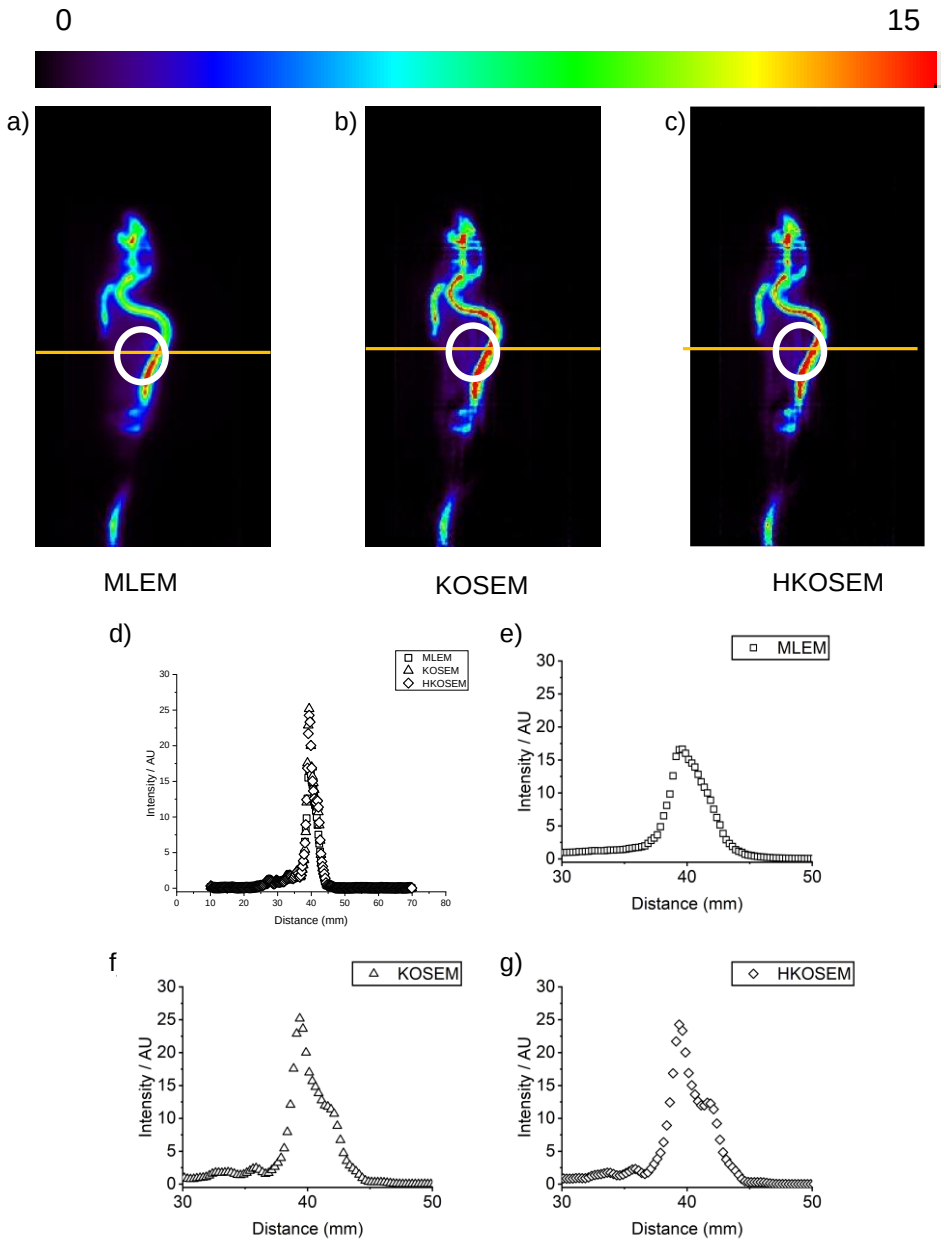

Figure 39: STIR reconstruction of sham model from PPE cohort. Representative images of MLEM (a) , KOSEM (b) and HKOSEM (c) raw PET images with area highlighted for AA region with line profile drawn. Composite line profile graphs for each reconstruction algorithm (d). No difference in line profile was shown between MLEM (e), KOSEM (f) and HKOSEM (g) reconstruction algorithms.

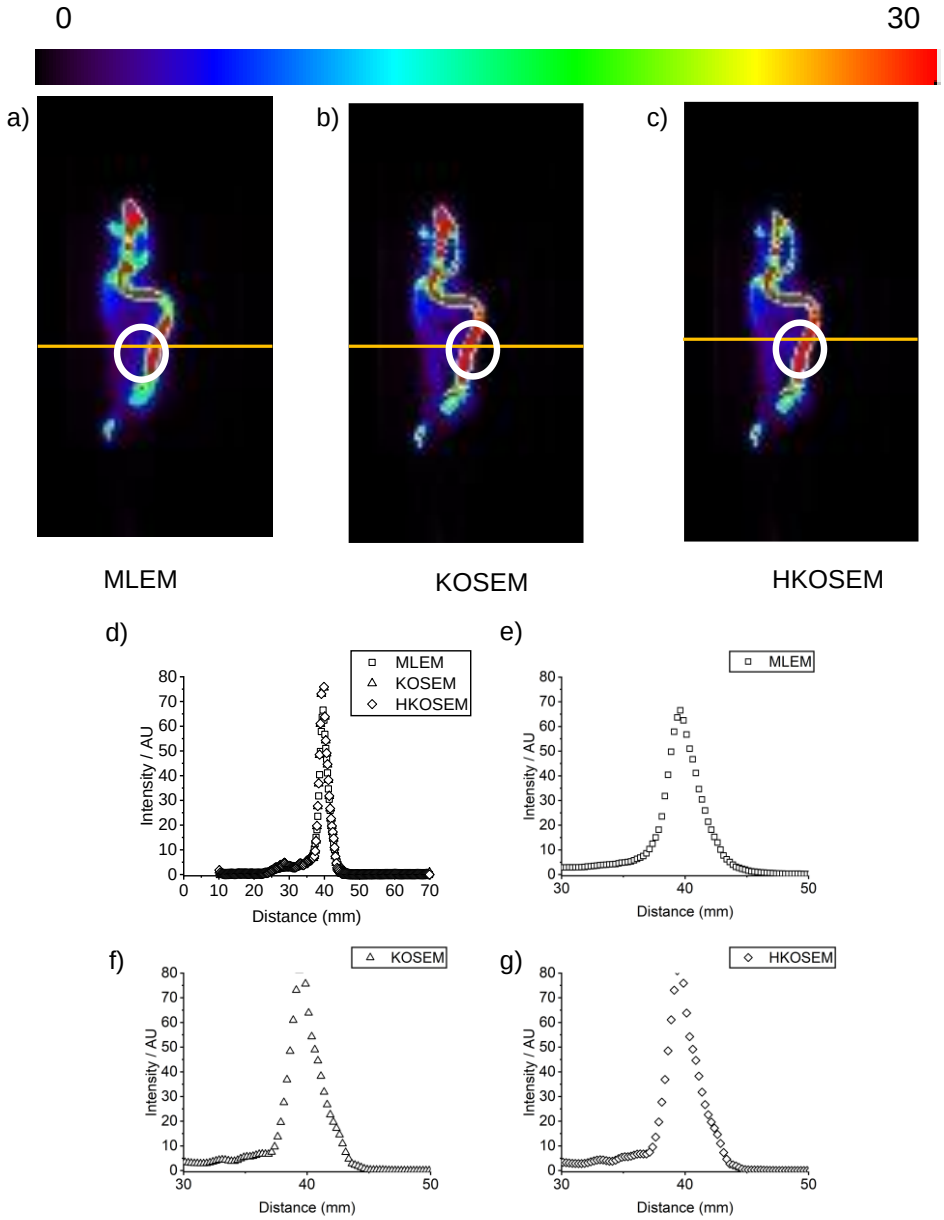

Figure 40: STIR reconstruction of PPE model from PPE cohort. Representative images of MLEM (a) , KOSEM (b) and HKOSEM (c) raw PET images with area highlighted for AA region with line profile drawn. Composite line profile graphs for each reconstruction algorithm (d). No difference in line profile was shown between MLEM (e), KOSEM (f) and HKOSEM (g) reconstruction algorithms.

One of the challenges in this study has been to validate and reproduce Na[^{18}F]F signal uptake, if any, in the PPE model of AAA to determine if the PPE model could be useful in studying the relationship between microcalcification and aneurysm progression and how this links to the clinical scenario. Unfortunately due to technical limitations with the scanner, no Na[^{18}F]F signal was detectable in the AAA using µPET/CT. However, *ex vivo* gamma counting demonstrated a

significant difference in uptake between day 14 sham and PPE AA and von kossa stain showed the presence of a small percentage of microcalcification deposits in PPE AA tissue. Due to the inconsistency between histological staining, *ex vivo* gamma counting and *in vivo* PET/CT, the absence or presence of calcification markers in AAA tissue and their cellular localisation was investigated.

3.5 Expression of calcification markers in PPE model

The results from Section 3.3 demonstrated Na[^{18}F]F uptake in the PPE model was elevated compared to sham controls using *ex vivo* biodistribution. The presence of microcalcification deposits in the aortic wall was also identified by von Kossa stain. It was therefore of interest to further study the biological drivers of microcalcification in this model.

Our group has developed a vascular smooth muscle lineage tracing model in mTmG mice to follow cellular remodelling in the PPE model of AAA. As described in Section 1.6, there is growing evidence that VSMC remodelling could be a driver of aneurysm formation through phenotypic switching from the native contractile state to a synthetic state. The lineage traced model, as described in Section 2, harbours a membrane specific fluorescent tomato probe which is excised by tamoxifen injection to reveal a downstream green fluorescent protein in VSMC. Therefore, all cells are labelled red in these mice prior to tamoxifen treatment. After tamoxifen exposure, VSMCs switch from red to green and remain green irrespective of de-differentiation or remodelling and which allows cells to be tracked. The mTmG model is a powerful tool to examine localisation of protein expression in specific cell types, and in this case, VSMC.

The group have previously shown (Craggs *et al.* in preparation) that abdominal aorta treated with peri-adventitial application of PPE express lower levels of α-SMA at day 14 post surgery in lineage traced VSMC. This suggests in the PPE model, VSMC remodelling is observed in aneurysm formation.

To investigate whether calcification occurs in the PPE model, a range of calcification markers, including BMP2, BMP4, RUNX2 and OPG, were studied to determine their cellular origin and contribution to aneurysm formation due to their involvement in both bone mineralisation and presence in atherosclerotic and AAA tissue, as described in Section 1.6.2.

3.5.1 BMP2 expression, but not OPG, elevated in PPE model

Figure 41 demonstrates example multichannel IF sections of mTmG AAA tissue. These sections display mGFP and mTom expression (green and red, respectively), confirming the presence of VSMCs in the medial layer, and other cell types in the aortic wall. Blue DAPI staining indicates cell nuclei, yellow staining highlights nuclei expressing BMP2, and purple staining indicates OPG expression. Visually, the aortic diameters in sham mice are consistent across the time-points of the experiment. However, in PPE mice, as the time course increases, aortic diameter also increases (initiated at day 7), demonstrating dilation of the aorta.

To determine baseline levels of BMP2 and OPG expression, baseline (no surgical intervention) mTmG aorta sections were stained. As shown in Figure 42, no baseline expression of BMP2 or OPG was detected. Figure 43 shows day 1 post surgery sections, in which no BMP2 or OPG expression was seen in either sham or PPE mice. However, at day 7 post surgery, BMP2 expression was seen in the aorta in PPE sections, which was absent in sham counterparts (Figure 44). BMP2 expression was seen in cells expressing predominantly mGFP (lineage traced VSMCs). OPG expression was absent in the PPE model. In addition, the aortic lumen in the PPE group is visually thicker, implying possible remodelling and aneurysm development. BMP2 expression in cells also expressing mGFP was seen in PPE sections from day 14 (Figure 45) and day 28 (Figure 46), albeit at a lower amount at the latter time-point. At day 84, no BMP2 or OPG expression was seen in either sham or PPE sections (Figure 47).

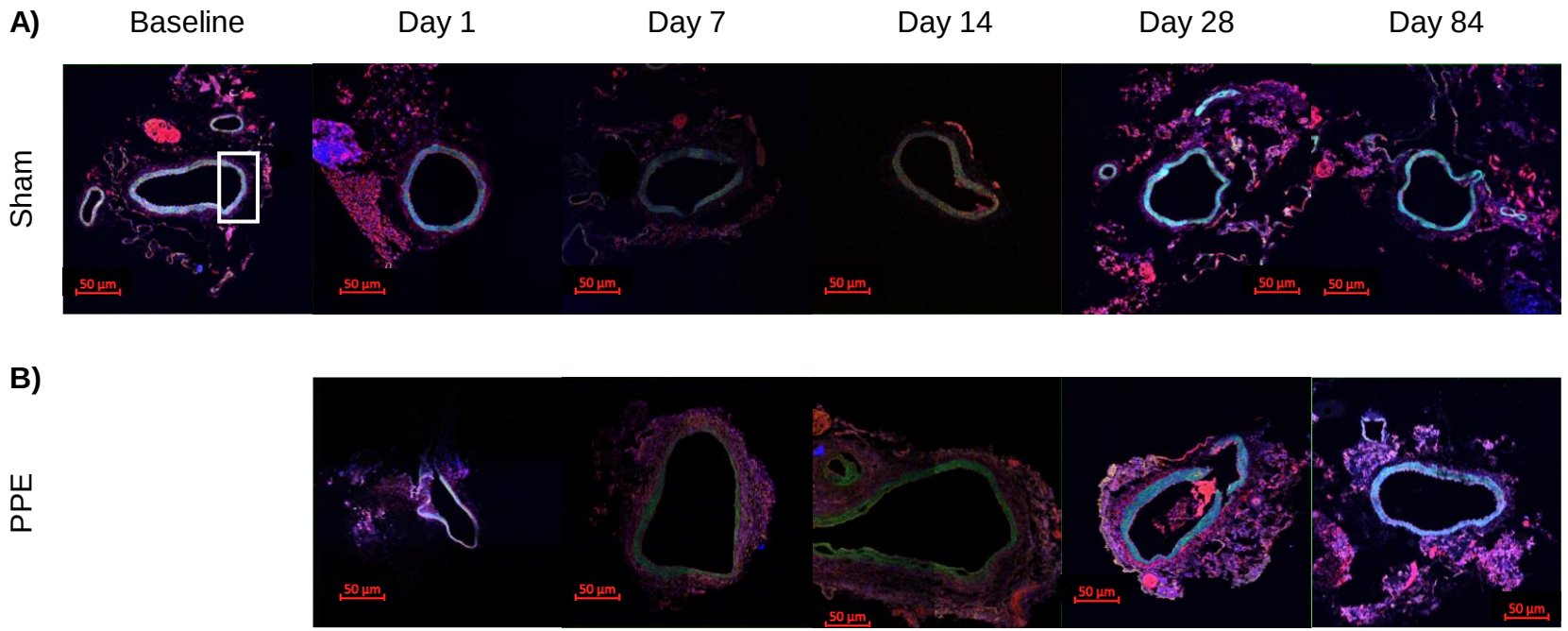

Figure 41: 20x tile scan of (A) Sham and (B) PPE AAA tissue sections stained for BMP2 and OPG at baseline, day 1, day 7, day 14, day 28 and day 84 post surgery. Dilation of the abdominal aorta is seen in PPE tissue sections from day 7 post surgery. The white box indicates a typical region of interest for analysis. Stains include mGFP = green (VSMC), mTom = red = all cells, DAPI = blue (nuclei), BMP2 = yellow, OPG = purple.

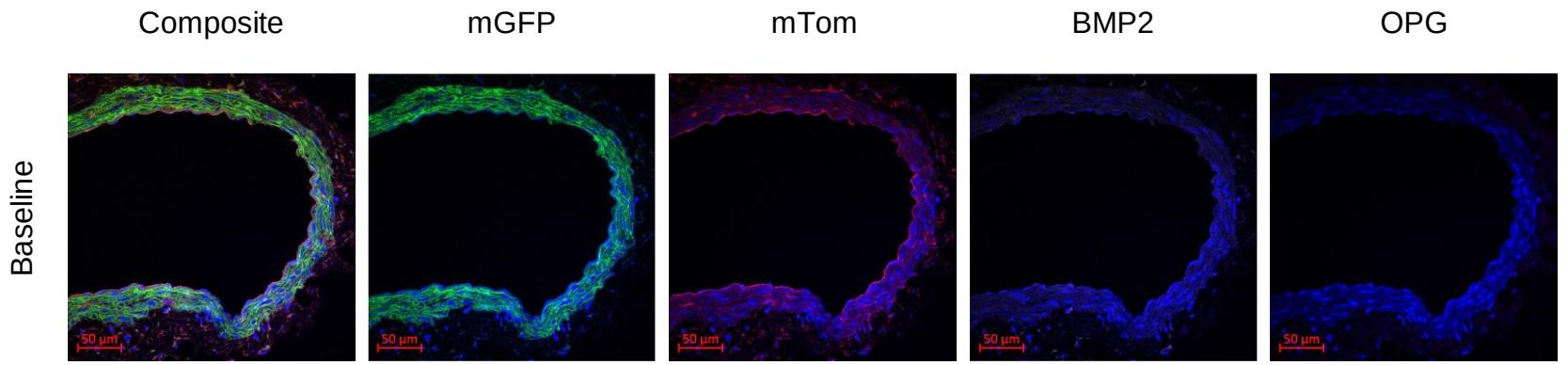

Figure 42: Representative 40x z-stack section of baseline mTmG AAA tissue sections stained for BMP2 and OPG. Expression of BMP2 and OPG were not detected at baseline. Stains include mGFP = green (VSMC), mTom = red (all cells), DAPI = blue (nuclei), Runx2 = yellow (514), BMP4 = purple (647). n=4

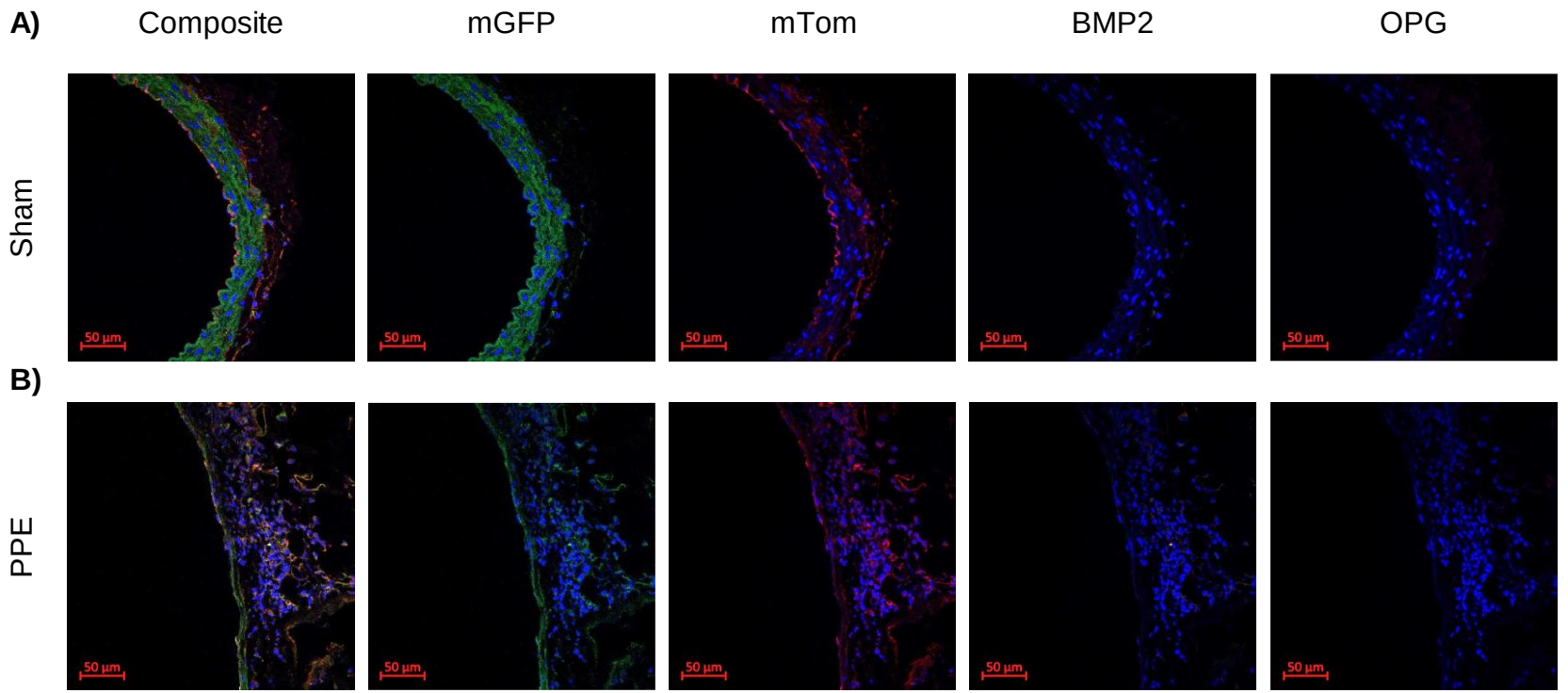

Figure 43: Representative 40x z-stack section of day 1 post surgery (A) sham and (B) PPE AAA tissue sections stained for BMP2 and OPG. No detectable levels of BMP2 or OPG was seen in either model. Stains include mGFP = green (VSMC), mTom = red (all cells), DAPI = blue (nuclei), BMP2 = yellow (514), OPG = purple (647). n=3 sham, n=4 PPE

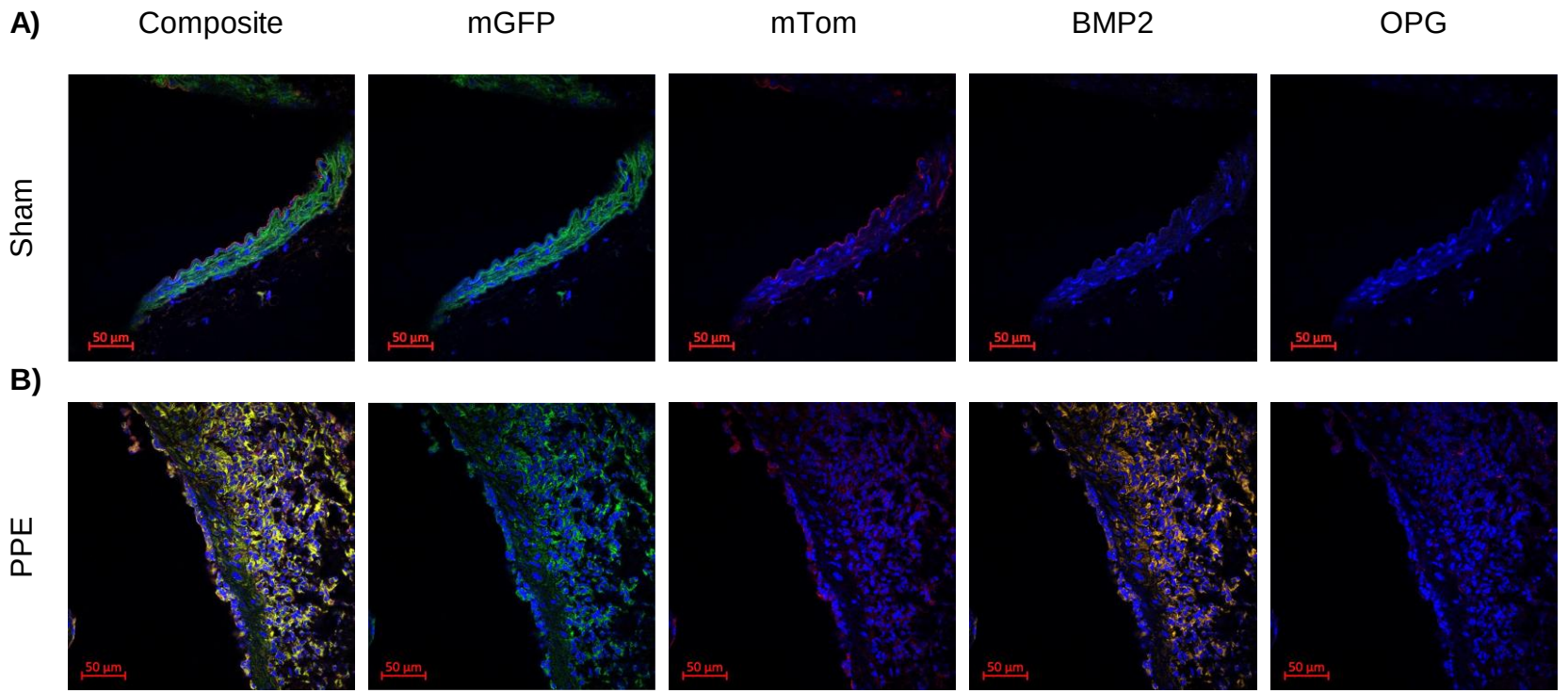

Figure 44: Representative 40x z-stack section of day 7 post surgery (A) sham and (B) PPE AAA tissue sections stained for BMP2 and OPG. mGFP expressing cells (VSMC) show an upregulation of BMP2 protein in PPE model compared to sham. Expression located in the medial and adventitial layers. Stains include mGFP = green (VSMC), mTom = red (all cells), DAPI = blue (nuclei), BMP2 = yellow (514), OPG = purple (647). n=5 sham, n=5 PPE

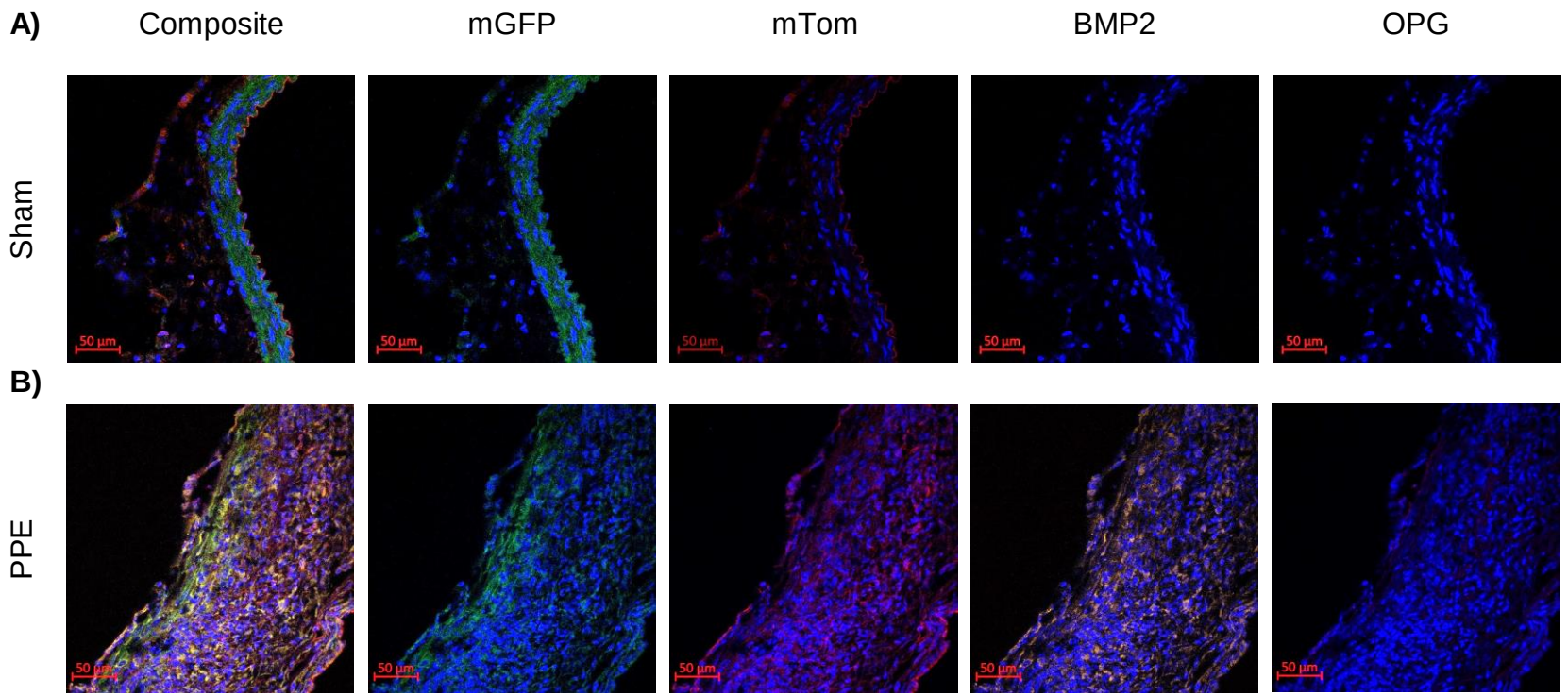

Figure 45: Representative 40x z-stack section of day 14 post surgery (A) sham and (B) PPE AAA tissue sections stained for BMP2 and OPG. mGFP expressing cells (VSMC) show an upregulation of BMP2 protein in PPE model compared to sham. Expression located in the medial and adventitial layers Stains include mGFP = green (VSMC), mTom = red (all cells), DAPI = blue (nuclei), BMP2 = yellow (514), OPG = purple (647). n=3 sham, n=7 PPE

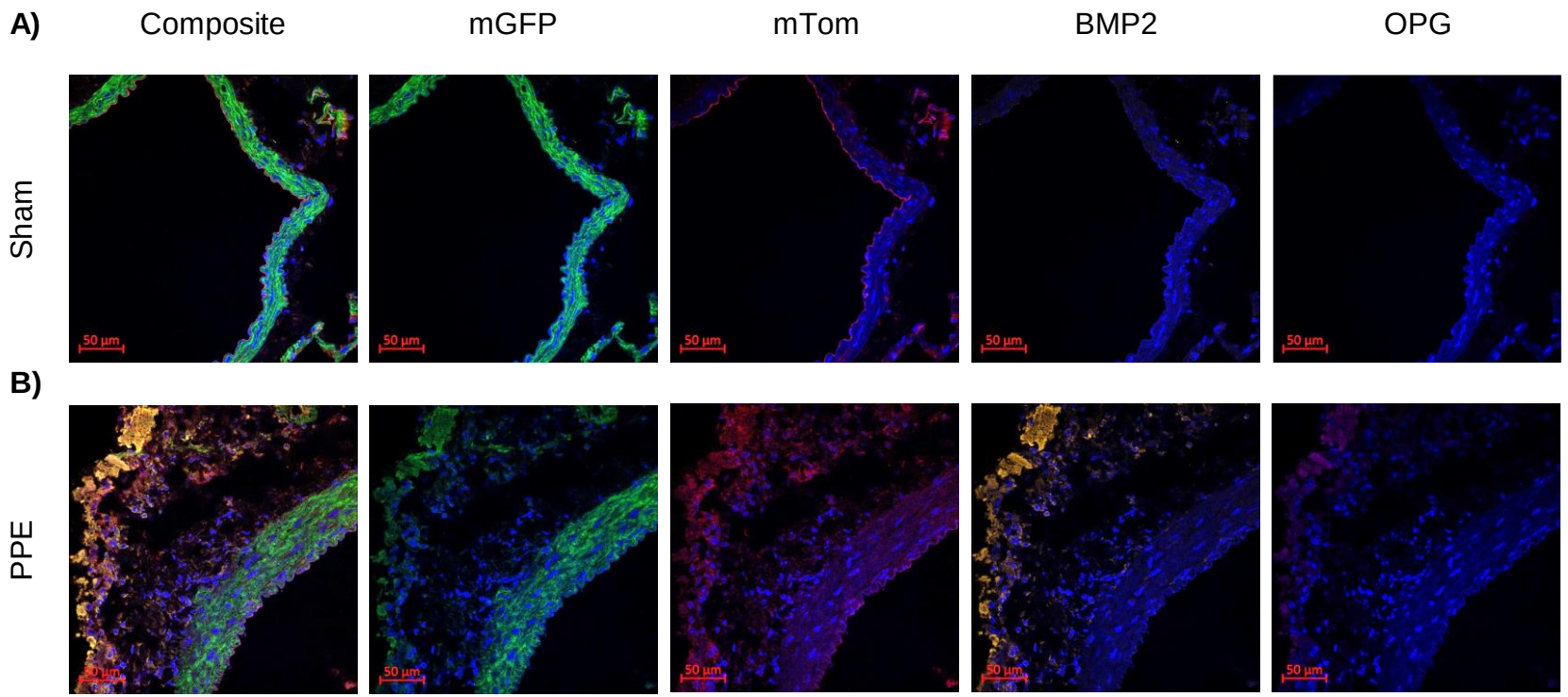

Figure 46: Representative 40x z-stack section of day 28 post surgery (A) sham and (B) PPE AAA tissue sections stained for BMP2 and OPG. mGFP expressing cells (VSMC) show an upregulation of BMP2 protein in PPE model compared to sham. Expression located in the medial and adventitial layers Stains include mGFP = green (VSMC), mTom = red (all cells), DAPI = blue (nuclei), BMP2 = yellow (514), OPG = purple (647). n=4 sham, n=3 PPE

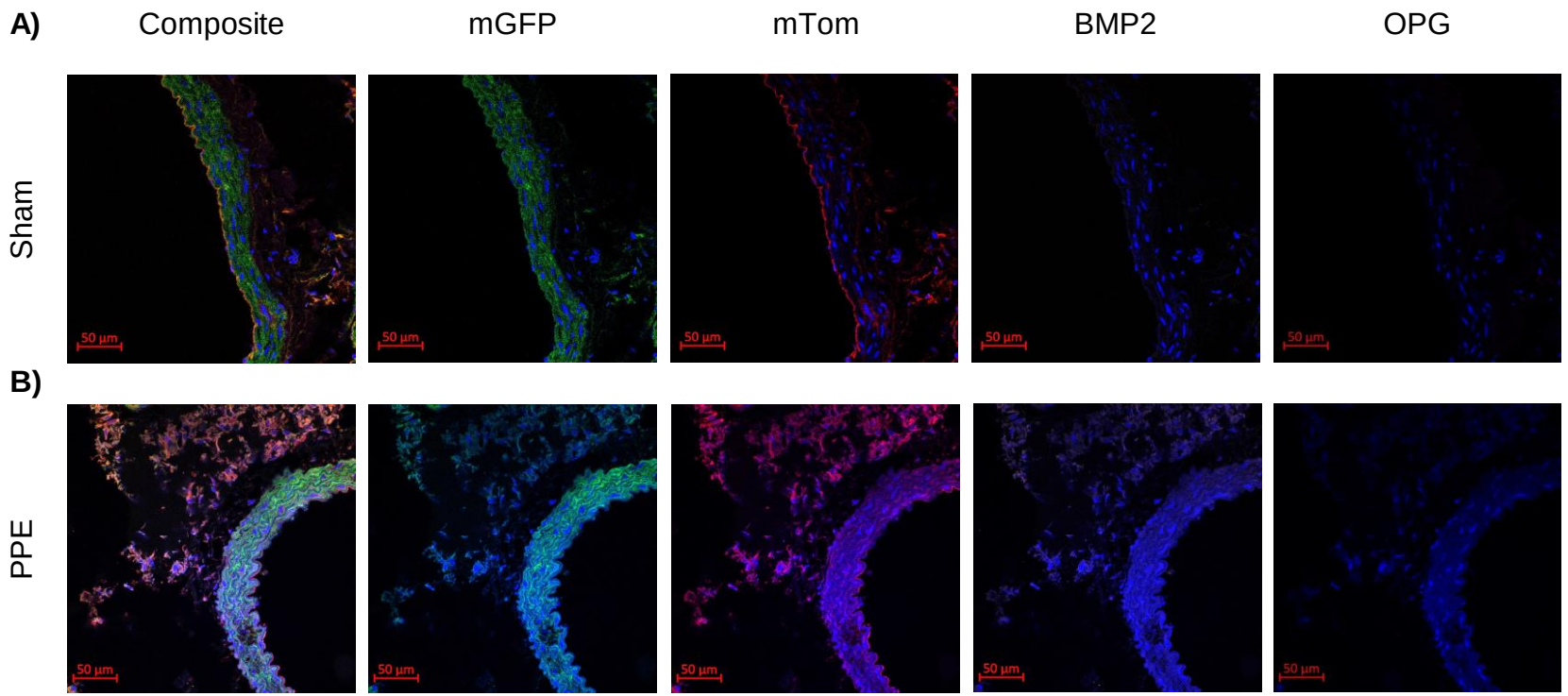

Figure 47: Representative 40x z-stack section of day 84 post surgery (A) sham and (B) PPE AAA tissue sections stained for BMP2 and OPG. No detectable levels of BMP2 or OPG was seen in either model. Stains include mGFP = green (VSMC), mTom = red (all cells), DAPI = blue (nuclei), BMP2 = yellow (514), OPG = purple (647). n=3 sham, n=2 PPE

Quantifying cells expressing mGFP, mTom, BMP2 or OPG demonstrates the remodelling process in PPE AAA model (Figure 48). The number of nuclei (i.e. DAPI positive cells) increases in the PPE model and peaks at day 14 post surgery before returning to baseline at day 84 (Figure 48a). The number of nuclei positive for mGFP expression peaks at day 7 before returning to baseline at day 84, demonstrating VSMC remodelling in the PPE model (Figure 48b). The number of nuclei positive for mTom peaks at day 14 in the PPE model before returning to baseline (Figure 48c). The number of BMP2 positive nuclei peaks at day 7 and is still elevated at day 14 compared to sham equivalents, before returning to baseline (Figure 48d). No OPG expression was seen in sham or PPE aortic sections (Figure 48e). From the analysis, it suggests that BMP2 expression and possible microcalcification formation in the PPE model is initiated at day 7 and continues at day 14 before returning to baseline. This microcalcification is predominately in VSMC derived cells.

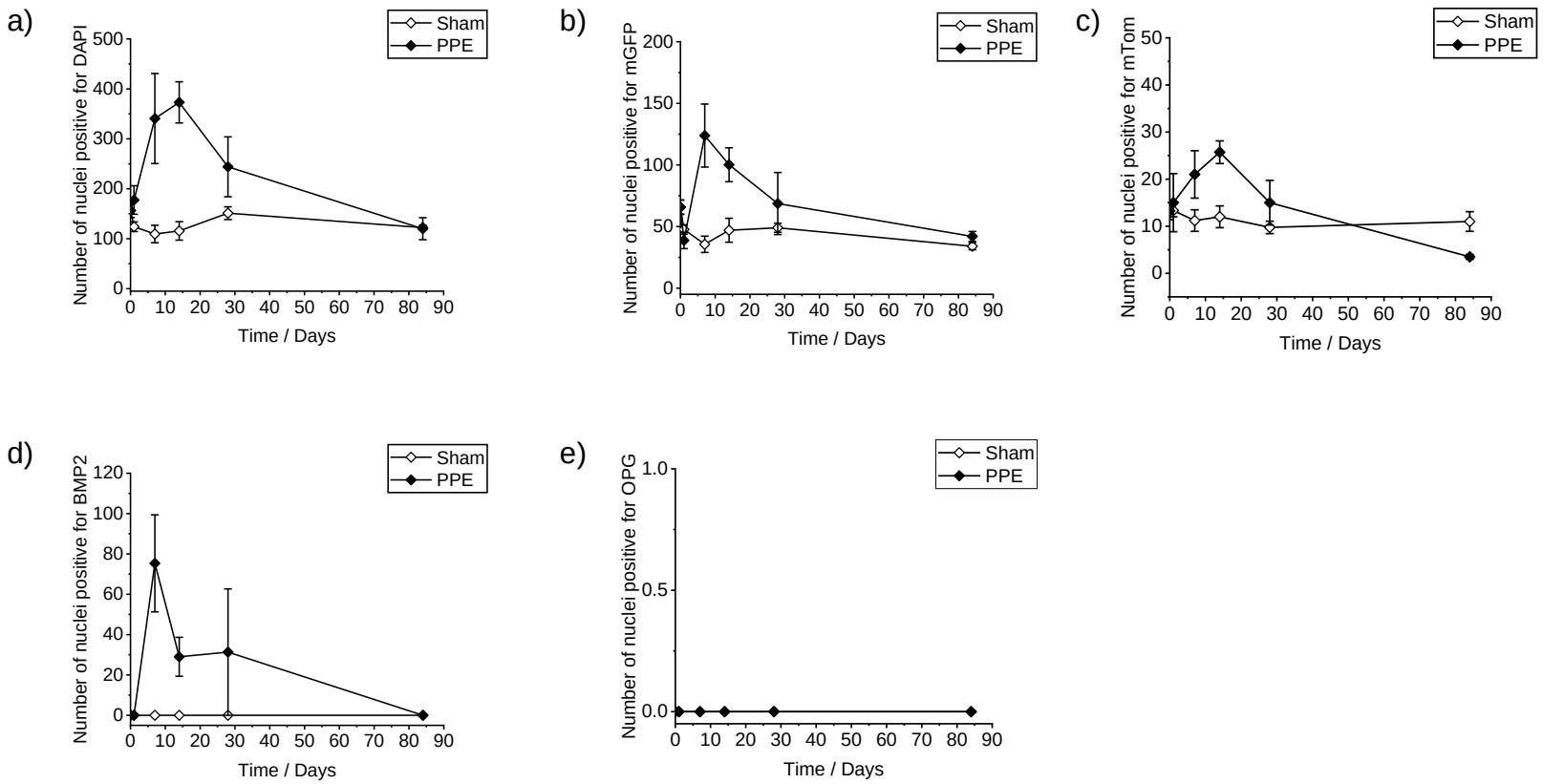

Figure 48: **Quantification of cells in sham and PPE aortic sections expressing various cellular proteins detected through cell staining and IF**. Data are presented as number of nuclei positive for: (a) DAPI, (b) mGFP, (c) mTom, (d) BMP2 and (e) OPG in sham and PPE aortic sections stained for BMP2 and OPG. Time points are baseline (denoted as day 0), day 1, day 7, day 14, day 28 and day 84. Mean and standard error shown.

To determine the predominant cell type expressing BMP2, cells positive for mGFP (i.e. lineage traced VSMC) AND BMP2 and cells positive for mTom AND BMP2 were quantified in day 7 and day 14 (Figure 49). Expression of BMP2 is highest in the PPE model, peaking at day 7 post surgery (P=0.004). BMP2 is predominately upregulated in mGFP positive cells (i.e., lineage traced VSMC), with some expression of BMP2 seen in mTom positive cells (28.0 ± 3.6% vs 4.1 ± 1.6%, P=0.01). This suggests that BMP2 expression is greatest in VSMC and peaks at day 7 post surgery. Counts for mGFP AND BMP2 positive cells is shown in Table 15 and Figure 49a and counts for mTom AND BMP2 positive cells is shown in Table 16 and Figure 49b,c.

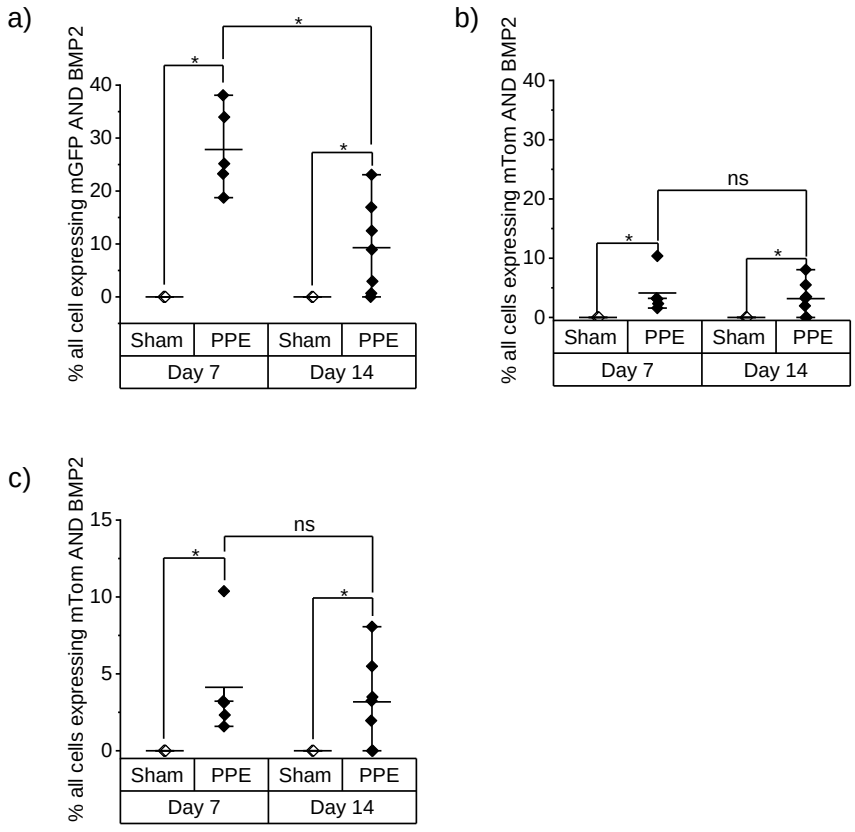

Figure 49: Percentage of cells in sham and PPE aortic sections expressing various cellular proteins as detected through cell staining and IF. Data are presented demonstrating cells positive for (a) mGFP and BMP2; (b) mTom and BMP2. (c) represents the results displayed in (b) zoomed to highlight the low percentage of cells expressing mTom and BMP2. ($p<0.05$; ns, not significant). Mean and standard error shown.

Table 15: Mean and SE of percentage of cells positive for mGFP AND BMP2

Time course / days	Sham	PPE	P value
7	0	28.0 ± 3.6	0.05
14	0	9.3 ± 3.3	0.05

Table 16: Mean and SE of percentage of cells positive for mTom AND BMP2

Time course / days	Sham	PPE	P value
7	0	4.1 ± 1.6	0.05
14	0	3.2 ± 1.1	0.05

Analysis of the cellular origin of BMP2 expressing cells indicate that most of the expression is predominately from lineage traced VSMC. This suggests that microcalcification formation in the PPE model of AAA is mainly associated with remodelling VSMC. Therefore, to confirm if mGFP AND BMP2 positive cells were VSMC and in their contractile or synthetic state, mTmG sections from day 7 and day 14 cohort were co-stained with BMP2 and α-SMA.

3.5.2 BMP2 expression is co-localised in mGFP positive cells, but NOT α-SMA cells

Representative slices from sham and PPE AAA slices at day 7 and day 14 are shown in Figure 50 and 51. In day 7 sham slices, BMP2 expression is unseen, similar to the results described in Section 5.1 and α-SMA expression is detected in the medial layer, co-localising with cells expressing mGFP cells. However in PPE day 7 AAA sections, BMP2 expression is elevated, as seen in Section 3.5.1 with α-SMA expression decreasing. The same pattern of expression in day 14 sham and PPE sections is seen. To quality assure that the expression of both α-SMA and BMP2 is in keeping with prior observations in our laboratory and Section 3.5.1, cells expressing mGFP AND α-SMA, mGFP AND BMP2 and mTom AND BMP2 were quantified as well as the counts for DAPI positive nuclei, mGFP positive nuclei and mTom positive nuclei.

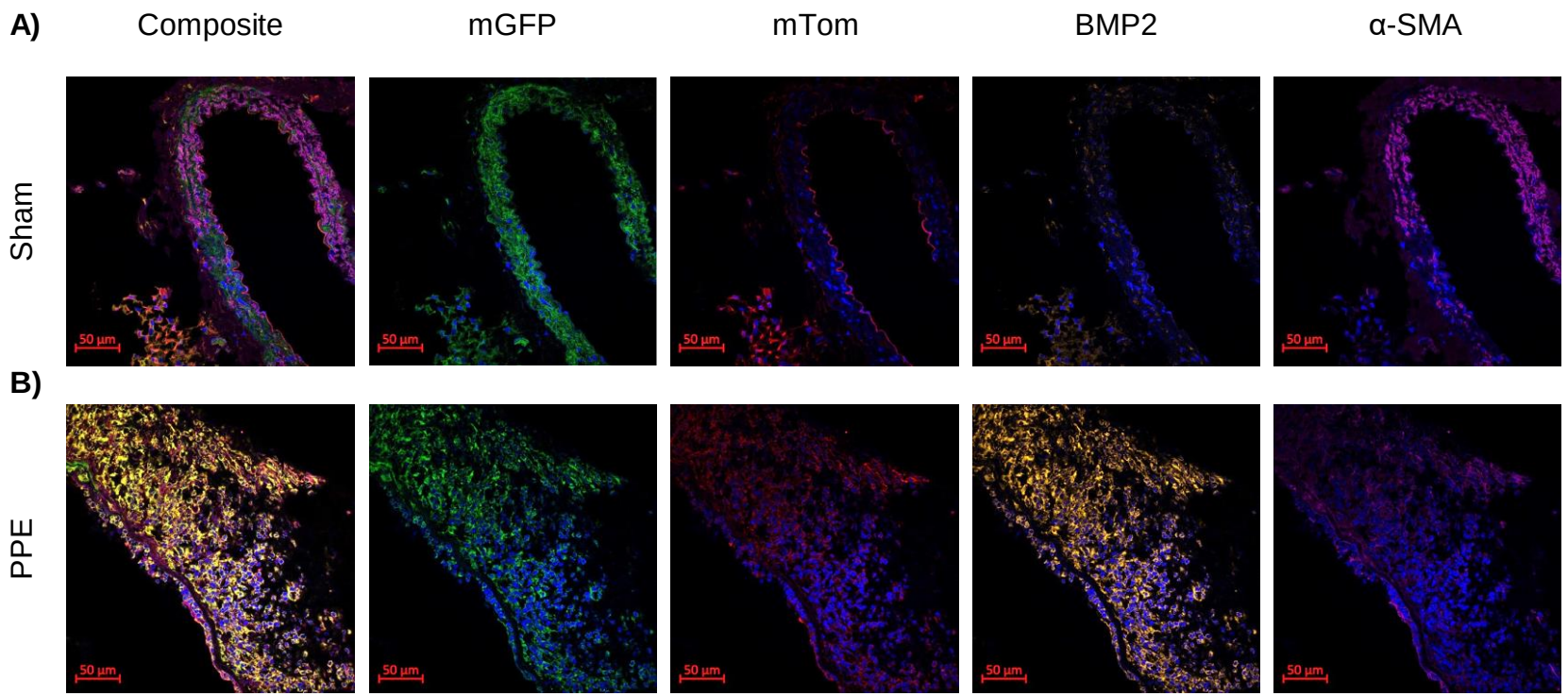

Figure 50: Representative 40x z-stack section of day 7 post surgery (A) sham and (B) PPE AAA tissue sections stained for BMP2 and α-SMA. Stains include mGFP = green (VSMC), mTom = red (all cells), DAPI = blue (nuclei), BMP2 = yellow (514), OPG = purple (647). n=5 sham, n=5 PPE

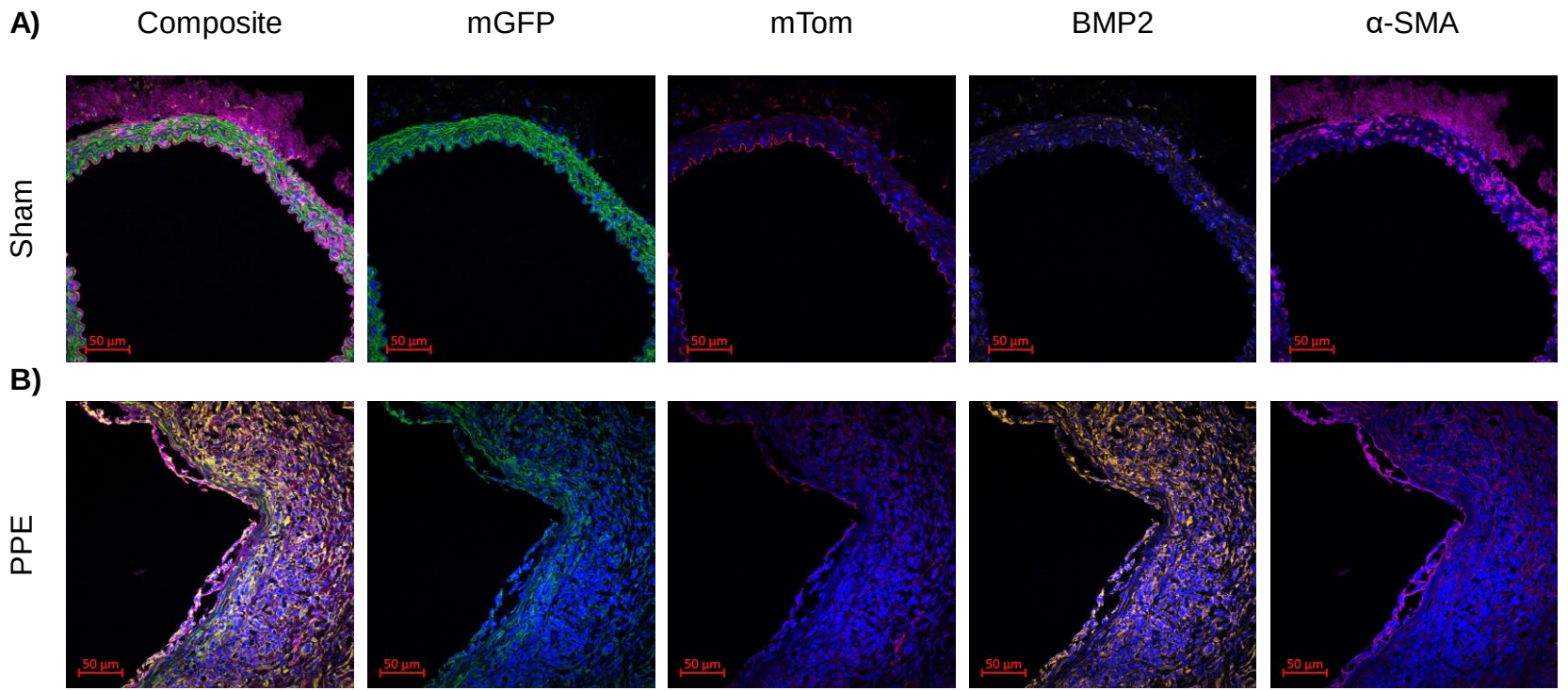

Figure 51: Representative 40x z-stack section of day 14 post surgery (A) sham and (B) PPE AAA tissue sections stained for BMP2 and α-SMA. Stains include mGFP = green (VSMC), mTom = red (all cells), DAPI = blue (nuclei), BMP2 = yellow (514), OPG = purple (647). n=3 sham, n=5 PPE

Counts for the number of DAPI positive nuclei and mGFP positive nuclei follow a similar pattern as described in Figures 48a and 48b respectively. Number of DAPI positive (Figure 52a) and mGFP positive nuclei (Figure 52b) increase in the PPE models at day 7 and 14 when compared to sham equivalents, suggesting positive aneurysm remodelling and cellular remodelling. Counts of mTom positive nuclei (Figure 52c) however do not follow a similar pattern as to that seen in Figure 48c. This could be due to a smaller number of slices quantified in this section due to the poor penetration of α-SMA antibody.

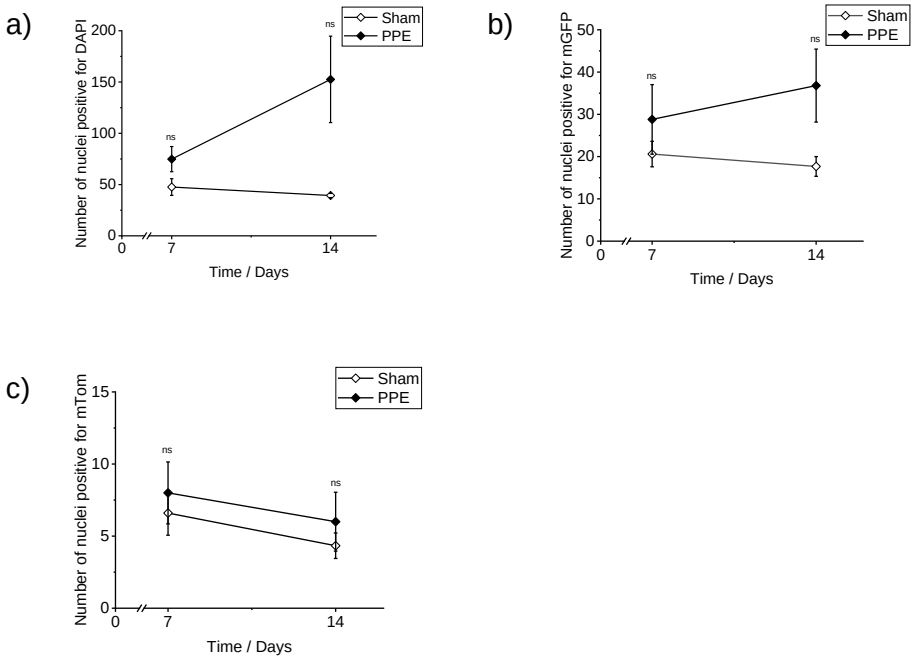

Figure 52: Raw counts of cells expressing DAPI, mGFP and mTom in sections stained for both BMP2 and α-SMA stained. Trends for (a) DAPI and (b) mGFP positive cells follow similar patterns to those seen in Figure 48. mTom counts follow a different trend as to that presented in Figure 48 due to a reduced number of slices available for analysis. Mean and standard error shown.

Nuclei positive for mGFP and α-SMA were also quantified to quality assure the samples used in this study are representative of results previously reported by our group. The percentage of cells expressing mGFP AND α-SMA decrease in PPE model at both day 7 and day 14 compared to sham model (Figure 53a). Table 17 shows the percentage of all cells positive for mGFP and α-SMA at day 7 and day 14. However, the recorded number of mGFP AND α-SMA positive cells is much lower in this study cohort compared to that previously reported. This

could be due to a different α-SMA antibody used to accommodate the allocation of secondary IF antibodies in this study.

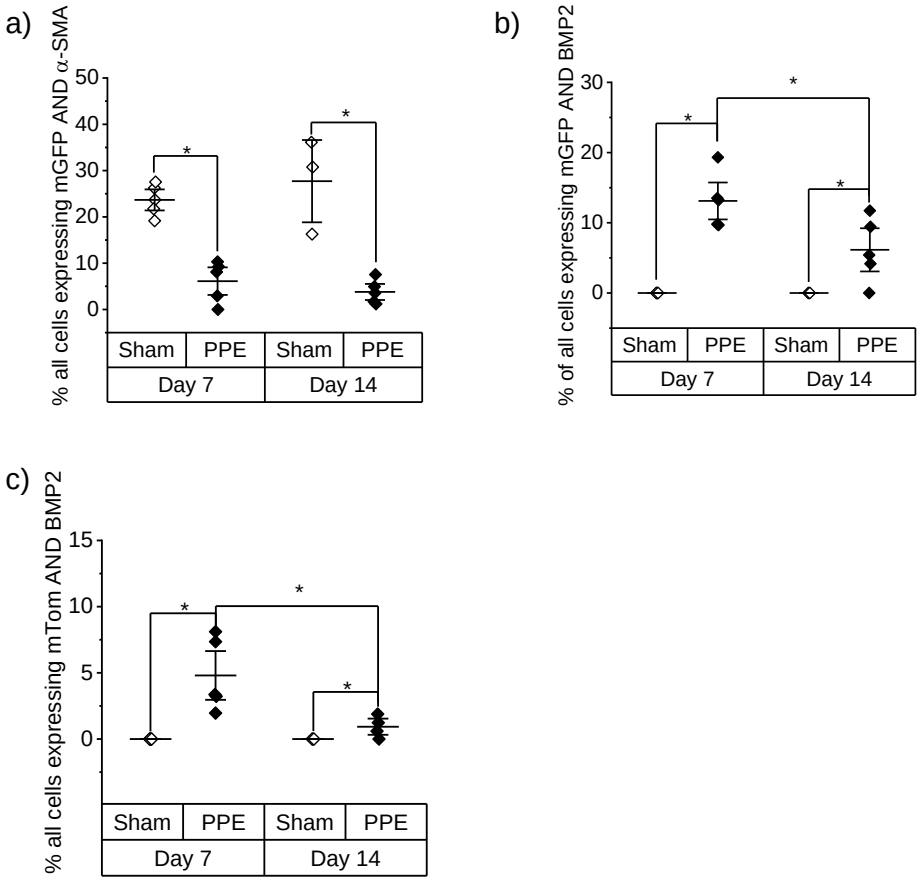

Figure 53: Cell counts for cells positive for mGFP AND α-SMA (a), mGFP AND BMP2 (b) and mTom AND BMP2 (c) as a percentage of all cells counted across slices. (p<0.05). Mean and standard error shown.

Table 17: Mean and SE of percentage of cells positive for mGFP AND α-SMA

Time course / days	Sham / %	PPE / %	P value
7	24 ± 1.5	6.1 ± 2.0	0.00011
14	28 ± 5.9	3.8 ± 1.2	0.001

Quantification of both cells positive for mGFP AND BMP2 and cells positive for mTom AND BMP2 follows the same trend as reported in Section 3.5.1 (Table 18 and 19 respectively). BMP2 expression in mGFP positive cells is highest in PPE model at day 7 compared to day 14 and sham equivalents (Figure 53b). In

addition, BMP2 expression in mTom positive cells is highest at day 7 compared to day 14 and sham equivalents (Figure 53c).

Table 18: Mean and standard error of percentage of cells positive for mGFP AND BMP2

Time course / days	Sham / %	PPE / %	P value
7	0	13± 1.8	0.05
14	0	6.1 ± 2.1	0.05

Table 19: Mean and standard error of percentage of cells positive for mTom AND BMP2

Time course / days	Sham / %	PPE / %	P value
7	0	4.8 ± 1.2	0.05
14	0	0.93 ± 0.41	0.05

As the majority of BMP2 staining was located in lineage traced VSMC we hypothesised that expression might relate to VSMC differentiation status. To assess this, BMP2 expression in lineage traced VSMC (mGFP+) cells with or without positive staining for α-SMA which is highly expressed in differentiated VMSC were quantified. Figure 54 shows quantification for mGFP AND BMP2 AND α-SMA cells vs mGFP AND BMP2 NOT α-SMA cells at day 7 and the mean and SE is tabulated in Table 20. A higher portion of cells counted for mGFP AND BMP2 NOT α-SMA compared to cells positive mGFP AND BMP2 AND α-SMA cells, however the differences in percentage counted at day 7 was not significantly different. Figure 55 shows the same quantification however on day 14 sham and PPE aortic sections. A similar trend is seen at day 14 compared to day 7, however a lower percentage of cells account for mGFP AND BMP2 AND α-SMA cells positivity and mGFP AND BMP2 NOT α-SMA cells (Table 21). The difference at day 14 is significant. This trend suggests that at day 14, BMP2 staining is predominately seen in de-differentiated lineage traced VSMC compared to differentiated lineage traced VSMC.

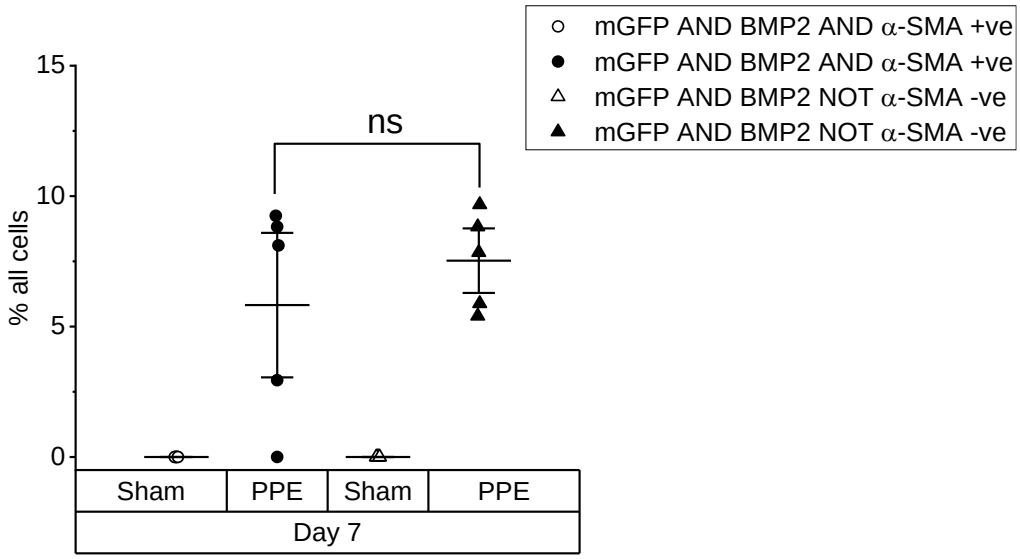

Figure 54: Cell counts for nuclei positive for mGFP and BMP2 with or without α-SMA positivity at day 7. Counts show that the percentage of cells positive for mGFP AND BMP2 AND α-SMA is high in the PPE model, as well as cells positive for mGFP AND BMP2 NOT α-SMA. However, a higher percentage of cells are positive for mGFP AND BMP2 NOT α-SMA, suggesting mGFP expressing BMP2 are differentiating, although this did not reach significance. ns, not significant. Mean and standard error shown.

Table 20: Mean and SE of percentage of cells positive for mGFP AND BMP2 with or without α-SMA positivity in day 7 sections.

Surgical Intervention	**α-**SMA positive / %	**α-**SMA negative/ %	P value
Sham	0	0	-
PPE	5.8 ± 1.8	7.5 ± 0.82	0.53

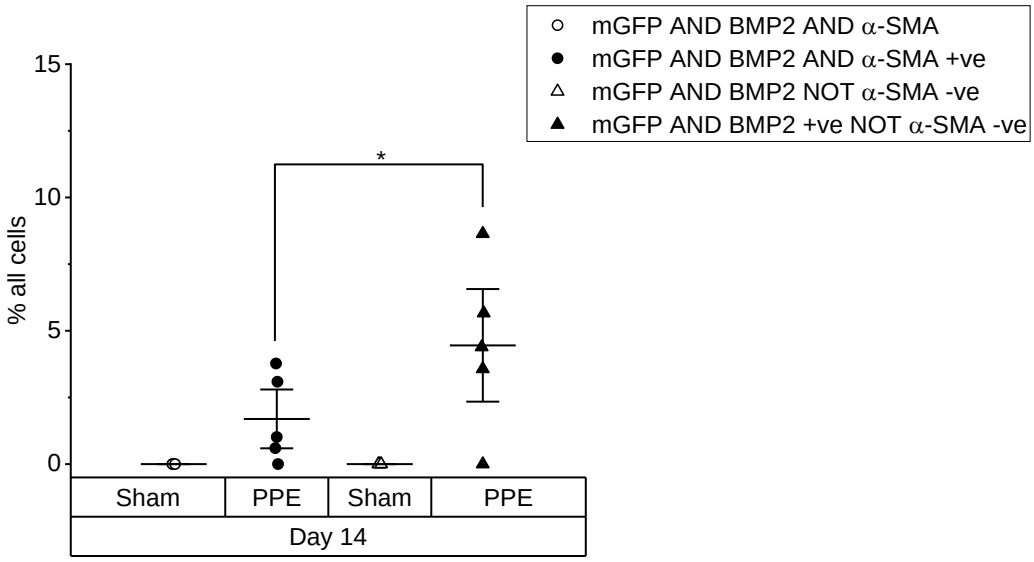

Figure 55: Cell counts for nuclei positive for mGFP and BMP2 with or without α-SMA positivity at day 14. Counts show that the percentage of cells positive for mGFP AND BMP2 AND α-SMA is high in the PPE model, as well as cells positive for mGFP AND BMP2 NOT α-SMA. However, a higher percentage of cells are positive for mGFP AND BMP2 NOT α-SMA, suggesting mGFP expressing BMP2 are differentiating. This occurs at a lower percentage when compared to day 7 (Figure 54). ($p<0.05$). Mean and standard error shown.

Table 21: Mean and SE of percentage of cells positive for mGFP AND BMP2 with or without α-SMA positivity in day 14 sections.

Surgical Intervention	**α-**SMA positive / %	**α-**SMA negative / %	P value
Sham	0	0	-
PPE	1.7 ± 0.73	4.5 ± 1.5	0.039

Peri-adventitial PPE induced AAA appears to promote BMP2 expression at day 7 and day 14 in cells positive for mGFP, a marker of VSMCs in this study. Interestingly, a higher number of cells that express mGFP AND BMP2 do not express α-SMA, a marker of smooth muscle contractility. This suggests that VSMC could be remodelling into an osteogenic like cell and contributing to the formation of microcalcifications.

3.5.3 Runx2 expression is detected in PPE AAA but not BMP4

As described in Section 1.6.2, Runx2 deletion in mice bearing an ApoE$^{-/-}$ background attenuated both Ang-II driven AAA and microcalcification development. Therefore it was important to investigate the expression of Runx2 in the PPE model. In addition, due to the increased expression of BMP2 seen in Section 3.5.1 and 3.5.2, BMP4 expression was investigated to study if any additional drivers of calcification can be detected in the PPE model of AAA.

Due to the results seen in Section 3.5.1, only baseline, day 7 and day 14 sections were imaged. Figure 56 demonstrates baseline sections stained for Runx2 and BMP4 demonstrated no visible positive staining. In day 7 sham sections (Figure 57), no positive nuclei was seen for Runx2 and BMP4. However in PPE aortic sections, the presence of Runx2 positive nuclei is visible but not BMP4 positive nuclei. No visible Runx2 or BMP4 staining was visibly seen in day 14 sham and PPE aortic sections (Figure 58).

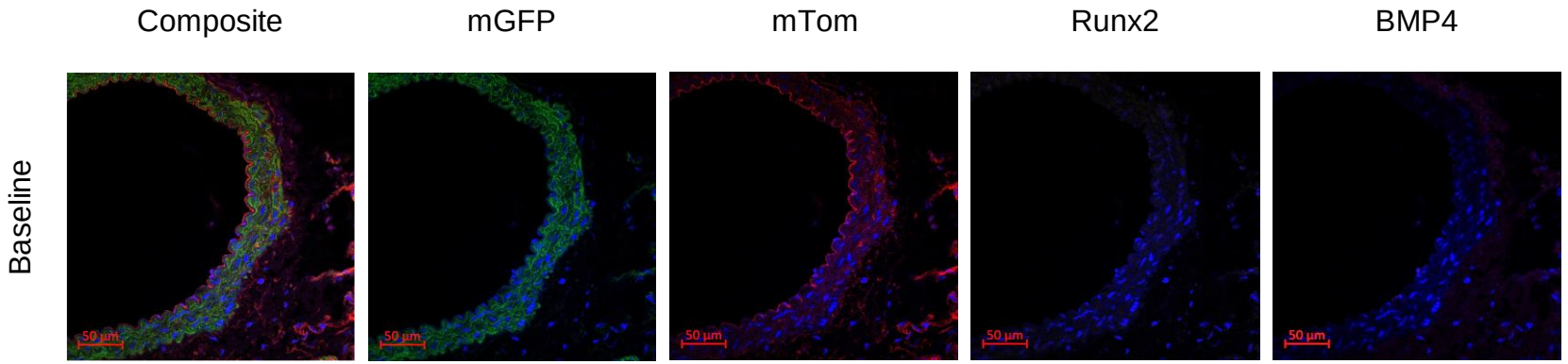

Figure 56: Representative 40x z-stack section of baseline mTmG AAA tissue sections stained for Runx2 and BMP4. Stains include mGFP = green (VSMC), mTom = red (all cells), DAPI = blue (nuclei), Runx2 = yellow (514), BMP4 = purple (647). n=4

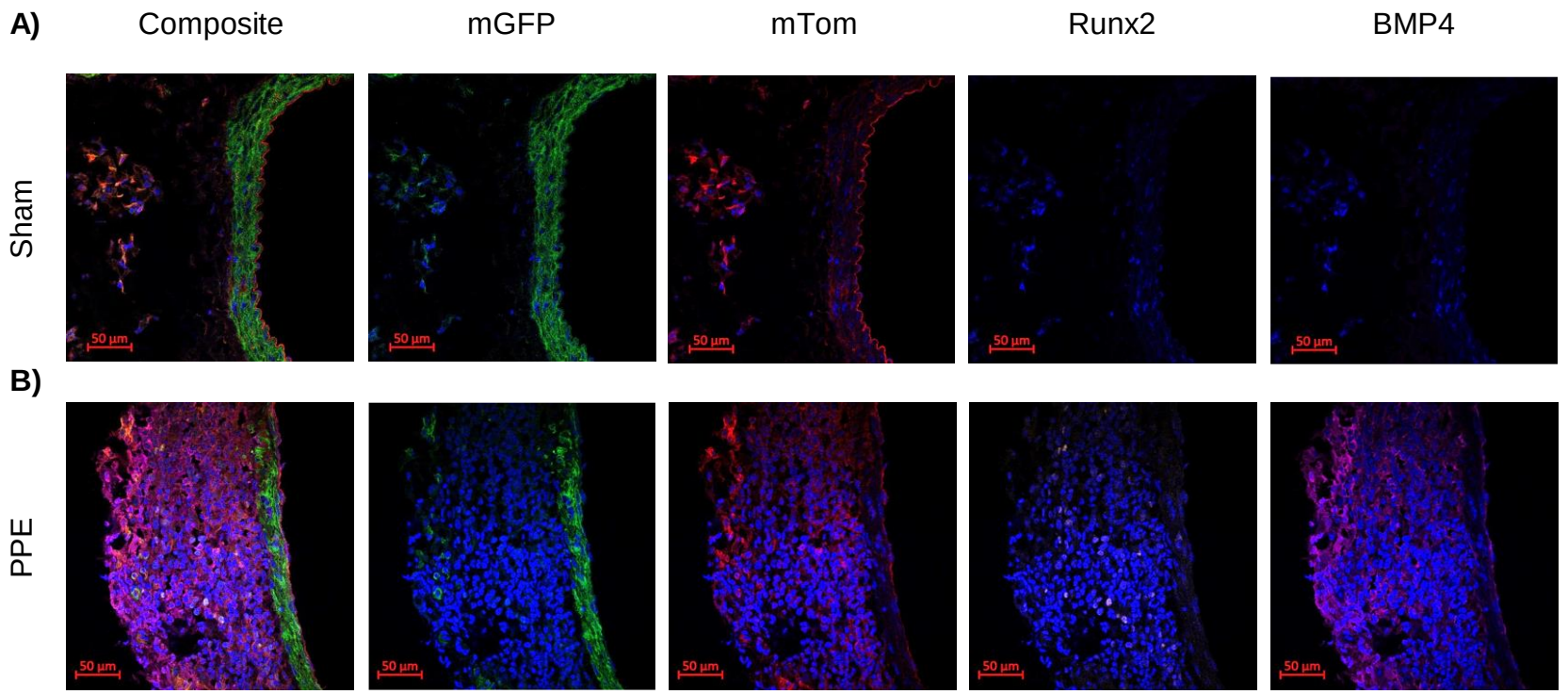

Figure 57: Representative 40x z-stack section of day 7 post surgery (A) sham and (B) PPE AAA tissue sections stained for Runx2 and BMP4. Stains include mGFP = green (VSMC), mTom = red (all cells), DAPI = blue (nuclei), BMP2 = yellow (514), OPG = purple (647). n=6 sham, n=5 PPE

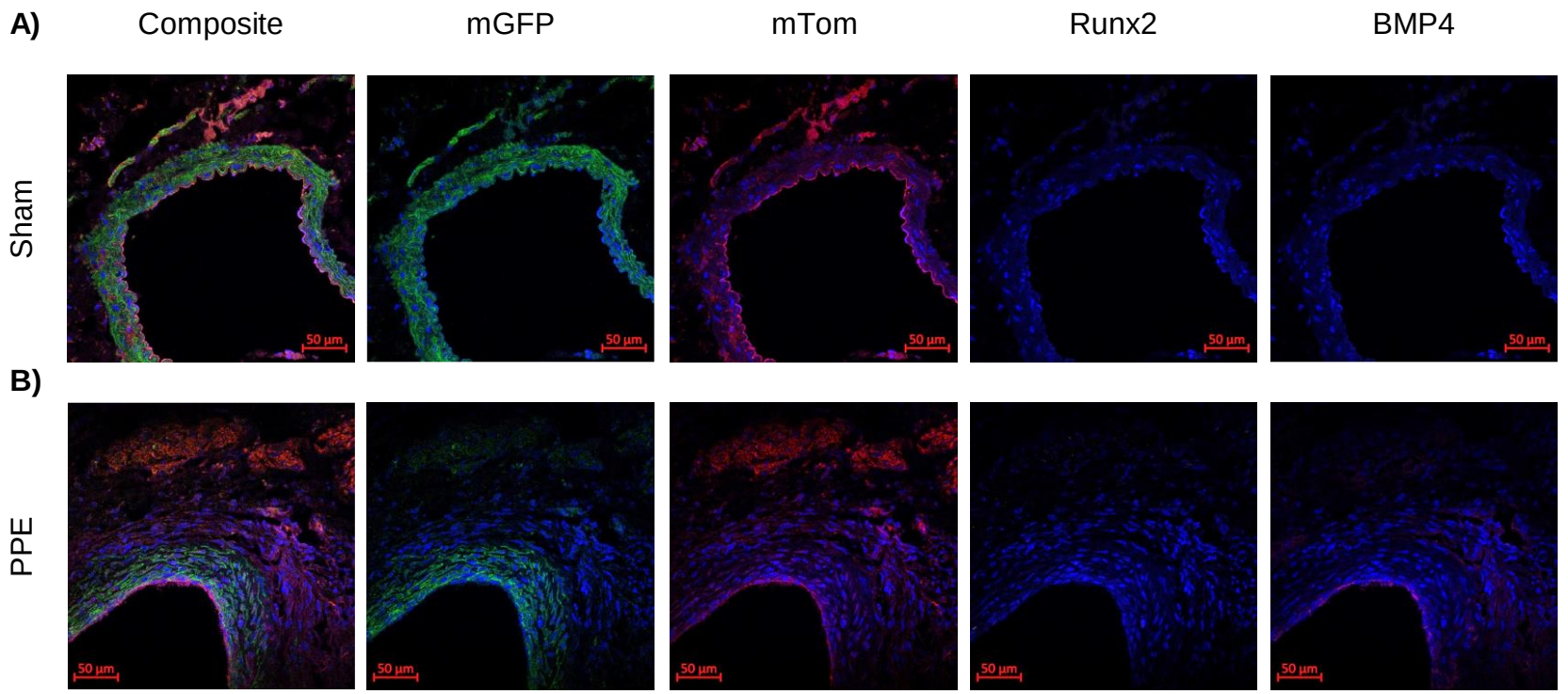

Figure 58: Representative 40x z-stack section of day 14 post surgery (A) sham and (B) PPE AAA tissue sections stained for Runx2 and BMP4. Stains include mGFP = green (VSMC), mTom = red (all cells), DAPI = blue (nuclei), BMP2 = yellow (514), OPG = purple (647). n=3 sham, n=7 PPE

Quantifying the number of mGFP positive for Runx2 or BMP4 in day 7 and day 14 sections showed no positive expression of either marker (Figure 59). However, a small percentage of cells positive for mTom AND Runx2 was seen in day 7 PPE aortic sections (Figure 59, Table 22), which was significantly different to sham aortic sections at the same time point. No positivity for mTom AND Runx2 cells at day 14 was seen in sham and PPE aortic sections. No cells positive for mTom AND BMP4 was seen in day 7 and day 14 aortic sections.

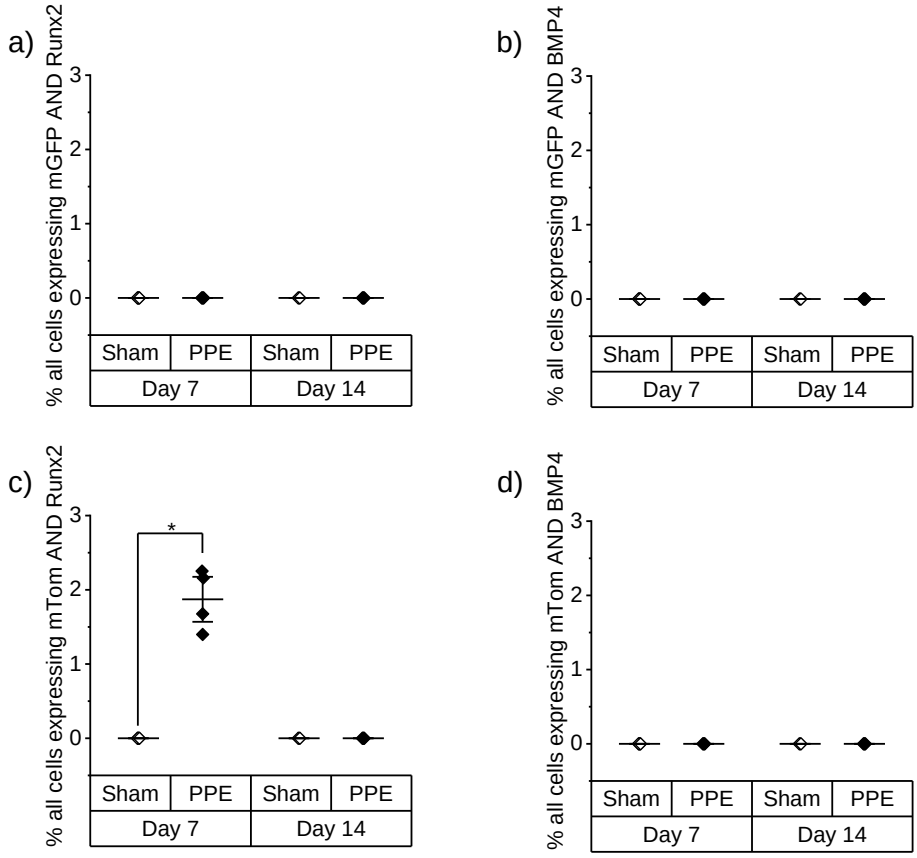

Figure 59: Percentage of cells expressing Runx2 and BMP4 in day 7 and day 14 sham and PPE tissue sections. (a) cell counts revealed no cells to be mGFP AND Runx2 positive. (b) no cells were mGFP AND BMP4 positive. (c) cells positive for mTom and Runx2 display high expression of Runx2 at day 7 in PPE sections. (d) no cells were positive for Runx2 AND BMP4. ($p<0.05$). Mean and standard error shown.

Table 22: Mean and standard error of percentage of cells positive for mTom AND Runx2

Time course / days	Sham / %	PPE / %	P value
7	0	1.9 ± 0.20	0.05
14	0	0	-

3.6 VSMC driven calcification *ex vivo*

The results from the mTmG study (Section 3.5) indicated that, in the PPE model, VMSCs expressed elevated levels of BMP2. This suggested that these VSMCs were de-differentiated, a state which is associated with a proliferative, migratory and secretary phenotype. VSMCs could therefore be displaying an osteogenic phenotype in AAA progression and may drive microcalcification development. As a result, it was important to study the expression of calcification markers *ex vivo* to support the findings from the *in vivo* data, to determine any drivers of microcalcification and to examine potential therapeutics that could be translated into murine models.

Initial experiments were first tested in saphenous vein smooth muscle cells (SVSMCs) to optimise conditions before translation into aortic smooth muscle cells.

3.6.1 Exposure of SVSMCs to aged calcification media

To determine the expression of BMP2, BMP4, Runx2, OPN and OPG in SVSMCs, these cells were exposed to an aged calcification media for 24 and 72 hours, and RNA was collected for qPCR analysis (Figure 60 and 61, respectively, mean and standard error in Table 23 and 24). The expression of a-SMA (ACTA2) was also studied as a control measure. qPCR analysis demonstrated inconsistent and variable expression of BMP2 (Figure 60a), BMP4 (Figure 60b), Runx2 (Figure 60c), OPN (Figure 61a), OPG (Figure 61b) and ACTA2 (Figure 61c) in control and treated cells. This suggested that SVSMCs exposed to aged calcification media did not upregulate these calcification markers.

BMP2 (Figure 62a) and OPN (Figure 62b) ELISA were also conducted on media collected from cells treated for 72 hours with calcification media to determine if

BMP2 and OPN were secreted from these cells. Mean and standard error is shown in Table 25. Figure 62a shows no difference between control and treated cells in BMP2 expression and Figure 62b displays no difference between control and treated cells in OPN expression.

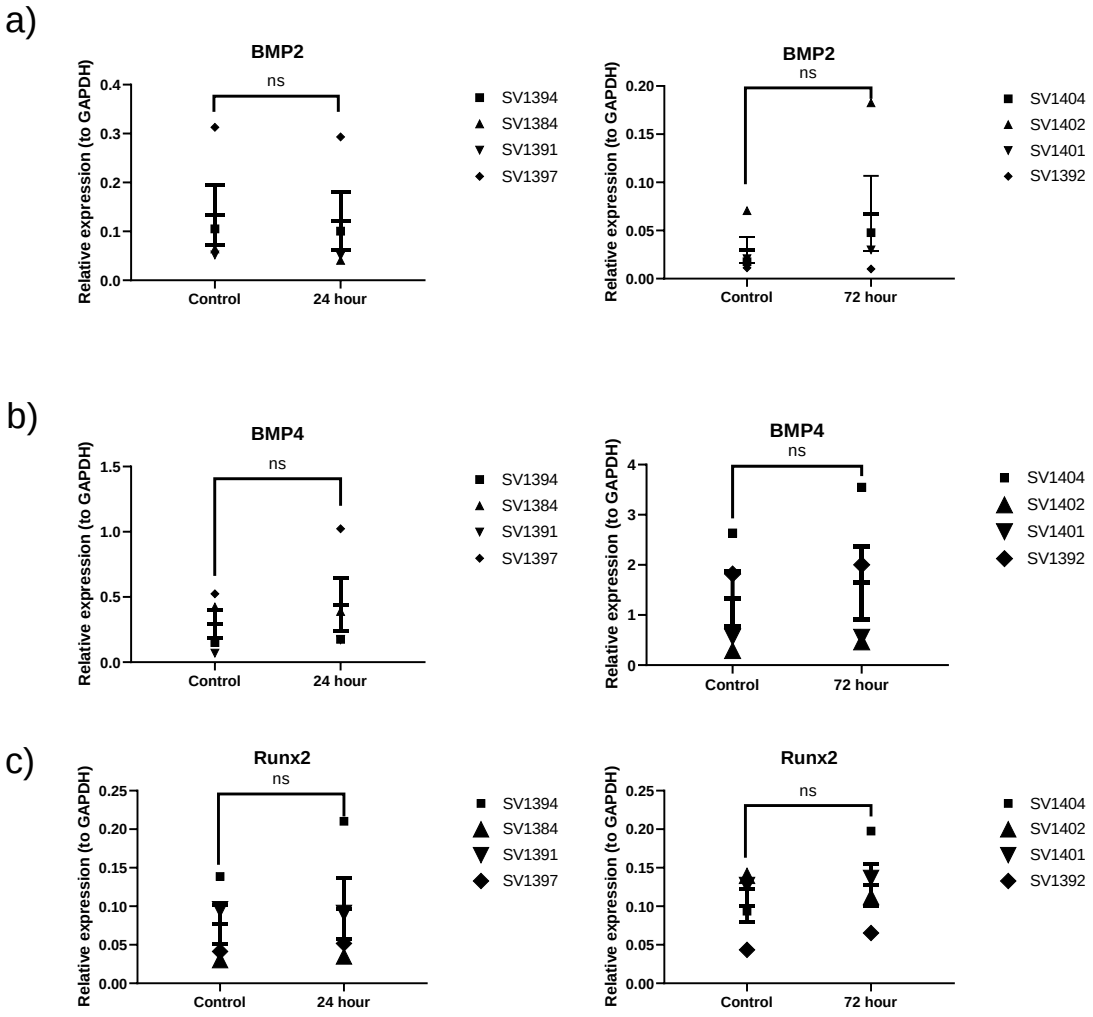

Figure 60: PCR analysis of calcification markers from 24 hour and 72 hour calcification challenged cells. No difference in (a) BMP2, (b) BMP4 and (c) Runx2 expression is seen between control and cells exposed to calcification media for 24 hours or 72 hours. Relative expression measured against GAPDH. n=4, ns= not significant. Mean and standard error shown.

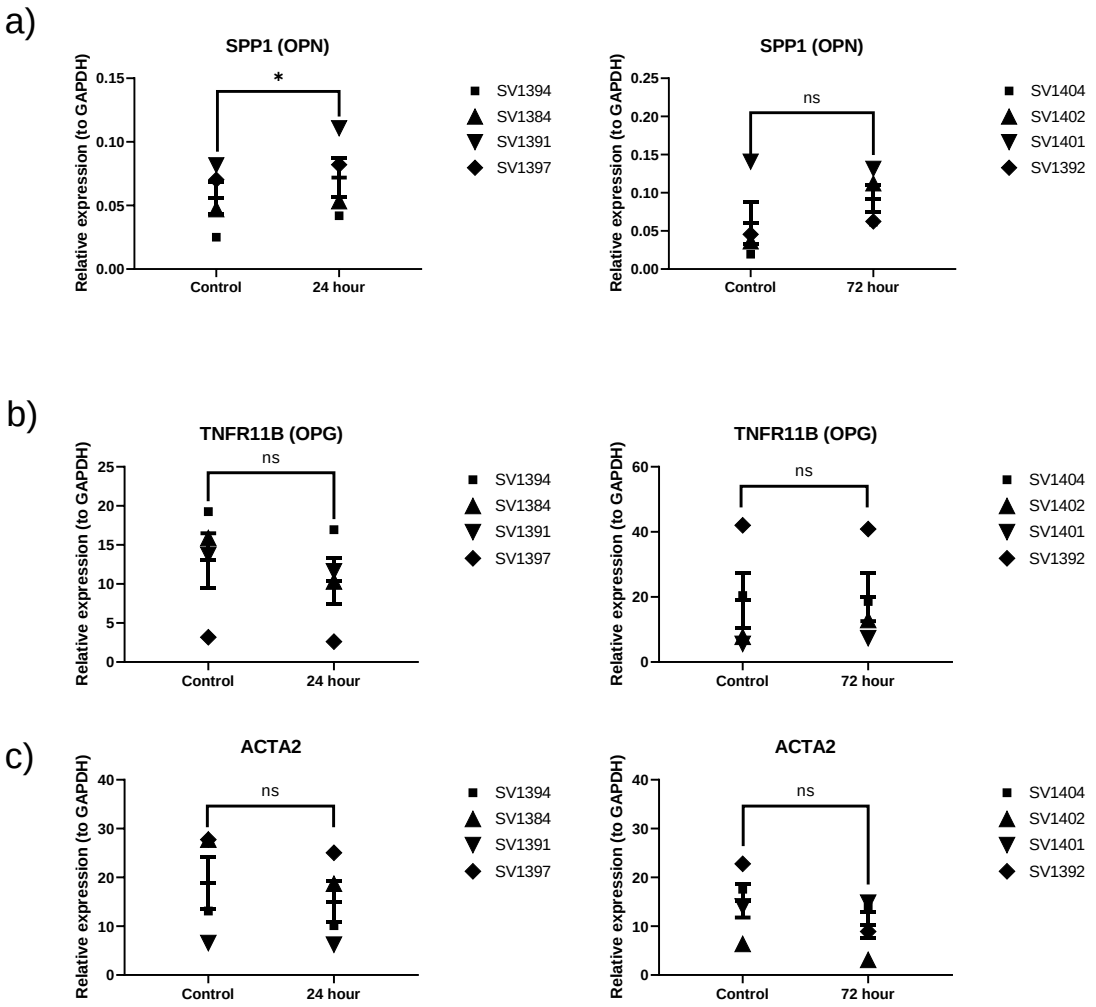

Figure 61: PCR analysis of calcification markers from 24 hour and 72 hour calcification challenged cells. No difference in (a) *SPP1* (OPN), (b) *TNFR11B* (OPG) and (c) ACTA2 expression is seen between control and cells exposed to calcification media for 24 hours or 72 hours. Relative expression measured against GAPDH. n=4, ns= not significant, $p<0.05$. Mean and standard error shown.

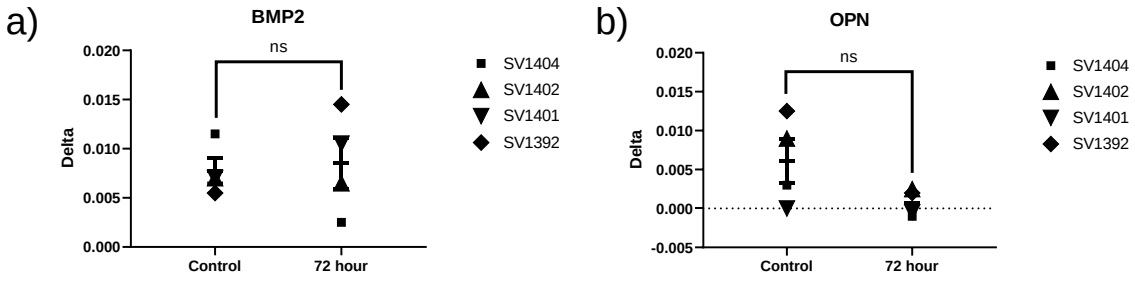

Figure 62: ELISA of 72 hour calcification challenged SVSMC. No difference in (a) BMP2 and (b) OPN expression in serum is seen between control and cells exposed to calcification media for 72 hours. n=4, ns = not significant. Mean and standard error shown.

Table 23: Mean and standard error of qPCR values for expression of calcification markers in SVSMC exposed for 24 hours to growth media vs calcification media, relative to GAPDH

Gene	Control (growth media)	Calcification media	P value
BMP2	0.13 ± 0.061	0.121 ± 0.059	0.10
BMP4	0.292 ± 0.108	0.44 ± 0.201	0.31
Runx2	0.077 ± 0.025	0.097 ± 0.04	0.32
SPP1 (OPN)	0.056 ± 0.013	0.072 ± 0.015	0.04
TNFR11B (OPG)	13.010 ± 3.470	10.374 ± 2.960	0.08
ACTA2	18.790 ± 5.537	15.025 ± 4.246	0.13

Table 24: Mean and standard error of qPCR values for expression of calcification markers in SVSMC exposed for 72 hours to growth media vs calcification media, relative to GAPDH

Gene	Control (growth media)	Calcification media	P value
BMP2	0.030 ± 0.014	0.68 ± 0.039	0.24
BMP4	1.327 ± 0.548	1.642 ± 0.726	0.21
Runx2	0.101 ± 0.022	0.128 ± 0.028	0.40
SPP1 (OPN)	0.061 ± 0.027	0.092 ± 0.018	0.18
TNFR11B (OPG)	18.942 ± 8.366	19.949 ± 7.353	0.56
ACTA2	15.212 ± 3.442	10.195 ± 2.690	0.20

Table 25: Mean and standard error of ELISA values for expression of calcification markers in SVSMC exposed for 72 hours to growth media vs calcification media

Gene	Control (growth media)	Calcification media	P value
BMP2	0.008 ± 0.001	0.009 ± 0.003	0.85
OPN	0.006 ± 0.003	0.001 ± 0.001	0.08

3.6.2 PDGF-BB driven remodelling of SVSMC

Our group has developed and validated a Sm22CrePDGF murine model. The VSMCs overexpress PDGFb, which promotes aortic dilation from birth. USS and CTA analysis of these vessels demonstrate stiffness and thus suggest PDGF driven aortic formation could also involve the formation of calcification deposits in

the aortic wall. Therefore, SVSMCs were exposed to PDGF-BB, a synthetic analogue, to determine if there was any change in expression of calcification markers (as discussed in Section 1.6.2) and ACTA2.

RNA was harvested from cells exposed PDGF-BB (10 ng/mL) and analysed for relative change in calcification marker expression using qPCR. Similar to the results in Section 6.2, inconsistent and variable expression of BMP2 (Figure 63a), BMP4 (Figure 63b), Runx2 (Figure 63c), OPN (Figure 63d), OPG (Figure 63e) and ACTA2 (Figure 63f) in control and treated cells was recorded (mean and standard error displayed Table 26). In addition, BMP2 and OPN ELISA (Figure 64) experiments were carried out on media from control and PDGF-BB treated cells (mean and standard error in Table 27). ELISA results demonstrated no significant difference between control and treated cells for both BMP2 and OPN expression.

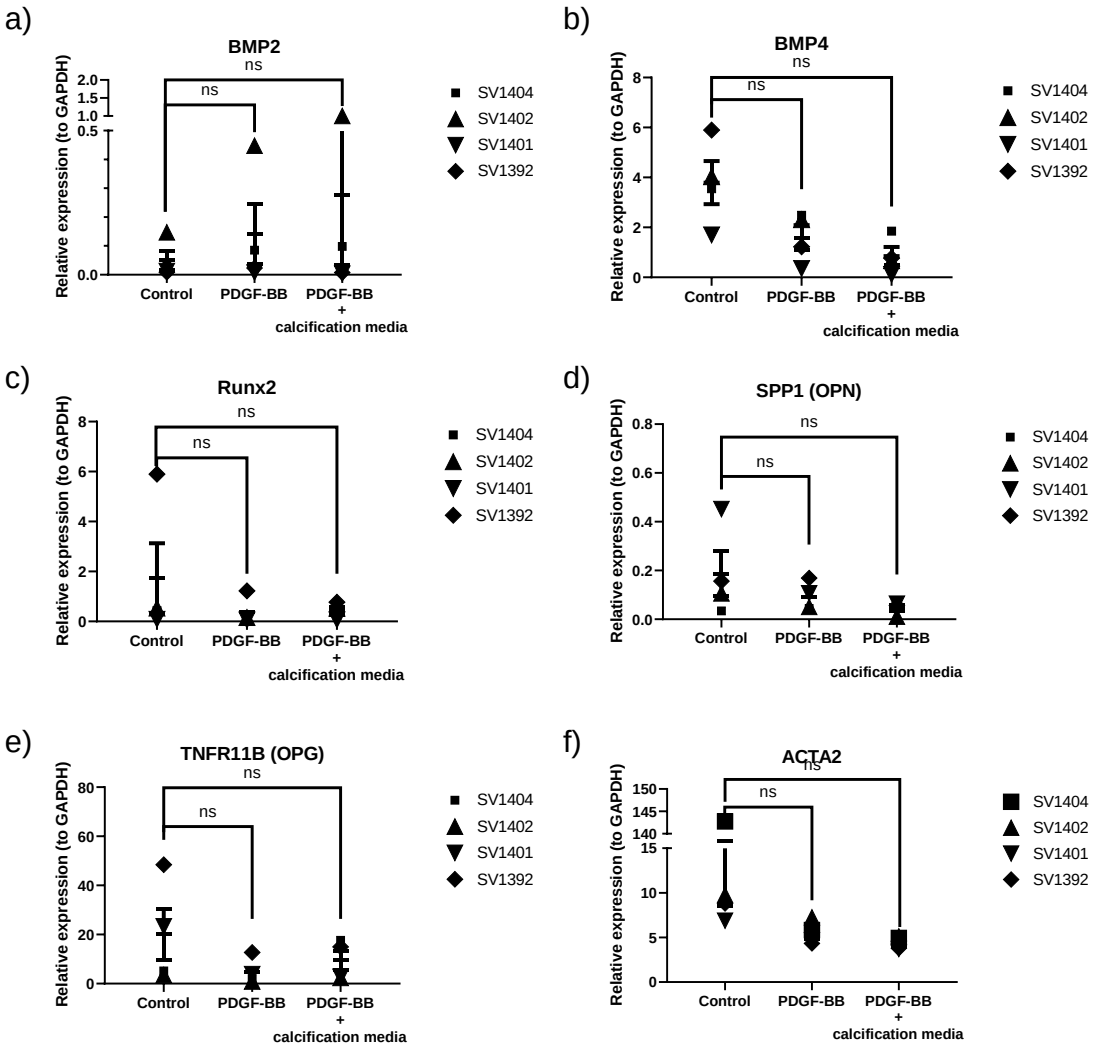

Figure 63: qPCR analysis of calcification markers from SVSMCs treated with either PDGF-BB 10 ng/mL or PDGF-BB 10 ng/mL and calcification media . The relative expressions of (a) BMP2, (b) BMP4 and (c) Runx2, (d) *SPP1* (OPN), (e) *TNFR11B* (OPG) and (f) ACTA2 were analysed against GAPDH. n=4, ns= not significant. Mean and standard error shown.

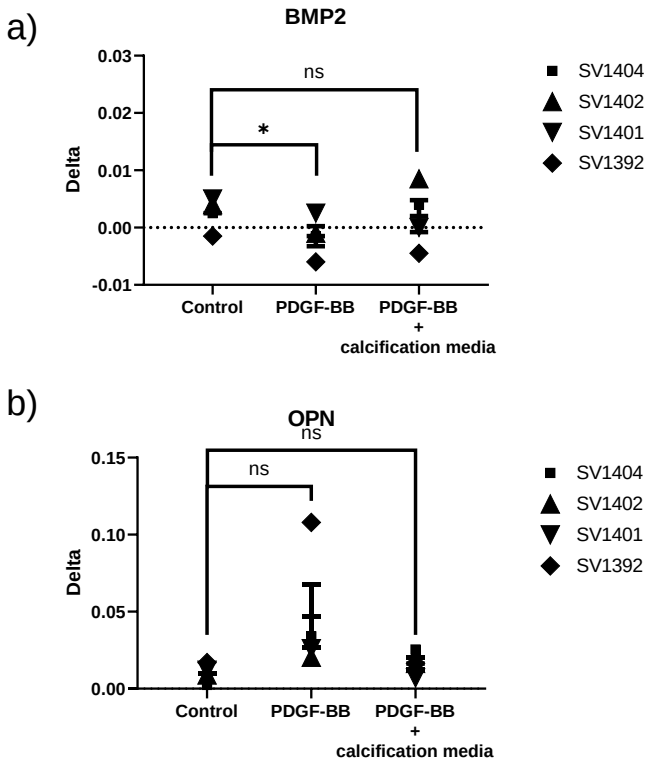

Figure 64: ELISA of PDGF-BB (10ng/mL) and PDGF-BB (10ng/mL) + Calcification media challenged SVSMC. No difference in (a) BMP2 and (b) OPN expression in serum is seen between control and cells exposed to PDGF-BB and PDGF-BB + calcification media. n=4, ns = not significant. Mean and standard error shown.

Table 26: Mean and standard error of qPCR values for expression of calcification markers in SVSMC exposed to PDGF-BB (10 ng/mL) or PDGF-BB (10 ng/mL) and calcification media, relative to GAPDH. P values shown are between control and intervention

Gene	Control	PDGF-BB	P value	PDGF-BB + Calcification media	P value
BMP2	0.050 ± 0.033	0.141± 0.104	0.28	0.272 ± 0.42	0.35
BMP4	3.793 ± 0.864	1.590 ± 0.499	0.35	0.851 ± 0.363	0.34
Runx2	1.737 ± 1.391	0.395 ± 0.276	0.31	0.405 ± 0.155	0.37
SPP1 (OPN)	0.187 ± 0.092	0.082 ± 0.029	0.34	0.046 ± 0.012	0.20
TNFR11B (OPG)	20.080 ± 10.452	4.796 ± 2.686	0.14	9.435 ± 3.997	0.37
ACTA2	42.045 ± 33.568	5.526 ± 0.661	0.35	4.4 ± 0.375	0.34

Table 27 Mean and standard error of ELISA values for expression of calcification markers in SVSMC exposed to PDGF-BB (10 ng/mL) or PDGF-BB (10 ng/mL) and calcification media. P values shown are between control and intervention

Gene	Control	PDGF-BB	P value	PDGF-BB + Calcification media	P value
BMP2	0.003 ± 0.001	-0.002 ± 0.002	0.005	0.002 ± 0.003	0.83
OPN	0.010 ± 0.003	0.047 ± 0.020	0.14	0.016 ± 0.004	0.38

3.7 Conclusion

No difference in Na[^{18}F]F detection of microcalcifications using PET/CT was seen in sham and PPE models. *Ex vivo* gamma counting of PPE induced AAA showed elevated Na[^{18}F]F uptake at day 14 post surgery when compared to sham equivalents. Von kossa stain also revealed the presence of microcalcification deposits in the aortic wall at day 14 post PPE surgery. Using the lineage traced model, nuclei positive for mGFP (lineage traced VSMC) and BMP2 was highest at day 7 post surgery in the PPE model, although still elevated at day 14. This suggests that in the PPE model, VSMC remodelling could be a contributor to microcalcification developments in the aortic wall and aneurysm development.

Chapter 4
Discussion

The aim of this PhD project was to i) evaluate the use of Na[^{18}F]F as a detector of AAA and AAA progression in a preclinical model, ii) determine the key markers of calcification involved in AAA progression in the PPE model and the specific cell type expressing osteogenic proteins and iii) investigate the application of novel reconstruction methods and assess the effects of different region of interest (ROI) definitions. It is worth noting that, due to the COVID-19 pandemic, many experimental plans made to achieve these aims could not be completed as a result of laboratory closure, and limited laboratory and resource access upon reopening.

Studying the development of microcalcification using nuclear imaging in both the $CaCl_2$ and peri-adventitial PPE models produced mixed results. Using Na[^{18}F]F in $CaCl_2$-treated mice provided some insight into AAA development when TBR_{max} and gamma counting data were assessed. However, aneurysm generation with this model was poor and analysis of AAA was hampered by signal masking by the vertebrae. In the PPE model, no detectable Na[^{18}F]F signal was apparent when compared to sham in PET/CT studies. By contrast, *ex vivo* experiments gave some interesting data, with biodistribution studies showing Na[^{18}F]F uptake in PPE AA when compared to sham operated tissue. In addition, BMP2, a marker of microcalcification development, was upregulated in PPE aortic tissue and located in both contractile and synthetic VSMCs.

4.1 PET/CT detection of microcalcification in preclinical models of AAA using Na[^{18}F]F

Na[^{18}F]F has been employed in the clinic to detect microcalcification development in atherosclerosis subjects. The SoFIA^3 trial demonstrated the potential use in AAA subjects, reporting that Na[^{18}F]F uptake could predict aneurysm growth and end clinical events (e.g. rupture) independent of clinical risk factors (e.g. smoking) (83). In the literature, little is reported on the use of Na[^{18}F]F in preclinical AAA. A single study reported microcalcification detection in Ang-II model of AAA (151). In the study, elevated Na[^{18}F]F signal was detected at three time points in the Ang-II model, compared to sham equivalents, with the presence of

microcalcifications seen in the suprarenal aneurysm. To our knowledge, this is the only study to report on the findings of Na[^{18}F]F detection in the PPE preclinical model of AAA.

In this thesis, both the $CaCl_2$ and PPE models were used to determine if Na[^{18}F]F uptake in microcalcifications located in the AA was achievable on the PET/CT system housed at the University of Leeds. The results in both models demonstrated the difficulty in detecting a uniform signal in the AA, as well as showing that any detectable signal from the AA is potentially masked by signal from the neighbouring spine. Quantifying the Na[^{18}F]F uptake in the AA showed no significant difference between the different metrics, apart from TBR_{max} in $CaCl_2$ model. It should be noted that several factors can confound quantification of SUV_{max}. These include tracer administration, scan time, final radiation dose and noise, and they can result in challenging interpretation of PET/CT studies.

In vascular PET/CT studies, there is lack of consensus about which PET/CT metric best represents the signal located in microcalcification deposits (183). SUV_{max}, for example, relies on uniform tracer distribution in the deposit and clear segmentation is required. In addition, the methodology in reconstructing the PET/CT data is considered, with the number of iterations used can influence SUV_{max} in terms of noise (225). TBR_{max} is often employed to remove some of the errors incorporated into by SUV_{max} quantification by removing background Na[^{18}F]F signal. The removal of Na[^{18}F]F background signal could enhance the detection of Na[^{18}F]F signal in the $CaCl_2$ model presented in this study. This is supported by the presence of detectable Na[^{18}F]F signal in *ex vivo* gamma counting of aortic tissue, as shown in Figure 24. In addition, line profile analysis through the abdominal aorta in $CaCl_2$ examples show possible signal masked by the spine, which is absent in baseline and sham line profiles. However, in the PPE model, no difference in each metric used in this study showed any significant difference between sham and PPE models at two time points.

In this thesis, positive Na[^{18}F]F detection in the PPE model was detected at day 14 using *ex vivo* gamma counting, with microcalcification deposits present in the aortic wall through positive Von Kossa stain. However, no positive Na[^{18}F]F signal was seen in the AA using the PET/CT system. Although there could be partial volume effects due to the signal from the spine masking the signal from the AA, absence of signal could be due to limitations with the scanner. The Albira

PET/SPECT/CT system, when compared to other commercial scanners, has a low sensitivity (2% compared to 6.7% for Siemens Inveon scanner) and a spatial resolution of 1.55 mm, the largest reported when compared to a range of scanners (226,227). Using both USS and CTA, sham operated aorta was measured at 0.52 ± 0.018 mm on USS and 0.71 ± 0.029 mm on CTA, whereas PPE operated aorta was measured at 1.0 ± 0.061 mm on USS and 1.2 ± 0.049 mm on CTA. The measured range of aorta in this study sits just below the spatial resolution of the scanner. This coupled with the low sensitivity could provide a barrier for detecting Na[^{18}F]F in this model using this preclinical scanner. It is therefore important to determine if the results from this study are reliable by replicating our experiments but with use of a different PET/CT scanner, or scanning the aorta *ex vivo* (228).

It should also be considered the role in which PPE model and Ang-II model reflect human clinical AAA progression. As previously mentioned, a study of Ang-II driven AAA formation detected microcalcification deposits at three different time points (151). In contrast, in the PPE model, microcalcifications was detected at day 14 i.e., end stage progression for this preclinical model. A recent study compared the PPE and Ang-II models to human AAA development using genomic profiling and demonstrated that the PPE model reflects disease initiation, whereas Ang-II model captures AAA progression (229). This reflects the appearance of microcalcifications detected by Na[^{18}F]F in late stage AAA patients (83). Therefore, the PPE model may not be the most appropriate model to study microcalcification development in comparison to other models. It is important to note, however, that there is evidence in this study from PPE-treated mice demonstrating the expression of calcification markers in the remodelling aortic wall, suggesting the model may still be relevant for investigating microcalcifications in AAA.

4.2 Advanced Reconstruction algorithms on PET/CT data

The development of advanced reconstruction algorithms have been a key development in research to improve image quality and increase the speed to enable faster diagnosis in the clinic. The kernel expectation maximum methods were first introduced to solve a common issue in PET imaging; the acquisition of low count data resulting in noisy image reconstruction (230). The kernel expectation maximum method utilises prior information from the PET

reconstruction to improve image quality, whilst the hybrid kernel method uses additional imaging data set i.e. CT or MR data to improve image resolution. The kernel expectation maximum and hybrid kernel expectation maximum method have been studied on both preclinical and clinical Na[^{18}F]F PET data to improve image quantification. Application of the aforementioned advanced reconstruction methods in Na[^{18}F]F carotid artery rabbit scans reduced partial volume effects as well as providing improved delineation of the artery for quantification (231). Application of these methods in the SoFIA^{3} trial data set improved quantification of microcalcification deposits in the aorta and revealed additional positive AAA diagnosis (221).

Due to the difficulty in positively identifying Na[^{18}F]F signal in the PPE model, and the partial volume effects exhibited by the spine in both the $CaCl_2$ and PPE models, the kernel methods were implemented. As shown in the line profiles in Figures 37–40, no improvement in identifying signal from the AA was seen for any of the models tested. This suggests that there could be a lack of PET information for the AA to allow for improved delineation. In addition, no quantification metrics were studied due to the development stage of implementing the Albira scanner into the STIR database. The lack of improvement in data quality could also be due to low sensitivity of the Albira scanner (227). However, it should be noted that the vertebrae peak in the line profiles due to signal from the spine is well preserved in the STIR reconstructions, with KEM and HKEM generating smoother profiles.

The absence of additional Na[^{18}F]F information generated from the advanced reconstruction algorithms for the abdominal aorta, in particular in the PPE model, does not fully support the *ex vivo* gamma counting results presented in this study. As mentioned in Section 4.1, additional scanners should be tested to see if there is true Na[^{18}F]F detectable by PET/CT in this model. However additional advanced reconstruction algorithms could be tested to determine if there is true signal from the AA. Segmentation of the spine has been shown to visually improve the identification of microcalcification lesions as detected by positive Na[^{18}F]F in the Ang-II model and SoFIA^{3} trial data (151,224). These methods however was not considered for this study due to the quality of CT data acquired and the hypothesis that the kernel methods should improve the visualisation of microcalcifications in the abdominal aorta.

4.3 Animal PET/CT preclinical protocol

In the clinic, there is a clear protocol for subjects undergoing a PET/CT scan. For example, subjects undergoing a 2-[^{18}F]-FDG will be asked to fast for 6 hours prior to their scan to reduce the effects of basal glucose levels. There has been discussion in the preclinical PET/CT community into the need for a murine PET/CT protocol to remove confounds seen in the literature. A large multicentre study (n=5) imaged a phantom of known radioactivity on 5 different preclinical PET/CT scans using the centre specific reconstruction parameters (232). The phantom was then rescanned using a study derived protocol. The findings from the multicentre study showed that site specific measures of SUV_{max} were confounded by bias whereas using the study derived parameters, SUV_{max} measurements improved. Similar findings were also found for recovery coefficients. Therefore, there could be the need for standardized protocols in preclinical PET/CT.

In the PET/CT studies presented in this study, radioactivity, at a known concentration was either injected at the start of the scan or injected in models which subsequently recovered for a later scan time. In the Ang-II AAA study of microcalcification, models were injected at the same target radioactivity (10 MBq) however were left for 10 minutes before being placed under isoflurane and in the scanner (151). There is however, no information on scan duration or time frame for analysing the presence of microcalcifications. In addition, OSEM reconstruction was used whereas on the Albira system, only MLEM reconstruction was available. However, this difference shouldn't be too large as OSEM is an accelerated version of MLEM. Although the difference in scan parameters is not large, small variations in preparation could be important in the detection of microcalcifications using Na[^{18}F]F in preclinical models of AAA. In addition, there will be variations in injection quality, animal preparation (i.e. fast or no fast), animal positioning in the scanner and scanner capabilities.

4.4 Markers of microcalcification in AAA mTmG tissue

The mTmG lineage tracing model is a powerful tool to assess the fate of specific cell types and to learn about how tissue remodels in response to disease. Investigation of the expression of various calcification markers was conducted on sections of aortic mTmG tissue to determine the cells involved in remodelling.

BMP2, BMP4 and Runx2 were examined as they are responsible for driving calcification remodelling. OPN and OPG were chosen due to their role in regulating calcification production. Both OPN and OPG have been reported in histological examination of human end stage AAA tissue, and have been suggested as biomarkers to identify AAA patients developing microcalcification deposits.

To our knowledge, this is the first reporting of microcalcification deposits in the PPE preclinical murine model of AAA. Von Kossa stain (Figure 22) showed the presence of microcalcifications in the aortic wall. Figures 44, 45 and 49 demonstrate the detection of BMP2 in lineage traced VSMC in PPE operated murine models. The peri-adventitial application of PPE on the aorta causes destruction of the vessel wall and induces inflammation and VSMC remodelling. This appears to induce microcalcification and the data presented in Section 3.5 supports the idea that this occurs in de-differentiated VSMC. The link between elastin proteins and microcalcifications has been studied previously. In the CaCl2 model of AAA, the formation of microcalcification deposits was accompanied by the breakdown of the elastin wall (233). The link between the two biological processes was attributed to the elevated levels of MMPs, with MMP-2 and MMP-9 KO mice were resistant to CaCl2 induced AAA and microcalcification development. *Ex vivo* rat aortic smooth muscle cells (RASMCs) exposed to a pro-calcification matrix were remodelled into an osteogenic phenotype (234). The osteogenic phenotype, however, could be reversed when exposed to a non-calcified matrix suggesting a calcified matrix may be required to promote VSMC dedifferentiation. Finally the elevation of elastin peptides and TGF-β1, promoted RASMCs dedifferentiation into an osteogenic state when incubated with a mix of elastin peptides through upregulation of calcification markers such as Runx2, ALP and osteocalcin (235). It is therefore warranted to study the biological process that promotes microcalcification deposits through the application of PPE.

The expression of BMP2 in PPE aortic sections was found in cells expressing mGFP (i.e. lineage traced VSMCs) with or without the expression of α-SMA, a smooth muscle cell marker. The upregulation of BMP2 can be attributed to the onset of disease, as BMP2 expression is not detected in sham sections (along with other markers of calcification studied). This suggests that VSMCs

remodelling could be important in driving microcalcification development in aneurysm progression. The biological source of microcalcifications in human AAA has not been previously identified. However, it has been suggested previously that VSMC can differentiated into osteogenic like cells when transitioning from a contractile to synthetic state. A review study looking at single cells RNA sequencing studies demonstrated that VSMC transition from a contractile state to an intermediatory mesenchymal cell state before developing into an osteogenic state (236). This has been suggested to be a result of Runx2 and BMP2 stimulating this process and a loss of contractile proteins. This has been seen in this study, with VSMC losing contractile state (i.e. downregulation of α-SMA as a result of PPE induced injury) and upregulation of BMP2. It should be noted that the presence of BMP2 in cells expressing mTom could also suggest that microcalcification development in PPE model could be a multicell process and this should be investigated further. The majority of BMP2 expression was localised in lineage traced VSMC thus indicating the role VSMC remodelling could play in AAA progression and microcalcification development.

In this study, other markers of calcification were also studied including Runx2, BMP4, OPG and OPN. Out of the markers investigated only Runx2 expression was detected. Runx2 was investigated primarily due to mice harbouring a Runx2 deficient background were resistant to Ang-II driven AAA formation (151). Figure 59 demonstrates a small percentage of cells expressing both mTom and Runx2. The small, reported percentage could be due to the difficulty of detecting transcription factors using IF antibodies. An alternative method, such as western blot of RT-PCR may identify a greater expression of Runx2, in both VSMC and other cell types in PPE induced AAA tissue. In addition, IF investigation of BMP4 and OPG was absent from the tissue sections investigated in this study. This however, does not rule out BMP4 and OPG are upregulated in PPE induced AAA progression. The expression levels could be low and therefore IF may not be the most appropriate methodology to investigate upregulation of these markers, if any. In addition, both of these markers were investigated using a 647 secondary antibody. Detection of antibodies using 647 antibodies test the range of the confocal microscope and is not the most ideal channel to use. Although the mTmG model is an elegant IF tool to lineage trace the fate of cells, the membrane fluorescent markers occupy the ideal fluorescent channels used in IF. To study

the presence of both BMP4 and OPG, secondary antibodies in a different IF range could be used, or detecting these markers using western blot of RT-PCR. It would be interesting to investigate the levels of OPG and OPN in particular to determine if there is a competition between pro-calcification and regulatory calcification markers.

4.5 Smooth muscle cell *in vitro* calcification

The findings from the examination of calcification markers in mTmG aortic tissue demonstrated that in aneurysm progression, VSMC can release pro-calcification markers and thus drive bone mineralisation in the aorta in response to disease. Therefore, examining the stimuli that could drive VSMC osteogenic differentiation was investigated.

Smooth muscle cells, derived from the aorta, and the upregulation of calcification protein in response to stimuli have been widely reported in the literature. Aortic smooth muscle cells (ASMC) derived from murine aorta exposed in high phosphate medium were positive for microcalcification deposits through alizarin red staining (237). PCR analysis found BMP2, BMP9 and Runx2 upregulation. In addition, 12-day addition of BMP2 elevated SMC calcification in ASMCs cultured in high phosphate medium (156). PCR analysis again showed the upregulation of BMP2 receptors. However, BMP2 added to SMCs cultured in normal conditions did not induce calcification, suggesting the need for a high phosphate background to elicit SMC calcification. Finally, application of pre-aged calcification media accelerated the onset of microcalcification deposition in ASMCs, as detected by alizarin red staining, through upregulation of TNF-α (223). This suggests that ASMCs are able to express calcification markers when challenged by pro-calcification environments.

To determine the optimum calcification conditions to study human aortic smooth muscle cell (aSMC) treatment, SVSMCs were used. This was due to the high cost of acquiring aSMC, the low availability of SMCs derived from the aorta with the correct background (i.e., non-trauma, healthy donors) and the high availability of SVSMCs in our institute. As seen in Figures 60 and 61, no change in expression of calcification markers was seen when cells were challenged with calcification media, and with the addition of PDGF-BB. The accelerated calcification media chosen in this study was originally reported in aSMC (223),

with no equivalent studies reported in SVSMCs. Therefore, the failure to induce calcification in SVSMCs could be because they are derived from a different vascular bed. In addition, the SVSMCs used were kindly donated by patients undergoing a cardiovascular intervention. It is therefore feasible that these individuals were predisposed to a cardiovascular disease, and thus may already exhibit calcification within the vascular system. Finally, the SVSMCs used in this study appeared senescent when examined under a light microscope, as well as displaying a fibroblast morphology.

However, there has been some evidence of *in vitro* SVSMC calcification reported elsewhere. Isolated SVSMCs incubated in AngII and pro-calcification media for 72 hours demonstrated increased expression of calcification transcription factors, including Runx2, and prevented Gla activity, a protein which normally inhibits of microcalcification development (238). It could be that an additional stimulus may be needed to promote calcification *in vitro* in SVSMCs. Increased expression of high mobility group box 1 promoted BMP2-driven calcification in SVSMCs through elevated glucose concentration in serum (239). Further optimisation would be required in these experiments to demonstrate the factors required to drive SVSMC calcification, and the role they play in the calcification processes of both aSMC and PPE-induced SMCs.

Chapter 5
Future Directions

As outlined earlier, although some of the initial aims of this PhD were achieved, the COVID-19 pandemic disrupted many of the planned experiments. This section details the future directions which could follow this project.

5.1 Preclinical PET/CT in PPE model of AAA

The results detailed in Sections 3.1-3.4 demonstrated some of the issues faced in small animal Na[^{18}F]F imaging for detecting microcalcification deposits in AAA. Therefore, it would be important to assess i) the capabilities of the Albira PET/SPECT/CT system housed in ePIC at the University of Leeds, and ii) PET/CT detection of microcalcification deposits in the PPE model.

Experiment 1: Phantom experiment

Qualitative assessment of PET/CT images acquired in this project demonstrated Na[^{18}F]F uptake in bone regions. However, in the AA, no apparent signal was seen. This was demonstrated in Figures 28–31, with no significant difference between sham and PPE models confirmed with a range of quantification metrics. This could be due to the detection limits of the scanner or signal from the spine masking any signal from the abdominal aorta.

Using data collected from USS and CTA experiments, cylindrical rods mimicking the abdominal aorta could be made into a phantom (Figure 65). These rods can be filled with a range of radioactivities reflecting the expected activity in the AA. The phantom can then be scanned and reconstructed using an optimised protocol. The result of this experiment would indicate whether the preclinical scanner in ePIC is capable of detecting the level of radioactivities in a model of interest reflecting AAA pathology. This would then confirm whether the use of another scanner should be considered (Experiment 3 Section 5.1), or whether to conduct further phantom experiments reflecting the *in vivo* scenario. Although this experiment would not reflect the *in vivo* model, it is an important step in determining whether the scanner is capable of imaging aortas and would be in line with the 3R's principle.

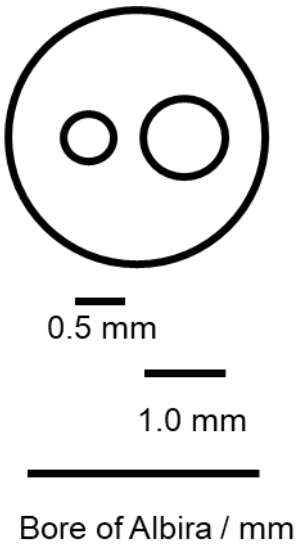

Figure 65: Schematic diagram of proposed PET/CT phantom. The phantom, with a diameter matching that of the bore of the Albira scanner, would contain rods representing a sham and PPE induced abdominal aorta.

Experiment 2: *Ex vivo* scanning of PPE aorta

One of the challenges in this project was the large Na[^{18}F]F uptake in the spine masking signal from the AA. MacAskill *et al.* demonstrated in the Ang-II model that excising and incubating the aorta in Na[^{18}F]F elegantly showed the distribution and uptake of Na[^{18}F]F without the presence of bone (228).

It may be useful to conduct a similar experiment in future work. Wild type mice would undergo sham or PPE surgery. As shown in Section 3.3, Na[^{18}F]F uptake was seen day 14 post surgery in PPE model using *ex vivo* gamma counting. In Section 3.5, however, upregulation of calcification markers was seen at day 7 post PPE surgery. Therefore it would be important to look at these two time points. The models would be subject to USS scan (to ensure AAA had been induced and to study correlation between Na[^{18}F]F uptake and aortic size) before fixing the aortas in 4% PFA (similar to OCT/RNA tissue extraction). These aortas would then be incubated in Na[^{18}F]F, following the methodology published by MacAskill *et al.*, and scanned on the Albira PET/SPECT/CT system (228). The results would demonstrate whether PET/CT imaging could reveal Na[^{18}F]F uptake *ex vivo* using samples of PPE-induced AAA.

Although the results from *ex vivo* scanning of PPE aortas would be beneficial in understanding the uptake of Na[^{18}F]F and distribution of microcalcifications in this model, certain limitations would need to be considered. Using this *ex vivo*

approach would not allow for monitoring of microcalcification development over the time course of 14 days (i.e., there would only be one time-point of analysis for each individual mouse). In addition, a large number of aortae would be needed for a viable experiment. Only a small amount of radioactivity would be required per scan, therefore it would be costly due to the expense that accompanies the shipping of radioactivity, and time on the scanner.

Experiment 3: PET/CT investigation of PPE induced AAA on different preclinical PET/CT scanners

One of the key challenges of biomarker validation is to demonstrate reproducibility in different clinics and with different imaging systems. This poses the question as to whether preclinical PET/CT imaging of PPE-induced AAA is achievable different scanners and if PET/CT metrics are in agreement when measuring Na[^{18}F]F in the AAA between imaging centres.

The experiment would require coordination with 2 or more sites that house differing preclinical PET/CT scanners and murine models would be imaged according to an approved protocol (including scan protocol, image reconstruction protocol and image analysis protocol) . This would allow us to understand if AAA generation with PPE is detectable with Na[^{18}F]F PET/CT, and if so, whether these imaging data could be reliably replicated elsewhere. Such information would verify if the PPE model is a useful approach for studying microcalcification development with Na[^{18}F]F, and in turn, whether it has applicability in a clinical setting for stratifying and offering personalised medicine to patients with AAA .

5.2 Validate *ex vivo* gamma counting findings

As demonstrated in Section 3.5, *ex vivo* gamma counting of aortic tissue post PET/CT imaging revealed a significant difference in uptake of Na[^{18}F]F at day 14 in the PPE model when compared to sham equivalents. Unfortunately, PET/CT imaging did not support these findings.

An alternative methodology would be to use autoradiography. In short, tissue sections are incubated with the radiotracer of choice, before exposing the tissue to a film to produce the autoradiograph. This experiment would validate findings from biodistribution studies, but also could be correlated with von Kossa stain. i.e., tissue sections positive or negative for Na[^{18}F]F could be stained for von Kossa to confirm the autoradiography findings. This study would provide

knowledge about the distribution of microcalcification deposits within the aortic wall, and where greatest Na[18F]F uptake occurs.

5.3 Microcalcification and aneurysm progression

The SoFIA[3] trial elegantly showed that Na[^{18}F]F uptake was a predictor of aneurysm growth and rupture independent of cardiovascular risk factors (e.g., smoking) in those with an aneurysm of 4.5–5 cm. The aim of this study was to use a preclinical model to further study the relationship between microcalcification deposits and aneurysm progression. In this thesis, it has been shown that microcalcification deposits are present in the AA at day 14 post surgery through von Kossa staining. A calcification remodelling response was also observed, with expression of BMP2 detected at day 7 post surgery.

Experiment 1: Validate microcalcification deposits in the aortic wall

Von Kossa stain demonstrated the presence of microcalcifications in histological sections. However, due to the quality of paraffin blocks, it was not possible for all samples to be stained and imaged. It would therefore be necessary to validate these findings using a von Kossa assay kit, which would enable quantification of von Kossa stain. Here, the AA would be excised before grinding. The tissue would then be exposed to the von Kossa assay kit reagents, followed by analysis on a suitable plate reader. This would then validate or show further, the amount of microcalcification deposits generated in the PPE model. It would be important to ensure that only the aneurysmal parts of the aorta are excised to confidently discuss the location of microcalcification deposition.

Experiment 2: The link between BMP2 expression and microcalcification deposits

In this thesis, BMP2 expression located in lineage traced VSMCs was elevated in PPE mice at day 7 and at day 14 compared to sham. However, it is uncertain whether the upregulation of BMP2 is the driver of microcalcification deposition in the PPE model. In addition, the contribution of BMP2 to the progression of PPE-induced AAA is unknown.

An ideal experiment would be to generate a VSMC-specific BMP2 knockout murine line and examine the development of PPE-induced AAA and microcalcification formation. The 3D USS protocol as described in Waduud *et al.*

could be used post-procedure, followed by excision of tissue and staining with a von Kossa kit or a calcification assay kit (e.g. Calcium Assay Kit, Abcam (ab112115) (59). This would provide understanding of the importance of BMP2 absence in mediating microcalcification deposition in the PPE model, and its impact on aneurysm progression. This may ultimately give more insight into the potential for targeted calcification-based therapeutics to slow aneurysm progression in patients. However, generating and validating a murine model would be a lengthy and costly process, and this would have to be carefully considered when planning future work.

5.4 Validation of calcification markers

A key finding in this thesis was the upregulation of BMP2 and Runx2 in the mTmG lineage trace model, with BMP2 expressed in lineage traced VSMCs and Runx2 expressed in cells also expressing mTom. However, although markers such as OPG are studied in human histological sections, no expression was found in the lineage traced model. It would therefore be sensible to further explore the levels of calcification markers expressed as a result of PPE surgery.

Wild type mice would undergo sham or PPE intervention, before being scanned using USS for quality assurance. RNA from excised aorta samples could then be sent for RNAseq analysis. The data would then be examined for the key calcification markers studied in this thesis to determine if data seen from IF experiments are true. This would provide whole tissue analysis of calcification markers which appear to be upregulated as a result of PPE intervention, as well as information on other pathways which may be upregulated. However, no information would be given on specific cell types that express predominately calcification markers, unless pure cell types are isolated from the tissue. In addition, it would be warranted to repeat this experiment in mTmG models to rule out any possibilities that the transgenic model affects PPE surgery and alters the level of calcification markers expressed.

5.5 Therapeutic response

One of the key research questions surrounding AAA research is the development of a therapeutic strategy which would slow down AAA progression, thereby providing a better quality of life for this patient cohort. As described in Section 1.6, many drugs have failed due to. There has been studies published recently

that has repurposed VEGF inhibitors such as Imatinib (115,116) and Lenvatinib (117) in small animal AAA models. Both drugs showed promise in attenuated aneurysm growth in response to surgical intervention. However, it is well documented that subjects taking imatinib and Lenvatinib do not tolerate the treatment well and may not be the best option for AAA subjects.

This study has shown that VSMC remodelling to an osteogenic phenotype may encourage microcalcification formation in AAA and could be a therapeutic target of interest. As BMP2 is a regulator of bone mineralisation under normal circumstances, it would be important to assess whether a therapeutic intervention could interfere with these non-pathological processes. Currently, there is no real treatment for preventing calcification deposition, other than lifestyle adjustments.

5.6 Conclusions and key findings

This work demonstrated the presence of calcification remodelling in the PPE preclinical model of AAA due to VSMC remodelling. Detection of calcification remodelling using Na[^{18}F]F PET/CT was not achieved. However, Na[^{18}F]F uptake in PPE AAA tissue was observed with *ex vivo* gamma counting. Elevation of BMP2, a driver of microcalcification formation, was seen in lineage traced VSMCs in early AAA development in the PPE model. This provides some insight into what stimulates microcalcification in human AAA, and Na[^{18}F]F could offer further understanding in the clinical setting. Further work is warranted to study how microcalcification influences both aneurysm growth and clinical end points (e.g., rupture) and whether this process represents a possible therapeutic target to meet an unmet clinical need.

List of References

1. Foundation BH. Heart and Circulatory Disease Statistics 2020. 2020.
2. Hurford R, Taveira I, Kuker W, Rothwell PM. Prevalence, predictors and prognosis of incidental intracranial aneurysms in patients with suspected TIA and minor stroke: A population-based study and systematic review. J Neurol Neurosurg Psychiatry. 2021;92(5):542–8.
3. Oliver-Williams C, Sweeting MJ, Jacomelli J, Summers L, Stevenson A, Lees T, et al. Safety of Men with Small and Medium Abdominal Aortic Aneurysms under Surveillance in the NAAASP. Circulation. 2019;139(11):1371–80.
4. Bäck M, Gasser TC, Michel JB, Caligiuri G. Biomechanical factors in the biology of aortic wall and aortic valve diseases. Cardiovasc Res. 2013;99(2):232–41.
5. Guo DC, Papke CL, He R, Milewicz DM. Pathogenesis of thoracic and abdominal aortic aneurysms. Ann N Y Acad Sci. 2006;1085:339–52.
6. Bunton TE, Jensen Biery N, Myers L, Gayraud B, Ramirez F, Dietz HC. Phenotypic alteration of vascular smooth muscle cells precedes elastolysis in a mouse model of Marfan syndrome. Circ Res. 2001;88(1):37–43.
7. Coady MA, Davies RR, Roberts M, Goldstein LJ, Rogalski MJ, Rizzo JA, et al. Familial patterns of thoracic aortic aneurysms. Arch Surg. 1999;134(4):361–7.
8. Isselbacher EM. Thoracic and abdominal aortic aneurysms. Circulation. 2005;111(6):816–28.
9. Sueyoshi E, Sakamoto I, Hayashi K. Aortic aneurysms in patients with Takayasu's arteritis: CT evaluation. Am J Roentgenol. 2000;175(6):1727–33.
10. Bade MA, Queral LA, Mukherjee D, Kong LS. Endovascular abdominal aortic aneurysm repair in a patient with Ehlers-Danlos syndrome. J Vasc Surg. 2007;46(2):360–2.
11. MacCarrick G, Black JH, Bowdin S, El-Hamamsy I, Frischmeyer-Guerrerio PA, Guerrerio AL, et al. Loeys-Dietz syndrome: A primer for diagnosis and

management. Genet Med. 2014;16(8):576–87.

12. Guo DC, Pannu H, Tran-Fadulu V, Papke CL, Yu RK, Avidan N, et al. Mutations in smooth muscle α-actin (ACTA2) lead to thoracic aortic aneurysms and dissections. Nat Genet. 2007;39(12):1488–93.

13. Raffort J, Lareyre F, Clément M, Hassen-Khodja R, Chinetti G, Mallat Z. Monocytes and macrophages in abdominal aortic aneurysm. Nat Rev Cardiol [Internet]. 2017;14(8):457–71. Available from: http://dx.doi.org/10.1038/nrcardio.2017.52

14. Sakalihasan N, Limet R, Defawe OD. Abdominal aortic aneurysm. Lancet. 2005;365:1577–89.

15. Daugherty A, Cassis LA. Mechanisms of abdominal aortic aneurysm formation. Curr Atheroscler Rep. 2002;4(3):222–7.

16. Howard DPJ, Banerjee A, Fairhead JF, Handa A, Silver LE, Rothwell PM. Age-specific incidence, risk factors and outcome of acute abdominal aortic aneurysms in a defined population. Br J Surg. 2015;102(8):907–15.

17. Karthikesalingam A, Holt PJ, Vidal-Diez A, Ozdemir BA, Poloniecki JD, Hinchliffe RJ, et al. Mortality from ruptured abdominal aortic aneurysms: Clinical lessons from a comparison of outcomes in England and the USA. Lancet. 2014;383(9921):963–9.

18. Bailey MA, Baxter PD, Jiang T, Charnell AM, Griffin KJ, Johnson AB, et al. Modeling the Growth of Infrarenal Abdominal Aortic Aneurysms. Aorta. 2014;1(6):268–73.

19. Golledge J, Muller J, Daugherty A, Norman P. Abdominal aortic aneurysm: Pathogenesis and implications for management. Arterioscler Thromb Vasc Biol. 2006;26(12):2605–13.

20. Nordon IM, Hinchliffe RJ, Loftus IM, Thompson MM. Pathophysiology and epidemiology of abdominal aortic aneurysms. Nat Rev Cardiol [Internet]. 2011;8(2):92–102. Available from: http://dx.doi.org/10.1038/nrcardio.2010.180

21. Sakalihasan N, Michel JB, Katsargyris A, Kuivaniemi H, Defraigne JO, Nchimi A, et al. Abdominal aortic aneurysms. Nat Rev Dis Prim [Internet]. 2018;4(1). Available from: http://dx.doi.org/10.1038/s41572-018-0030-7

22. Vardulaki KA, Walker NM, Day NE, Duffy SW, Ashton HA, Scott RAP. Quantifying the risks of hypertension, age, sex and smoking in patients with abdominal aortic aneurysm. Br J Surg. 2000;87(2):195–200.

23. Ashton HA, Buxton MJ, Day NE, Kim LG, Marteau TM, Scott RAP, et al. The Multicentre Aneurysm Screening Study (MASS) into the effect of abdominal aortic aneurysm screening on mortality in men: a randomised controlled trial. Lancet. 2002;360:1531–9.

24. Jacomelli J, Summers L, Stevenson A, Lees T, Earnshaw JJ. Impact of the first 5 years of a national abdominal aortic aneurysm screening programme. Br J Surg. 2016;103(9):1125–31.

25. Jacomelli J, Summers L, Stevenson A, Lees T, Earnshaw JJ. Update on the prevention of death from ruptured abdominal aortic aneurysm. J Med Screen. 2017;24(3):166–8.

26. Carter JL, Morris DR, Sherliker P, Clack R, Lam KBH, Halliday A, et al. Sex-Specific Associations of Vascular Risk Factors With Abdominal Aortic Aneurysm: Findings From 1.5 Million Women and 0.8 Million Men in the United States and United Kingdom. J Am Heart Assoc. 2020;9(4):1–8.

27. Sweeting MJ, Masconi KL, Jones E, Ulug P, Glover MJ, Michaels JA, et al. Analysis of clinical benefit, harms, and cost-effectiveness of screening women for abdominal aortic aneurysm. Lancet [Internet]. 2018;392(10146):487–95. Available from: http://dx.doi.org/10.1016/S0140-6736(18)31222-4

28. Aune D, Schlesinger S, Norat T, Riboli E. Tobacco smoking and the risk of abdominal aortic aneurysm: a systematic review and meta-analysis of prospective studies. Sci Rep. 2018;8(1):1–9.

29. Sode BF, Nordestgaard BG, Grønbæk M, Dahl M. Tobacco smoking and aortic aneurysm: Two population-based studies. Int J Cardiol [Internet]. 2013;167(5):2271–7. Available from: http://dx.doi.org/10.1016/j.ijcard.2012.06.003

30. Benson RA, Poole R, Murray S, Moxey P, Loftus IM. Screening results from a large United Kingdom abdominal aortic aneurysm screening center in the context of optimizing United Kingdom National Abdominal Aortic Aneurysm

Screening Programme protocols. J Vasc Surg [Internet]. 2016;63(2):301–4. Available from: http://dx.doi.org/10.1016/j.jvs.2015.08.091

31. Summers KL, Kerut EK, Sheahan CM, Sheahan MG. Evaluating the prevalence of abdominal aortic aneurysms in the United States through a national screening database. J Vasc Surg [Internet]. 2021;73(1):61–8. Available from: https://doi.org/10.1016/j.jvs.2020.03.046

32. Aune D, Schlesinger S, Norat T, Riboli E. Diabetes mellitus and the risk of abdominal aortic aneurysm: A systematic review and meta-analysis of prospective studies. J Diabetes Complications. 2018;32(12):1169–74.

33. Kristensen KL, Rasmussen LM, Hallas J, Lindholt JS. Diabetes Is Not Associated with the Risk of Rupture Among Patients with Abdominal Aortic Aneurysms – Results From a Large Danish Register Based Matched Case Control Study From 1996 to 2016. Eur J Vasc Endovasc Surg [Internet]. 2020;60(1):36–42. Available from: https://doi.org/10.1016/j.ejvs.2020.02.020

34. Raffort J, Lareyre F, Clément M, Hassen-Khodja R, Chinetti G, Mallat Z. Diabetes and aortic aneurysm: Current state of the art. Cardiovasc Res. 2018;114(13):1702–13.

35. Golledge J, Moxon J, Pinchbeck J, Anderson G, Rowbotham S, Jenkins J, et al. Association between metformin prescription and growth rates of abdominal aortic aneurysms. Br J Surg. 2017;104(11):1486–93.

36. Wilmink TBM, Quick CRG, Hubbard CS, Day NE. The influence of screening on the incidence of ruptured abdominal aortic aneurysms. J Vasc Surg. 1999;30(2):203–8.

37. Mealy K, Salman A. The true incidence of ruptured abdominal aortic aneurysms. Eur J Vasc Surg. 1988;2(6):405–8.

38. Davis M, Harris M, Earnshaw JJ. Implementation of the national health service abdominal aortic aneurysm screening program in England. J Vasc Surg [Internet]. 2013;57(5):1440–5. Available from: http://dx.doi.org/10.1016/j.jvs.2012.10.114

39. Lederle FA. Screening for AAA in the USA. Scand J Surg. 2008;97(2):139–41.

40. Svensjö S, Björck M, Wanhainen A. Update on screening for abdominal aortic aneurysm: A topical review. Eur J Vasc Endovasc Surg [Internet]. 2014;48(6):659–67. Available from: http://dx.doi.org/10.1016/j.ejvs.2014.08.029

41. Stather PW, Dattani N, Bown MJ, Earnshaw JJ, Lees TA. International variations in AAA screening. Eur J Vasc Endovasc Surg [Internet]. 2013;45(3):231–4. Available from: http://dx.doi.org/10.1016/j.ejvs.2012.12.013

42. Glover MJ, Kim LG, Sweeting MJ, Thompson SG, Buxton MJ. Cost-effectiveness of the National Health Service abdominal aortic aneurysm screening programme in England. Br J Surg. 2014;101(8):976–82.

43. Matthews EO, Pinchbeck J, Elmore K, Jones RE, Moxon J V., Golledge J. The reproducibility of measuring maximum abdominal aortic aneurysm diameter from ultrasound images. Ultrasound J [Internet]. 2021;13(1). Available from: https://doi.org/10.1186/s13089-021-00211-z

44. Powell JT, Brady AR, Brown LC, Forbes JF, Fowkes FGR, Greenhalgh RM, et al. Mortality results for randomised controlled trial of early elective surgery or ultrasonographic surveillance for small abdominal aortic aneurysms. Lancet. 1998;352(9141):1649–55.

45. Hartshorne TC, McCollum CN, Earnshaw JJ, Morris J, Nasim A. Ultrasound measurement of aortic diameter in a national screening programme. Eur J Vasc Endovasc Surg [Internet]. 2011;42(2):195–9. Available from: http://dx.doi.org/10.1016/j.ejvs.2011.02.030

46. Wanhainen A, Bjrck M. The Swedish experience of screening for abdominal aortic aneurysm. J Vasc Surg [Internet]. 2011;53(4):1164–5. Available from: http://dx.doi.org/10.1016/j.jvs.2010.10.099

47. Chiu KWH, Ling L, Tripathi V, Ahmed M, Shrivastava V. Ultrasound measurement for abdominal aortic aneurysm screening: A direct comparison of the three leading methods. Eur J Vasc Endovasc Surg [Internet]. 2014;47(4):367–73. Available from: http://dx.doi.org/10.1016/j.ejvs.2013.12.026

48. Powell JT, Brown LC, Forbes JF, Fowkes FGR, Greenhalgh RM, Ruckley

C V., et al. Final 12-year follow-up of surgery versus surveillance in the UK Small Aneurysm Trial. Br J Surg. 2007;94(6):702–8.

49. Schermerhorn ML, Cronenwett JL. To the Editors: The UK small aneurysm trial. J Vasc Surg. 2001;33(2):442–3.

50. Powell JT, Greenhalgh RM, Ruckley C V., Fowkes FGR. The UK Small Aneurysm Trial. Ann NY Acad Sci. 1996;18(800):249–51.

51. The RESCAN Collaborators. Surveillance Intervals for Small Abdominal Aortic Anurysms. Jama [Internet]. 2013;309(8):806–13. Available from: http://jama.jamanetwork.com/article.aspx?articleid=1656254

52. Parkinson F, Ferguson S, Lewis P, Williams IM, Twine CP. Rupture rates of untreated large abdominal aortic aneurysms in patients unfit for elective repair. J Vasc Surg [Internet]. 2015;61(6):1606–12. Available from: http://dx.doi.org/10.1016/j.jvs.2014.10.023

53. Earnshaw JJ. The Indication for Elective Repair of Abdominal Aortic Aneurysm Should Be Reviewed. Eur J Vasc Endovasc Surg [Internet]. 2021;61(1):7–8. Available from: https://doi.org/10.1016/j.ejvs.2020.09.001

54. Björck M, Boyle JR, Dick F. The Need of Research Initiatives Amidst and After the Covid-19 Pandemic: A Message from the Editors of the EJVES. Eur J Vasc Endovasc Surg [Internet]. 2020;59(5):695–6. Available from: https://doi.org/10.1016/j.ejvs.2020.04.002

55. Aggarwal S, Qamar A, Sharma V, Sharma A. Abdominal aortic aneurysm: A comprehensive review. Exp Clin Cardiol. 2011;16(1):11–5.

56. McGloughlin TM, Doyle BJ. New approaches to abdominal aortic aneurysm rupture risk assessment: Engineering insights with clinical gain. Arterioscler Thromb Vasc Biol. 2010;30(9):1687–94.

57. Fillinger MF, Marra SP, Raghavan ML, Kennedy FE. Prediction of rupture risk in abdominal aortic aneurysm during observation: Wall stress versus diameter. J Vasc Surg. 2003;37(4):724–32.

58. Kleinstreuer C, Li Z. Analysis and computer program for rupture-risk prediction of abdominal aortic aneurysms. Biomed Eng Online. 2006;5:1–13.

59. Waduud MA, Kandavelu P, Reay M, Paradine K, Scott DJA, Bailey MA.

High-Frequency Three-Dimensional Lumen Volume Ultrasound Is a Sensitive Method to Detect Early Aneurysmal Change in Elastase-Induced Murine Abdominal Aortic Aneurysm. Aorta. 2021;9:215–20.

60. Waton S, Johal A, Birmpili P, Li Q, Cromwell D, Pherwani A, et al. National Vascular Registry 2021 Annual Report [Internet]. Vsgbi. 2021. Available from: https://www.vsqip.org.uk/reports/2021-annual-report/

61. Moxon J V., Parr A, Emeto TI, Walker P, Norman PE, Golledge J. Diagnosis and Monitoring of Abdominal Aortic Aneurysm: Current Status and Future Prospects. Curr Probl Cardiol [Internet]. 2010;35(10):512–48. Available from: http://dx.doi.org/10.1016/j.cpcardiol.2010.08.004

62. Excellence N institute of clinical. Abdominal aortic aneurysm: diagnosis and management [NG156] [Internet]. March. 2020. Available from: https://www.nice.org.uk/guidance/ng156/chapter/Recommendations

63. Kieffer WKM, Sonnenberg S, Windhaber RA, Pal N, Pemberton RM. Complications and reintervention following elective open abdominal aortic aneurysm repair: A 10-year retrospective analysis. Ann R Coll Surg Engl. 2012;94(3):177–80.

64. Nataraj V, Mortimer AJ. Endovascular abdominal aortic aneurysm repair. Contin Educ Anaesthesia, Crit Care Pain. 2004;4(3):91–4.

65. Swerdlow NJ, Wu WW, Schermerhorn ML. Open and endovascular management of aortic aneurysms. Circ Res. 2019;124(4):647–61.

66. Greenhalgh RM, Brown LC, Kwong GPS, Powell JT, Thompson SG, Participants E trial. Comparison of endovascular aneurysm repair with open repair in patients with abdominal aortic aneurysm (EVAR trial 1), 30-day operative mortality results: randomised controlled trial. Lancet. 2004;364:843–8.

67. Prinssen M, Verhoeven ELG, Buth J, Cuypers PWM, Sambeek MRHM van, Balm R, et al. A Randomized Trial Comparing Conventional and Endovascular Repair of Abdominal Aortic Aneurysms. N Engl J Med. 2004;351(16):1607–18.

68. Lederle FA, Freischlag JA, Kyriakides TC, Padberg FT, Matsumura JS, Kohler TR, et al. Outcomes following endovascular vs open repair of

abdominal aortic aneurysm: A randomized trial. JAMA - J Am Med Assoc. 2009;302(14):1535–42.

69. Patel R, Sweeting MJ, Powell JT, Greenhalgh RM. Endovascular versus open repair of abdominal aortic aneurysm in 15-years' follow-up of the UK endovascular aneurysm repair trial 1 (EVAR trial 1): a randomised controlled trial. Lancet [Internet]. 2016;388(10058):2366–74. Available from: http://dx.doi.org/10.1016/S0140-6736(16)31135-7

70. van Schaik TG, Yeung KK, Verhagen HJ, de Bruin JL, van Sambeek MRHM, Balm R, et al. Long-term survival and secondary procedures after open or endovascular repair of abdominal aortic aneurysms. J Vasc Surg. 2017;66(5):1379–89.

71. Sweeting MJ, Patel R, Powell JT, Greenhalgh RM. Endovascular Repair of Abdominal Aortic Aneurysm in Patients Physically Ineligible for Open Repair. Ann Surg. 2017;266(5):713–9.

72. Bailey MA. Store Operated Calcium Entry in Abdominal Aortic Aneurysm. University of Leeds; 2016.

73. Gandhi R, Cawthorne C, Craggs LJL, Wright JD, Domarkas J, He P, et al. Cell proliferation detected using [18F]FLT PET/CT as an early marker of abdominal aortic aneurysm. J Nucl Cardiol [Internet]. 2019; Available from: https://doi.org/10.1007/s12350-019-01946-y

74. Nabseth DC, Martin DE, Rowe MI, S L Gotlieb, Deterling R A. Enzymatic destruction of aortic elastic tissue and possible relationship to experimental atherosclerosis. J Cardiovasc Surg (Torino). 1963 Feb;4:11–7.

75. Patelis N, Moris D, Schizas D, Damaskos C, Perrea D, Bakoyiannis C, et al. Animal models in the research of Abdominal aortic aneurysms development. Physiol Res. 2017;66(6):899–915.

76. Golledge J. Abdominal aortic aneurysm: update on pathogenesis and medical treatments. Nat Rev Cardiol [Internet]. 2019;16(4):225–42. Available from: http://dx.doi.org/10.1038/s41569-018-0114-9

77. Bhamidipati CM, Mehta GS, Lu G, Moehle CW, Barbery C, Dimusto PD, et al. Development of a novel murine model of aortic aneurysms using peri-adventitial elastase. Vol. 152, Surgery (United States). 2012. p. 238–46.

78. Waduud MA, Kandavelu P, Reay M, Paradine K, Scott DJA, Baily MA. High frequency 3D lumen volume ultrasound is a sensitive method to detect early aneurysmal change in elastase induced murine abdominal aortic aneurysm. Aorta. 2021;

79. Sénémaud J, Caligiuri G, Etienne H, Delbosc S, Michel JB, Coscas R. Translational Relevance and Recent Advances of Animal Models of Abdominal Aortic Aneurysm. Arterioscler Thromb Vasc Biol. 2017;37(3):401–10.

80. Pyo R, Lee JK, Shipley JM, Curci JA, Mao D, Ziporin SJ, et al. Targeted gene disruption of matrix metalloproteinase-9 (gelatinase B) suppresses development of experimental abdominal aortic aneurysms. J Clin Invest. 2000;105(11):1641–9.

81. Ailawadi G, Eliason JL, Roelofs KJ, Sinha I, Hannawa KK, Kaldjian EP, et al. Gender differences in experimental aortic aneurysm formation. Arterioscler Thromb Vasc Biol. 2004;24(11):2116–22.

82. Lindholt JS. Aneurysmal wall calcification predicts natural history of small abdominal aortic aneurysms. Atherosclerosis. 2008;197(2):673–8.

83. Forsythe RO, Dweck MR, McBride OMB, Vesey AT, Semple SI, Shah ASV, et al. 18F–Sodium Fluoride Uptake in Abdominal Aortic Aneurysms: The SoFIA3 Study. J Am Coll Cardiol. 2018;71(5):513–23.

84. Gertz SD, Kurgan A, Eisenberg D. Aneurysm of the rabbit common carotid artery induced by periarterial application of calcium chloride in vivo. J Clin Invest. 1988;81(3):649–56.

85. Wang Y, Krishna S, Golledge J. The calcium chloride-induced rodent model of abdominal aortic aneurysm. Atherosclerosis [Internet]. 2013;226(1):29–39. Available from: http://dx.doi.org/10.1016/j.atherosclerosis.2012.09.010

86. Chiou AC, Chiu B, Pearce WH. Murine aortic aneurysm produced by periarterial application of calcium chloride. J Surg Res. 2001;99(2):371–6.

87. Sheth RA, Maricevich M, Mahmood U. In vivo optical molecular imaging of matrix metalloproteinase activity in abdominal aortic aneurysms correlates with treatment effects on growth rate. Atherosclerosis [Internet].

2010;212(1):181–7. Available from: http://dx.doi.org/10.1016/j.atherosclerosis.2010.05.012

88. Kimura T, Yoshimura K, Aoki H, Imanaka-Yoshida K, Yoshida T, Ikeda Y, et al. Tenascin-C is expressed in abdominal aortic aneurysm tissue with an active degradation process. Pathol Int. 2011;61(10):559–64.

89. Xiong W, Knispel R, Mactaggart J, Baxter BT. Effects of tissue inhibitor of metalloproteinase 2 deficiency on aneurysm formation. J Vasc Surg. 2006;44(5):1061–6.

90. Lysgaard Poulsen J, Stubbe J, Lindholt JS. Animal Models Used to Explore Abdominal Aortic Aneurysms: A Systematic Review. Eur J Vasc Endovasc Surg [Internet]. 2016;52(4):487–99. Available from: http://dx.doi.org/10.1016/j.ejvs.2016.07.004

91. Matthew Longo G, Xiong W, Greiner TC, Zhao Y, Fiotti N, Timothy Baxter B. Matrix metalloproteinases 2 and 9 work in concert to produce aortic aneurysms. J Clin Invest. 2002;110(5):625–32.

92. Isenburg JC, Simionescu DT, Starcher BC, Vyavahare NR. Elastin stabilization for treatment of abdominal aortic aneurysms. Circulation. 2007;115(13):1729–37.

93. Kaneko H, Anzai T, Morisawa M, Kohno T, Nagai T, Anzai A, et al. Resveratrol prevents the development of abdominal aortic aneurysm through attenuation of inflammation, oxidative stress, and neovascularization. Atherosclerosis [Internet]. 2011;217(2):350–7. Available from: http://dx.doi.org/10.1016/j.atherosclerosis.2011.03.042

94. Daugherty A, Cassis L. Chronic Angiotensin II Infusion Promotes Atherogenesis in Low Density Lipoprotein Receptor - / - Mice. Ann N Y Acad Sci. 1999;892(606):108–18.

95. Daugherty A, Manning MW, Cassis LA. Angiotensin II promotes atherosclerotic lesions and aneurysms in apolipoprotein E-deficient mice. J Clin Invest. 2000;105(11):1605–12.

96. Rush C, Nyara M, Moxon J V., Trollope A, Cullen B, Golledge J. Whole genome expression analysis within the angiotensin II-apolipoprotein E deficient mouse model of abdominal aortic aneurysm. BMC Genomics.

2009;10:1–20.

97. Saraff K, Babamusta F, Cassis LA, Daugherty A. Aortic dissection precedes formation of aneurysms and atherosclerosis in angiotensin II-infused, apolipoprotein E-deficient mice. Arterioscler Thromb Vasc Biol. 2003;23(9):1621–6.

98. Deng GG, Martin-McNulty B, Sukovich DA, Freay A, Halks-Miller M, Thinnes T, et al. Urokinase-type plasminogen activator plays a critical role in angiotensin II-induced abdominal aortic aneurysm. Circ Res. 2003;92(5):510–7.

99. Cassis LA, Gupte M, Thayer S, Zhang X, Charnigo R, Howatt DA, et al. ANG II infusion promotes abdominal aortic aneurysms independent of increased blood pressure in hypercholesterolemic mice. Am J Physiol - Hear Circ Physiol. 2009;296(5):1660–5.

100. Manning MW, Cassis LA, Huang J, Szilvassy SJ, Daugherty A. Abdominal aortic aneurysms: Fresh insights from a novel animal model of the disease. Vasc Med. 2002;7(1):45–54.

101. Rateri DL, Howatt DA, Moorleghen JJ, Charnigo R, Cassis LA, Daugherty A. Prolonged infusion of angiotensin II in apoE -/- mice promotes macrophage recruitment with continued expansion of abdominal aortic aneurysm. Am J Pathol. 2011;179(3):1542–8.

102. Trachet B, Fraga-Silva RA, Jacquet PA, Stergiopulos N, Segers P. Incidence, severity, mortality, and confounding factors for dissecting AAA detection in angiotensin II-infused mice: A meta-analysis. Cardiovasc Res. 2015;108(1):159–70.

103. Quintana RA, Taylor WR. Cellular mechanisms of aortic aneurysm formation. Circ Res. 2019;124(4):607–18.

104. Biros E, Gäbel G, Moran CS, Schreurs C, Lindeman JHN, Walker PJ, et al. Differential gene expression in human abdominal aortic aneurysm and aortic occlusive disease. Oncotarget. 2015;6(15):12984–96.

105. Paik DC, Fu C, Bhattacharya J, Tilson MD. Ongoing angiogenesis in blood vessels of the abdominal aortic aneurysm. Exp Mol Med. 2004;36(6):524–33.

106. Thompson MM, Jones L, Nasim A, Sayers RD, Bell PRF. Angiogenesis in abdominal aortic aneurysms. Eur J Vasc Endovasc Surg. 1996;11(4):464–9.

107. Sano M, Sasaki T, Hirakawa S, Sakabe J, Ogawa M, Baba S, et al. Lymphangiogenesis and angiogenesis in abdominal aortic aneurysm. PLoS One. 2014;9(3).

108. Choke E, Cockerill GW, Dawson J, Wilson RW, Jones A, Loftus IM, et al. Increased angiogenesis at the site of abdominal aortic aneurysm rupture. Ann N Y Acad Sci. 2006;1085:315–9.

109. Yu M, Chen C, Cao Y, Qi R. Inhibitory effects of doxycycline on the onset and progression of abdominal aortic aneurysm and its related mechanisms. Eur J Pharmacol [Internet]. 2017;811(May):101–9. Available from: http://dx.doi.org/10.1016/j.ejphar.2017.05.041

110. Abdul-Hussien H, Hanemaaijer R, Verheijen JH, van Bockel JH, Geelkerken RH, Lindeman JHN. Doxycycline therapy for abdominal aneurysm: Improved proteolytic balance through reduced neutrophil content. J Vasc Surg [Internet]. 2009;49(3):741–9. Available from: http://dx.doi.org/10.1016/j.jvs.2008.09.055

111. Meijer CA, Stijnen T, Wasser MNJM, Hamming JF, van Bockel JH, Lindeman JHN. Doxycycline for stabilization of abdominal aortic aneurysms: a randomized trial. Ann Intern Med. 2013 Dec;159(12):815–23.

112. Baxter BT, Matsumura J, Curci JA, McBride R, Larson L, Blackwelder W, et al. Effect of Doxycycline on Aneurysm Growth among Patients with Small Infrarenal Abdominal Aortic Aneurysms: A Randomized Clinical Trial. JAMA - J Am Med Assoc. 2020;323(20):2029–38.

113. Isoda K, Akita K, Kitamura K, Sato-Okabayashi Y, Kadoguchi T, Isobe S, et al. Inhibition of interleukin-1 suppresses angiotensin II-induced aortic inflammation and aneurysm formation. Int J Cardiol [Internet]. 2018;270:221–7. Available from: https://doi.org/10.1016/j.ijcard.2018.05.072

114. Lindeman JH, Matsumura JS. Pharmacologic management of aneurysms.

Circ Res. 2019;124(4):631–46.

115. Vorkapic E, Dugic E, Vikingsson S, Roy J, Mäyränpää MI, Eriksson P, et al. Imatinib treatment attenuates growth and inflammation of angiotensin II induced abdominal aortic aneurysm. Atherosclerosis. 2016;249:101–9.

116. Yao F, Yao Z, Zhong T, Zhang J, Wang T, Zhang B, et al. Imatinib prevents elastase-induced abdominal aortic aneurysm progression by regulating macrophage-derived MMP9. Eur J Pharmacol [Internet]. 2019;860(May):172559. Available from: https://doi.org/10.1016/j.ejphar.2019.172559

117. Busch A, Pauli J, Winski G, Bleichert S, Chernogubova E, Metschl S, et al. Lenvatinib halts aortic aneurysm growth by restoring smooth muscle cell contractility. JCI Insight. 2021;6(15).

118. Airhart N, Brownstein BH, Cobb JP, Schierding W, Arif B, Ennis TL, et al. Smooth muscle cells from abdominal aortic aneurysms are unique and can independently and synergistically degrade insoluble elastin. J Vasc Surg [Internet]. 2014;60(4):1033-1042.e5. Available from: http://dx.doi.org/10.1016/j.jvs.2013.07.097

119. Jones GT, Tromp G, Kuivaniemi H, Gretarsdottir S, Baas AF, Giusti B, et al. Meta-Analysis of Genome-Wide Association Studies for Abdominal Aortic Aneurysm Identifies Four New Disease-Specific Risk Loci. Circ Res. 2017;120(2):341–53.

120. López-Candales A, Holmes DR, Liao S, Scott MJ, Wickline SA, Thompson RW. Decreased vascular smooth muscle cell density in medial degeneration of human abdominal aortic aneurysms. Am J Pathol. 1997;150(3):993–1007.

121. Rowe VL, Stevens SL, Reddick TT, Freeman MB, Donnell R, Carroll RC, et al. Vascular smooth muscle cell apoptosis in aneurysmal, occlusive, and normal human aortas. J Vasc Surg. 2000;31(3):567–76.

122. Shanahan CM. Mechanisms of vascular calcification in CKD - Evidence for premature ageing? Nat Rev Nephrol. 2013;9(11):661–70.

123. Nakano-Kurimoto R, Ikeda K, Uraoka M, Nakagawa Y, Yutaka K, Koide M, et al. Replicative senescence of vascular smooth muscle cells enhances

the calcification through initiating the osteoblastic transition. Am J Physiol - Hear Circ Physiol. 2009;297(5).

124. Gomez D, Owens GK. Smooth muscle cell phenotypic switching in atherosclerosis. Cardiovasc Res. 2012;95(2):156–64.

125. Caplice NM, Bunch TJ, Stalboerger PG, Wang S, Simper D, Miller D V., et al. Smooth muscle cells in human coronary atherosclerosis can originate from cells administered at marrow transplantation. Proc Natl Acad Sci U S A. 2003;100(8):4754–9.

126. Roostalu U, Aldeiri B, Albertini A, Humphreys N, Simonsen-Jackson M, Wong JKF, et al. Distinct cellular mechanisms underlie smooth muscle turnover in vascular development and repair. Circ Res. 2018;122(2):267–81.

127. Trion A, Van Der Laarse A. Vascular smooth muscle cells and calcification in atherosclerosis. Am Heart J. 2004;147(5):808–14.

128. Hofmann Bowman MA, McNally EM. Genetic Pathways of Vascular Calcification. Trends Cardiovasc Med [Internet]. 2012;22(4):93–8. Available from: http://dx.doi.org/10.1016/j.tcm.2012.07.002

129. Lee SJ, Lee IK, Jeon JH. Vascular calcification—new insights into its mechanism. Int J Mol Sci. 2020;21(8).

130. Mori H, Torii S, Kutyna M, Sakamoto A, Finn A V., Virmani R. Coronary Artery Calcification and its Progression: What Does it Really Mean? JACC Cardiovasc Imaging. 2018;11(1):127–42.

131. Wang Y, Osborne MT, Tung B, Li M, Li Y. Imaging cardiovascular calcification. J Am Heart Assoc. 2018;7(13):1–15.

132. Motoyama S, Kondo T, Sarai M, Sugiura A, Harigaya H, Sato T, et al. Multislice Computed Tomographic Characteristics of Coronary Lesions in Acute Coronary Syndromes. J Am Coll Cardiol. 2007;50(4):319–26.

133. Allison MA, Pavlinac P, Wright CM. The differential associations between HDL, non-HDL and total cholesterols and atherosclerotic calcium deposits in multiple vascular beds. Atherosclerosis. 2007;194(2):87–94.

134. Criqui MH, Kamineni A, Allison MA, Ix JH, Carr JJ, Cushman M, et al. Risk factor differences for aortic versus coronary calcified atherosclerosis: The

multiethnic study of atherosclerosis. Arterioscler Thromb Vasc Biol. 2010;30(11):2289–96.

135. Demer LL, Tintut Y. Vascular calcification: Pathobiology of a multifaceted disease. Circulation. 2008;117(22):2938–48.

136. Bartstra JW, Mali WPTM, Spiering W, De Jong PA. Abdominal aortic calcification: From ancient friend to modern foe. Eur J Prev Cardiol. 2021;28(12):1386–91.

137. Petsophonsakul P, Furmanik M, Forsythe R, Dweck M, Schurink GW, Natour E, et al. Role of vascular smooth muscle cell phenotypic switching and calcification in aortic aneurysm formation involvement of Vitamin K-dependent processes. Arterioscler Thromb Vasc Biol. 2019;39(7):1351–68.

138. Durham AL, Speer MY, Scatena M, Giachelli CM, Shanahan CM. Role of smooth muscle cells in vascular calcification: Implications in atherosclerosis and arterial stiffness. Cardiovasc Res. 2018;114(4):590–600.

139. Nakayama A, Morita H, Hayashi N, Nomura Y, Hoshina K, Shigematsu K, et al. Inverse correlation between calcium accumulation and the expansion rate of abdominal aortic aneurysms. Circ J. 2016;80(2):332–9.

140. Wanga S, Hibender S, Ridwan Y, van Roomen C, Vos M, van der Made I, et al. Aortic microcalcification is associated with elastin fragmentation in Marfan syndrome. J Pathol. 2017;243(3):294–306.

141. Chowdhury MM, Zieliński LP, Sun JJ, Lambracos S, Boyle JR, Harrison SC, et al. Editor's Choice – Calcification of Thoracic and Abdominal Aneurysms is Associated with Mortality and Morbidity. Eur J Vasc Endovasc Surg. 2018;55(1):101–8.

142. Golledge J, Muller J, Shephard N, Clancy P, Smallwood L, Moran C, et al. Association between osteopontin and human abdominal aortic aneurysm. Arterioscler Thromb Vasc Biol. 2007;27(3):655–60.

143. Cho HJ, Cho HJ, Kim HS. Osteopontin: A multifunctional protein at the crossroads of inflammation, atherosclerosis, and vascular calcification. Curr Atheroscler Rep. 2009;11(3):206–13.

144. Wada T, McKee MD, Steitz S, Giachelli CM. Calcification of vascular smooth muscle cell cultures: Inhibition by osteopontin. Circ Res. 1999;84(2):166–78.

145. Speer MY, Chien YC, Quan M, Yang HY, Vali H, McKee MD, et al. Smooth muscle cells deficient in osteopontin have enhanced susceptibility to calcification in vitro. Cardiovasc Res. 2005;66(2):324–33.

146. Bruemmer D, Collins AR, Noh G, Wang W, Territo M, Arias-Magallona S, et al. Angiotensin II-accelerated atherosclerosis and aneurysm formation is attenuated in osteopontin-deficient mice. J Clin Invest. 2003;112(9):1318–31.

147. Otto F, Thornell AP, Crompton T, Denzel A, Gilmour KC, Rosewell IR, et al. Cbfa1, a candidate gene for cleidocranial dysplasia syndrome, is essential for osteoblast differentiation and bone development. Cell. 1997;89(5):765–71.

148. Sun Y, Byon CH, Yuan K, Chen J, Mao X, Heath JM, et al. Smooth muscle cell-specific runx2 deficiency inhibits vascular calcification. Circ Res. 2012;111(5):543–52.

149. Komori T, Yagi * H., Nomura S, Yamaguchi A. Targeted disruption of. Proc Natl Acad Sci U S A [Internet]. 1998;95(15):8692–7. Available from: http://www.pubmedcentral.nih.gov/articlerender.fcgi?artid=21138&tool=pmcentrez&rendertype=abstract

150. Tyson KL, Reynolds JL, McNair R, Zhang Q, Weissberg PL, Shanahan CM. Osteo/chondrocytic transcription factors and their target genes exhibit distinct patterns of expression in human arterial calcification. Arterioscler Thromb Vasc Biol. 2003;23(3):489–94.

151. Li Z, Zhao Z, Cai Z, Sun Y, Li L, Yao F, et al. Runx2 (Runt-Related Transcription Factor 2)-Mediated Microcalcification Is a Novel Pathological Characteristic and Potential Mediator of Abdominal Aortic Aneurysm. Arterioscler Thromb Vasc Biol. 2020;2(May):1352–69.

152. Hruska KA, Mathew S, Saab G. Bone morphogenetic proteins in vascular calcification. Circ Res. 2005;97(2):105–14.

153. Yang P, Troncone L, Augur ZM, Kim SSJ, McNeil ME, Yu PB. The role of

bone morphogenetic protein signaling in vascular calcification. Bone [Internet]. 2020;141(April):115542. Available from: https://doi.org/10.1016/j.bone.2020.115542

154. Boström K, Watson KE, Horn S, Wortham C, Herman IM, Demer LL. Bone morphogenetic protein expression in human atherosclerotic lesions. J Clin Invest. 1993;91(4):1800–9.

155. Dhore CR, Cleutjens JPM, Lutgens E, Cleutjens KBJM, Geusens PPM, Kitslaar PJEHM, et al. Differential expression of bone matrix regulatory proteins in human atherosclerotic plaques. Arterioscler Thromb Vasc Biol. 2001;21(12):1998–2003.

156. Li X, Yang HY, Giachelli CM. BMP-2 promotes phosphate uptake, phenotypic modulation, and calcification of human vascular smooth muscle cells. Atherosclerosis. 2008;199(2):271–7.

157. Wong GA, Tang V, El-Sabeawy F, Weiss RH. BMP-2 inhibits proliferation of human aortic smooth muscle cells via p21Cip1/Waf1. Am J Physiol - Endocrinol Metab. 2003;284(5 47-5):972–9.

158. Rifas L, Arackal S, Weitzmann MN. Inflammatory T cells rapidly induce differentiation of human bone marrow stromal cells into mature osteoblasts. J Cell Biochem. 2003;88(4):650–9.

159. Parhami F, Morrow AD, Balucan J, Leitinger N, Watson AD, Tintut Y, et al. Lipid oxidation products have opposite effects on calcifying vascular cell and bone cell differentiation: A possible explanation for the paradox of arterial calcification in osteoporotic patients. Arterioscler Thromb Vasc Biol. 1997;17(4):680–7.

160. Moran CS, McCann M, Karan M, Norman P, Ketheesan N, Golledge J. Association of osteoprotegerin with human abdominal aortic aneurysm progression. Circulation. 2005;111(23):3119–25.

161. Bumdelger B, Kokubo H, Kamata R, Fujii M, Yoshimura K, Aoki H, et al. Osteoprotegerin Prevents Development of Abdominal Aortic Aneurysms. PLoS One. 2016;11(1):1–19.

162. Jono S, Ikari Y, Shioi A, Mori K, Miki T, Hara K, et al. Serum osteoprotegerin levels are associated with the presence and severity of coronary artery

disease. Circulation. 2002;106(10):1192–4.

163. Ueland T, Jemtland R, Godang K, Kjekshus J, Hognestad A, Omland T, et al. Prognostic value of osteoprotegerin in heart failure after acute myocardial infarction. J Am Coll Cardiol [Internet]. 2004;44(10):1970–6. Available from: http://dx.doi.org/10.1016/j.jacc.2004.06.076

164. Golledge J, McCann M, Mangan S, Lam A, Karan M. Osteoprotegerin and osteopontin are expressed at high concentrations within symptomatic carotid atherosclerosis. Stroke. 2004;35(7):1636–41.

165. Koole D, Hurks R, Schoneveld A, Vink A, Golledge J, Moran CS, et al. Osteoprotegerin is associated with aneurysm diameter and proteolysis in abdominal aortic aneurysm disease. Arterioscler Thromb Vasc Biol. 2012;32(6):1497–504.

166. Moran CS, Jose RJ, Biros E, Golledge J. Osteoprotegerin deficiency limits angiotensin ii-induced aortic dilatation and rupture in the apolipoprotein e-knockout mouse. Arterioscler Thromb Vasc Biol. 2014;34(12):2609–16.

167. Bumdelger B, Otani M, Karasaki K, Sakai C, Ishida M, Kokubo H, et al. Disruption of Osteoprotegerin has complex effects on medial destruction and adventitial fibrosis during mouse abdominal aortic aneurysm formation. PLoS One [Internet]. 2020;15(7 July):1–13. Available from: http://dx.doi.org/10.1371/journal.pone.0235553

168. Vorkapic E, Kunath A, Wågsäter D. Effects of osteoprotegerin/TNFRSF11B in two models of abdominal aortic aneurysms. Mol Med Rep. 2018;18(1):41–8.

169. Moran CS, Cullen B, Campbell JH, Golledge J. Interaction between angiotensin II, osteoprotegerin, and peroxisome proliferator-activated receptor-γ in abdominal aortic aneurysm. J Vasc Res. 2009;46(3):209–17.

170. James ML, Gambhir SS. A molecular imaging primer: Modalities, imaging agents, and applications. Physiol Rev. 2012;92(2):897–965.

171. Aldrich JE. Basic physics of ultrasound imaging. Crit Care Med. 2007;35(5 SUPPL.):131–7.

172. Goldman LW. Principles of CT and CT technology. J Nucl Med Technol. 2007;35(3):115–28.

173. Boll H, Bag S, Schambach SJ, Doyon F, Nittka S, Kramer M, et al. High-speed singleybreath-hold microycomputed tomography of thoracic and abdominal structures in mice using a simplified method for intubation. J Comput Assist Tomogr. 2010;34(5):783–90.

174. Zhu G, Sun H, Wang J, Zhao Z, Bao J, Feng R, et al. In Vivo Detection and Measurement of Aortic Aneurysm and Dissection in Mouse Models Using Microcomputed Tomography with Contrast Agent. Contrast Media Mol Imaging. 2019;2019.

175. Ametamey SM, Honer M, Schubiger PA. Molecular imaging with PET. Chem Rev. 2008;108(5):1501–16.

176. EANM. Guidance to Radiotracer Nomenclature [Internet]. 2019. Available from: https://www.eanm.org/publications/guidelines/nomenclature/

177. Jensen MM, Kjaer A. Monitoring of anti-cancer treatment with (18)F-FDG and (18)F-FLT PET: a comprehensive review of pre-clinical studies. Am J Nucl Med Mol Imaging [Internet]. 2015;5(5):431–56. Available from: http://www.ncbi.nlm.nih.gov/pubmed/26550536%0Ahttp://www.pubmedcentral.nih.gov/articlerender.fcgi?artid=PMC4620172

178. Gambhir SS. Molecular imaging of cancer with positron emission tomography. Nat Rev Cancer. 2002;2(9):683–93.

179. Harrison MR, George DJ. Better late than early: FDG-PET imaging in metastatic renal cell carcinoma. Clin Cancer Res. 2011;17(18):5841–3.

180. Even-Sapir E, Mishani E, Flusser G, Metser U. 18F-Fluoride Positron Emission Tomography and Positron Emission Tomography/Computed Tomography. Semin Nucl Med. 2007;37(6):462–9.

181. Mosconi L. Brain glucose metabolism in the early and specific diagnosis of Alzheimer's disease: FDG-PET studies in MCI and AD. Eur J Nucl Med Mol Imaging. 2005;32(4):486–510.

182. Boellaard R. Standards for PET image acquisition and quantitative data analysis. J Nucl Med. 2009;50(SUPPL. 1):11–21.

183. Chen W, Dilsizian V. PET assessment of vascular inflammation and atherosclerotic plaques: SUV or TBR? J Nucl Med. 2015;56(4):503–4.

184. Kinahan PE, Fletcher JW. Positron emission tomography-computed

tomography standardized uptake values in clinical practice and assessing response to therapy. Semin Ultrasound, CT MRI. 2010;31(6):496–505.

185. Thie JA. Understanding the standardized uptake value, its methods, and implications for usage. J Nucl Med. 2004;45(9):1431–4.

186. Chomet M, Schreurs M, Vos R, Verlaan M, Kooijman EJ, Poot AJ, et al. Performance of nanoScan PET/CT and PET/MR for quantitative imaging of 18F and 89Zr as compared with ex vivo biodistribution in tumor-bearing mice. EJNMMI Res [Internet]. 2021;11(1). Available from: https://doi.org/10.1186/s13550-021-00799-2

187. Tawakol A, Migrino RQ, Bashian GG, Bedri S, Vermylen D, Cury RC, et al. In Vivo 18F-Fluorodeoxyglucose Positron Emission Tomography Imaging Provides a Noninvasive Measure of Carotid Plaque Inflammation in Patients. J Am Coll Cardiol. 2006;48(9):1818–24.

188. Lee YH, Choi SJ, Ji JD, Song GG. Diagnostische Genauigkeit der 18F-FDG PET bzw. PET/CT für Vaskulitiden großer Gefäße: Eine Metaanalyse. Z Rheumatol. 2016;75(9):924–31.

189. Einat Even-Sapir, MD, PhD1, 2; Ur Metser, MD1, 2; Eyal Mishani, PhD3; Gennady Lievshitz, MD1; Hedva Lerman M, and Ilan Leibovitch, MD2 4. The Detection of Bone Metastases in Patients with High-Risk Prostate Cancer : 99m Tc-MDP Planar. J Nucl Med. 2006;47:287–97.

190. Freesmeyer M, Stecker FF, Schierz JH, Hofmann GO, Winkens T. First experience with early dynamic 18F-NaF-PET/CT in patients with chronic osteomyelitis. Ann Nucl Med. 2014;28(4):314–21.

191. Czernin J, Satyamurthy N, Schiepers C. Molecular mechanisms of bone 18F-NaF deposition. J Nucl Med. 2010;51(12):1826–9.

192. Cocker MS, Spence JD, Hammond R, Wells G, deKemp RA, Lum C, et al. [18F]-NaF PET/CT Identifies Active Calcification in Carotid Plaque. JACC Cardiovasc Imaging. 2017;10(4):486–8.

193. Irkle A, Vesey AT, Lewis DY, Skepper JN, Bird JLE, Dweck MR, et al. Identifying active vascular microcalcification by 18F-sodium fluoride positron emission tomography. Nat Commun [Internet]. 2015;6(May):1–11. Available from: http://dx.doi.org/10.1038/ncomms8495

194. Derlin T, Richter U, Bannas P, Begemann P, Buchert R, Mester J, et al. Feasibility of 18F-sodium fluoride PET/CT for imaging of atherosclerotic plaque. J Nucl Med. 2010;51(6):862–5.

195. Dweck MR, Jones C, Joshi N V., Fletcher AM, Richardson H, White A, et al. Assessment of valvular calcification and inflammation by positron emission tomography in patients with aortic stenosis. Circulation. 2012;125(1):76–86.

196. Massera D, Trivieri MG, Andrews JPM, Sartori S, Abgral R, Chapman AR, et al. Disease activity in mitral annular calcification: A multimodality study. Circ Cardiovasc Imaging. 2019;12(2):1–10.

197. Joshi N V., Vesey AT, Williams MC, Shah ASV, Calvert PA, Craighead FHM, et al. 18F-fluoride positron emission tomography for identification of ruptured and high-risk coronary atherosclerotic plaques: A prospective clinical trial. Lancet [Internet]. 2014;383(9918):705–13. Available from: http://dx.doi.org/10.1016/S0140-6736(13)61754-7

198. Kitagawa T, Yamamoto H, Toshimitsu S, Sasaki K, Senoo A, Kubo Y, et al. 18F-Sodium Fluoride positron emission tomography for molecular imaging of coronary atherosclerosis based on computed tomography analysis. Atherosclerosis. 2017;263:385–92.

199. Chowdhury MM, Tarkin JM, Albaghdadi MS, Evans NR, Le EP V, Berrett TB, et al. Vascular Positron Emission Tomography and Restenosis in Symptomatic Peripheral Arterial Disease. A prospective clinical study. J Am Coll Cardiol Cardiovasc Imaging. 2020;13(4):1008–17.

200. Folco EJ, Sheikine Y, Rocha VZ, Christen T, Shvartz E, Sukhova GK, et al. Hypoxia but not inflammation augments glucose uptake in human macrophages: Implications for imaging atherosclerosis with 18fluorine-labeled 2-deoxy-D-glucose positron emission tomography. J Am Coll Cardiol. 2011;58(6):603–414.

201. Courtois A, Nusgens B V., Hustinx R, Namur G, Gomez P, Somja J, et al. 18F-FDG uptake assessed by PET/CT in abdominal aortic aneurysms is associated with cellular and molecular alterations prefacing wall deterioration and rupture. J Nucl Med. 2013;54(10):1740–7.

202. Marini C, Morbelli S, Armonino R, Spinella G, Riondato M, Massollo M, et al. Direct relationship between cell density and FDG uptake in asymptomatic aortic aneurysm close to surgical threshold: An in vivo and in vitro study. Eur J Nucl Med Mol Imaging. 2012;39(1):91–101.

203. Tegler G, Ericson K, Srensen J, Bjrck M, Wanhainen A. Inflammation in the walls of asymptomatic abdominal aortic aneurysms is not associated with increased metabolic activity detectable by 18-fluorodeoxglucose positron-emission tomography. J Vasc Surg [Internet]. 2012;56(3):802–7. Available from: http://dx.doi.org/10.1016/j.jvs.2012.02.024

204. Reeps C, Essler M, Pelisek J, Seidl S, Eckstein HH, Krause BJ. Increased 18F-fluorodeoxyglucose uptake in abdominal aortic aneurysms in positron emission/computed tomography is associated with inflammation, aortic wall instability, and acute symptoms. J Vasc Surg. 2008;48(2):417–23.

205. Morel O, Mandry D, Micard E, Kauffmann C, Lamiral Z, Verger A, et al. Evidence of cyclic changes in the metabolism of abdominal aortic aneurysms during growth phases: 18F-FDG PET sequential observational study. J Nucl Med. 2015;56(7):1030–5.

206. Barwick TD, Lyons OTA, Mikhaeel NG, Waltham M, O'Doherty MJ. 18F-FDG PET-CT uptake is a feature of both normal diameter and aneurysmal aortic wall and is not related to aneurysm size. Eur J Nucl Med Mol Imaging. 2014;41(12):2310–8.

207. Kotze CW, Groves AM, Menezes LJ, Harvey R, Endozo R, Kayani IA, et al. What is the relationship between 18F-FDG aortic aneurysm uptake on PET/CT and future growth rate? Eur J Nucl Med Mol Imaging. 2011;38(8):1493–9.

208. Nchimi A, Cheramy-Bien JP, Gasser TC, Namur G, Gomez P, Seidel L, et al. Multifactorial relationship between 18F-fluoro-deoxy-glucose positron emission tomography signaling and biomechanical properties in unruptured aortic aneurysms. Circ Cardiovasc Imaging. 2014;7(1):82–91.

209. Courtois A, Makrygiannis G, El Hachemi M, Hultgren R, Allaire E, Namur G, et al. Positron Emission Tomography/Computed Tomography Predicts and Detects Complications After Endovascular Repair of Abdominal Aortic Aneurysms. J Endovasc Ther. 2019;26(4):520–8.

210. Marie PY, Plissonnier D, Bravetti S, Coscas R, Rouer M, Haulon S, et al. Low baseline and subsequent higher aortic abdominal aneurysm FDG uptake are associated with poor sac shrinkage post endovascular repair. Eur J Nucl Med Mol Imaging. 2018;45(4):549–57.

211. Carvajal-Juarez I, Alexanderson-Rosas E, Meave-Gonzalez A, Ortega-Silva S, Espinola-Zavaleta N. Non-invasive assessment of endarteritis in Marfan syndrome with aortic dissection after surgical treatment. J Nucl Cardiol [Internet]. 2019;26(5):1759–60. Available from: https://doi.org/10.1007/s12350-018-1370-0

212. Blockmans D, Coudyzer W, Vanderschueren S, Stroobants S, Loeckx D, Heye S, et al. Relationship between fluorodeoxyglucose uptake in the large vessels and late aortic diameter in giant cell arteritis. Rheumatology. 2008;47(8):1179–84.

213. Kuehl H, Eggebrecht H, Boes T, Antoch G, Rosenbaum S, Ladd S, et al. Detection of inflammation in patients with acute aortic syndrome: Comparison of FDG-PET/CT imaging and serological markers of inflammation. Heart. 2008;94(11):1472–7.

214. Tegler G, Estrada S, Hall H, Wanhainen A, Björck M, Sörensen J, et al. Autoradiography screening of potential positron emission tomography tracers for asymptomatic abdominal aortic aneurysms. Ups J Med Sci. 2014;119(3):229–35.

215. Kitagawa T, Kosuge H, Chang E, James ML, Yamamoto T, Shen B, et al. Integrin-targeted molecular imaging of experimental abdominal aortic aneurysms by 18F-labeled Arg-Gly-Asp positron-emission tomography. Circ Cardiovasc Imaging. 2013;6(6):950–6.

216. Shi S, Orbay H, Yang Y, Graves SA, Nayak TR, Hong H, et al. PET imaging of abdominal aortic aneurysm with 64Cu-labeled anti-CD105 antibody fab fragment. J Nucl Med. 2015;56(6):927–32.

217. Been LB, Suurmeijer AJH, Cobben DCP, Jager PL, Hoekstra HJ, Elsinga PH. [18F]FLT-PET in oncology: Current status and opportunities. Eur J Nucl Med Mol Imaging. 2004;31(12):1659–72.

218. Bertagna F, Biasiotto G, Giubbini R. The role of F-18-fluorothymidine PET

in oncology. Clin Transl Imaging. 2013;1(2):77–97.

219. Syed MBJ, Fletcher AJ, Dweck MR. Imaging cellular activity and proliferation in the aortic wall. J Nucl Cardiol [Internet]. 2019;8–11. Available from: https://doi.org/10.1007/s12350-019-01987-3

220. Seidman J FGMSDDBKSZJJMRSMI, Stroud DM, Darrow BJ, Kim SD, Zhang J, Jongbloed MRM, et al. A Global Double-Fluorescent Cre Reporter Mouse. Genesis. 2007;45:593–605.

221. Deidda D, Akerele MI, Aykroyd RG, Dweck MR, Ferreira K, Forsythe RO, et al. Improved identification of abdominal aortic aneurysm using the Kernelized Expectation Maximization algorithm. Philos Trans R Soc A Math Phys Eng Sci. 2021;379(2200).

222. Deidda D, Karakatsanis NA, Robson PM, Tsai YJ, Efthimiou N, Thielemans K, et al. Hybrid PET-MR list-mode kernelized expectation maximization reconstruction. Inverse Probl. 2019;35(4).

223. Aghagolzadeh P, Bachtler M, Bijarnia R, Jackson C, Smith ER, Odermatt A, et al. Calcification of vascular smooth muscle cells is induced by secondary calciprotein particles and enhanced by tumor necrosis factor-α. Atherosclerosis [Internet]. 2016;251:404–14. Available from: http://dx.doi.org/10.1016/j.atherosclerosis.2016.05.044

224. Akerele MI, Karakatsanis NA, Forsythe RO, Dweck MR, Syed M, Aykroyd RG, et al. Iterative reconstruction incorporating background correction improves quantification of [18F]-NaF PET/CT images of patients with abdominal aortic aneurysm. J Nucl Cardiol [Internet]. 2021;28(5):1875–86. Available from: https://doi.org/10.1007/s12350-019-01940-4

225. Huet P, Burg S, Le Guludec D, Hyafil F, Buvat I. Variability and uncertainty of 18F-FDG PET imaging protocols for assessing inflammation in atherosclerosis: Suggestions for improvement. J Nucl Med. 2015;56(4):552–9.

226. Sánchez F, Moliner L, Correcher C, Gonzlez A, Orero A, Carles M, et al. Small animal PET scanner based on monolithic LYSO crystals: Performance evaluation. Med Phys. 2012;39(2):643–53.

227. Sánchez F, Orero A, Soriano A. ALBIRA : A small animal PET / SPECT /

CT imaging system. 2013;40(5):1–11.

228. MacAskill MG, McDougald W, Alcaide-Corral C, Newby DE, Tavares AAS, Hadoke PWF, et al. Characterisation of an atherosclerotic micro-calcification model using ApoE−/− mice and PET/CT. IJC Hear Vasc. 2020;31:4–6.

229. Gäbel G, Northoff BH, Balboa A, Becirovic-Agic M, Petri M, Busch A, et al. Parallel murine and human aortic wall genomics reveals metabolic reprogramming as key driver of abdominal aortic aneurysm progression. J Am Heart Assoc. 2021;10(17):1–19.

230. Wang G, Qi J. PET image reconstruction using kernel method. IEEE Trans Med Imaging. 2015;34(1):61–71.

231. Deidda D, Karakatsanis NA, Robson PM, Calcagno C, Senders ML, Mulder WJM, et al. Hybrid PET/MR kernelised expectation maximisation reconstruction for improved image-derived estimation of the input function from the aorta of rabbits. Contrast Media Mol Imaging. 2019;2019.

232. McDougald W, Vanhove C, Lehnert A, Lewellen B, Wright J, Mingarelli M, et al. Standardization of Preclinical PET/CT Imaging to Improve Quantitative Accuracy, Precision, and Reproducibility: A Multicenter Study. J Nucl Med. 2020;61(3):461–8.

233. Basalyga DM, Simionescu DT, Xiong W, Baxter BT, Starcher BC, Vyavahare NR. Elastin degradation and calcification in an abdominal aorta injury model: Role of matrix metalloproteinases. Circulation. 2004;110(22):3480–7.

234. Lei Y, Sinha A, Nosoudi N, Grover A, Vyavahare N. Hydroxyapatite and calcified elastin induce osteoblast-like differentiation in rat aortic smooth muscle cells. Exp Cell Res [Internet]. 2014;323(1):198–208. Available from: http://dx.doi.org/10.1016/j.yexcr.2014.01.011

235. Simionescu A, Philips K, Vyavahare N. Elastin-derived peptides and TGF-β1 induce osteogenic responses in smooth muscle cells. Biochem Biophys Res Commun. 2005;334(2):524–32.

236. Yap C, Mieremet A, De Vries CJM, Micha D, De Waard V. Six shades of vascular smooth muscle cells illuminated by klf4 (krüppel-like factor 4).

Arterioscler Thromb Vasc Biol. 2021;4(November):2693–707.

237. Zhu D, Mackenzie NCW, Shanahan CM, Shroff RC, Farquharson C, Macrae VE. BMP-9 regulates the osteoblastic differentiation and calcification of vascular smooth muscle cells through an ALK1 mediated pathway. J Cell Mol Med. 2015;19(1):165–74.

238. Jia G, Stormont RM, Gangahar DM, Agrawal DK. Role of matrix Gla protein in angiotensin II-induced exacerbation of vascular calcification. Am J Physiol - Hear Circ Physiol. 2012;303(5):523–32.

239. Wang Y, Shan J, Yang W, Zheng H, Xue S. High mobility group box 1 (HMGB1) mediates high-glucose-induced calcification in vascular smooth muscle cells of saphenous veins. Inflammation. 2013;36(6):1592–604.